SAPIENZA
UNIVERSITÀ DI ROMA

Modeling clinopyroxene and plagioclase growth kinetics at Mt. Etna and Stromboli: A time-integrated, polybaric and polythermal perspective

PhD Thesis

Piergiorgio Moschini
XXXV cycle

Supervisor:
Prof. Mario Gaeta

Co-Supervisor:
Prof. Silvio Mollo
Dr. Piergiorgio Scarlato

TABLE OF CONTENTS

Introduction 1

Parameterization of clinopyroxene growth kinetics via crystal size distribution (CSD) analysis: Insights into the temporal scales of magma dynamics at Mt. Etna volcano 3

Abstract 4

1. Introduction 5

2. Methods 7

2.1. Experimental strategy 7

2.2. Image processing and CSD correction 11

2.3. Microanalysis 14

3. Results 15

3.1. Textural features 15

3.2. Crystal content variation 16

3.3. Clinopyroxene euhedrality 17

3.4. Compositional features 17

4. Discussion 19

4.1. Clinopyroxene growth rate and thermodynamic constraints 19

4.3 Parameterization of clinopyroxene growth kinetics 24

4.4. Application to magma dynamics at Mt. Etna volcano 27

5. Conclusions 34

Acknowledgments 35

References 36

Figure captions 45

Figures 48

Tables 56

A review of plagioclase growth rate and compositional evolution in mafic alkaline magmas: Guidelines for modeling plumbing system dynamics at Stromboli and Mt. Etna 60

Abstract 61

1. Introduction 63

2. Methods 65

2.1 Experimental procedure 65

2.2 Microchemical analysis 67

2.3 Textural analysis 68

2.4 Statistical analysis 70

3. Plagioclase growth rate parameterization 71

3.1. Plagioclase growth principles 71

3.2 Growth-related plagioclase parameters 74

3.3 Control of crystallization time on growth rate 76
3.4 Estimating eruptive timescales at Stromboli and Mt. Etna 79
4. Plagioclase and melt compositional changes 83
4.1 Plagioclase cation substitutions and exchange partition coefficients 83
4.2 Tracking differentiation conditions of natural mafic alkaline melts 88
5. Thermodynamic and statistical modeling of plagioclase-melt equilibrium 89
5.1 Preliminary considerations 89
5.2 Anorthite-albite melt activities and the role of H_2O^{melt} 93
5.3 Plagioclase-based thermometry 99
6. Interpreting *T* and H_2O^{melt} in zoned plagioclase crystals 104
7. Conclusions and recommendations 110
Acknowledgments 112
References 112
Figure captions 131
Figures 134
Concluding remarks 144
Acknowledgements 146

Introduction

Basaltic volcanoes (e.g., Mt. Etna, Stromboli, Hawaii, etc.) are characterized by a range of effusive to explosive activities with variable intensity, which can pose different type of threats to local populations. Challenges in modern volcanology and petrology involve the attempt to constrain pre-eruptive magmatic processes, which provide the basis for volcanic hazard assessment. Although the recent literature has reported constant advancements in this respect, several key questions remain unanswered. Understanding how magma is stored, migrates and feeds eruption is not a trivial task, requiring for renewed improvements over the years. In this context, both textural maturation and compositional variability of minerals crystallizing in basaltic systems represent valuable sources of information to quantify the physio-chemical conditions experienced by magmas upon the effect of changing and complex plumbing system dynamics.

This study aims to provide new insights on the solidification behavior of mafic alkaline magmas erupted at Mt. Etna and Stromboli (Italy). Such open conduit volcanoes are characterized by the ubiquitous stability of clinopyroxene from mantle depths to shallow crustal levels. More evolved magmas are also saturated with plagioclase, especially at lower temperatures, melt-water contents, and pressures. Thus, clinopyroxene and plagioclase crystals represent powerful recorders of the intricate ascent dynamics explored by mafic alkaline magmas during their ascent paths towards the surface. By focusing on textural and chemical features of natural/synthetic clinopyroxene, plagioclase and coexisting glasses, I have provided new tools for interpreting polythermal-polybaric changes of magmas, together with several guidelines and a secure methodology to model pre- and syn-eruptive conditions. The temporal evolution of Etnean and Strombolian magmas has been also tracked via timescale modeling to better constrain the cooling-decompression paths of magmas rising and accelerating through the vertically extended, highly dynamic plumbing systems.

In the first part of this PhD thesis, I have experimentally explored the role of supersaturation and relaxation phenomena on clinopyroxene nucleation and growth processes, which affect the final crystal cargo of variably undercooled magmas. A certain degree of undercooling is pivotal to promote

the growth and textural maturation of crystals. With increasing crystallization time, however, the crystal growth rate decreases as the system approaches to near-equilibrium conditions that minimize the effect of melt supersaturation. By quantifying the textural features of synthetic and natural crystals it has been possible to parameterize clinopyroxene growth kinetics under a broad range of isothermal-isobaric, decompression, and cooling conditions representative of crystallization scenarios typically encountered in open-conduit volcanoes. This model parameterization has been combined with the textural analysis of natural clinopyroxene crystals erupted during lava fountain events at Mt. Etna allowing to unlock timescale of growth for microphenocryst and microlite populations. The retrieved temporal information has been used to develop a new conceptual model for the timescale of magma dynamics recorded by the (dis)equilibrium textural evolution of clinopyroxene and for the rapid acceleration of magma ascending within the volcanic conduit, immediately before eruption at the vent.

A more comprehensive work, focusing on plagioclase textural and compositional features, characterized the second part of my PhD thesis with the aim to identify disparate aspects of plagioclase growth scenarios. Following the same approach discussed above, timescale of plagioclase crystallization from mafic alkaline magmas has been parameterized as a function of growth rate by integrating experimental (i.e., isothermal-isobaric, decompression, and cooling experiments) and natural textural data from literature. Timescales of eruptive processes at Mt. Etna and Stromboli volcanoes have been quantified by considering phenocryst/microphenocryst and microlite crystals growing during lava flow and explosive eruptions. Statistical methodologies have been employed to assess the correlation between plagioclase growth rate and other system parameters governing the crystallization process. Special attention has been paid to disambiguate the role of temperature and melt-H_2O content on plagioclase chemical zoning patterns at Stromboli and Mt. Etna. By using plagioclase components and major cation substitution mechanisms, I have refined and readapted equilibrium, thermometric, and hygrometric models for future investigations.

Parameterization of clinopyroxene growth kinetics via crystal size distribution (CSD) analysis: Insights into the temporal scales of magma dynamics at Mt. Etna volcano

[1*]Piergiorgio Moschini, [1,2]Silvio Mollo, [1]Mario Gaeta, [3]Sara Fanara, [2]Manuela Nazzari, [4]Chiara Maria Petrone, [2]Piergiorgio Scarlato

[1]Department of Earth Sciences, Sapienza - University of Rome, P. le Aldo Moro 5, 00185 Roma, Italy

[2]Istituto Nazionale di Geofisica e Vulcanologia - Department Roma 1, Via di Vigna Murata 605, 00143 Roma, Italy

[3]Abteilung Experimentelle und Angewandte Mineralogie, Georg August Universität Göttingen, Goldschmidtstraße 1, 37077 Göttingen, Germany

[4]The Natural History Museum, Department of Earth Sciences, Cromwell Road, SW7 5BD, London, United Kingdom

*Corresponding author:

Piergiorgio Moschini

piergiorgio.moschini@uniroma1.it

Department of Earth Sciences

Sapienza - University of Rome

P. le Aldo Moro 5

00185 Roma, Italy

Published in Lithos 396-397, 106225

Abstract

There is increasing recognition that both textural and compositional changes of clinopyroxene crystallizing from mafic alkaline magmas are the direct expression of complex dynamic processes extending over a broad range of spatial and temporal scales. Among others, supersaturation and relaxation phenomena play a key role in controlling the final crystal cargo of variably undercooled magmas erupted from active alkaline volcanoes. Following this line of reasoning, we have carried out isothermal-isobaric, decompression, and cooling rate experiments on a basalt interpreted as the parental magma of mafic alkaline eruptions at Mt. Etna volcano (Sicily, Italy). The main purpose is to reconstruct and quantify the textural changes (i.e., length of major and minor axes, surface area per unit volume, area fraction, and maximum growth rate) of clinopyroxene at variable pressures (30-300 MPa), temperatures (1,050-1,100 °C), volatile contents (0-5 wt.% H_2O and 0-0.2 wt.% CO_2), and equilibration times (0.25-72 h). Melt supersaturation, corresponding to a degree of undercooling variable from 14 to 125 °C, drives the formation of clinopyroxene crystals with different textures and sizes as a function of growth rate and relaxation time. By integrating experimental data and thermodynamic modeling, the transition between interface-controlled (euhedral morphologies) and diffusion-controlled (anhedral morphologies) growth regimes has been determined to occur at degrees of undercooling higher than 30 °C. The decrease of clinopyroxene growth rate with increasing the equilibration time is combined with the crystal size distribution (CSD) analysis of naturally undercooled clinopyroxene crystals erupted during 2011-2012 lava fountain episodes at Mt. Etna volcano. Results indicate that the crystallization of microlites and microphenocrysts is on the order of ~10^0-10^1 min (large undercooling, short equilibration time) and ~10^1-10^2 h (small undercooling, long equilibration time), respectively. This temporal information allows to better constrain the cooling-decompression paths of Etnean magmas rising and accelerating along a vertically extended, highly dynamic plumbing system. While clinopyroxene microlites develop during the fast ascent of magmas (~10^0-10^1 m s^{-1}) within the uppermost part of the conduit or immediately before ejection from the vent, the onset of microphenocryst crystallization occurs at depth and continues within the

plumbing system during the slow ascent of magmas (~10^{-2} m s^{-1}) that migrate through interconnected storage regions.

1. Introduction

Clinopyroxene is an important recorder of the physico-chemical changes explored by mafic alkaline magmas typically occurring in intraplate settings. Owing to its ubiquitous crystallization over a broad range of pressures, temperatures, and volatile contents (e.g., Mollo et al., 2018), a gamut of studies have investigated the clinopyroxene textural and compositional variations in alkaline products, with the main purpose of elucidating pre-eruptive magma storage conditions at depth and syn-eruptive dynamics during ascent of magma towards the surface (e.g., Petrone et al., 2016, 2018; Ubide and Kamber, 2018).

While the stability field of clinopyroxene is intrinsically related to the intensive and extensive variables governing the thermodynamic reactions at the interface between crystal, melt, and fluid phases, a certain degree of undercooling (ΔT) is essential to promote the growth and textural maturation of clinopyroxene. ΔT is the thermodynamic driving force of crystallization and can be defined as the difference between the temperature at which a specific mineral saturates the melt and the temperature of a naturally solidifying system. In single-step undercooling experiments characterized by a rapid, large drop in pressure-temperature, the melt composition can be assumed constant during the decompression-cooling path controlling ΔT. As a consequence, the degree of supersaturation of the mineral-forming components can be linked and quantified directly through the magnitude of ΔT (Shea and Hammer, 2013 and references therein). Several reviews examined the phenomenological aspects related to the kinetics of crystal nucleation and growth (e.g., Kirkpatrick, 1981; Cashman, 1990; Lasaga, 1998; Hammer, 2006; Iezzi et al., 2014; Mollo and Hammer, 2017; Giuliani et al., 2020), along with increasing emphasis on the importance of magma supersaturation

state to resolve specific petrological and volcanological problems involving the environmental conditions of magmatic reservoirs and their dynamic evolutions.

Recently, some authors (Hammer et al., 2016; Welsch et al., 2016; Ubide et al., 2019a, 2019b; Di Stefano et al., 2020) focused their attention on the profound effect exercised by ΔT on the morphology and composition of clinopyroxene growing from mafic alkaline magmas, such as those erupted at Haleakala (Hawaii) and Mt. Etna and Stromboli (Italy). These authors documented that systematic departure from equilibrium arises by composite growth histories driven by imbalance between the rate at which the crystal surfaces advance and the rate of cation diffusion in the melt. In particular, for magmas erupted at Mt. Etna, it has been experimentally found that strong supersaturation effects correspond to large ΔT, leading to disequilibrium uptake of incompatible cations at the crystal-melt interface. These rate-limiting concentration gradients promote high nucleation rates and fast development of small, anhedral clinopyroxene crystals (Polacci et al., 2018; Arzilli et al., 2019; Masotta et al., 2020). Conversely, under the driving force of small ΔT, the bulk system attempts to return to a near-equilibrium state between the advancing crystal surfaces and the melt composition. Because of the effect of growth kinetics, large, euhedral clinopyroxene crystals develop by minimizing the interfacial free energy between crystal and surrounding melt. Time-series experiments have also outlined that the shift from a diffusion-controlled to an interface-controlled growth regime is intimately governed by relaxation phenomena lowering the concentration gradients at the crystal-melt interface and leading to a steady-state textural maturation of clinopyroxene (Pontesilli et al., 2019). After initial supersaturation effects, the growth rate of clinopyroxene progressively decreases with increasing relaxation time, thereby approaching to a near-equilibrium condition where attachment/detachment reactions of cations from the melt onto the crystalline surface (and *vice versa*) occur at the same rate (Pontesilli et al., 2019). These time-series experiments also corroborate the textural maturation model proposed by Welsch et al. (2016) for the growth of large clinopyroxene phenocrysts from ankaramite lava flows erupted at Haleakala. According to the authors, the external morphology, chemical variation, and internal structure of these phenocrysts

testify to a continuous growth rate decrease over time, in response to less effective supersaturation conditions driving gradual transition between diffusion-controlled and interface-controlled regimes (Welsch et al., 2016).

On the basis of previous laboratory data from Pontesilli et al. (2019) and Masotta et al. (2020), we have conducted complementary isothermal-isobaric, decompression, and cooling rate experiments on a primitive basalt from Mt. Etna, in order to assess the control of supersaturation and relaxation phenomena on clinopyroxene crystallization. In agreement with crystal growth thermodynamics and kinetics, the textural maturation of clinopyroxene is attained at small undercoolings and long equilibration times. Under such conditions, we measure a growth rate decay of six orders of magnitude that is modeled as a function of relaxation kinetics. This empirical relationship is interpolated to the algebraic expression of crystal size distribution (CSD) analysis, with the final purpose of quantifying the time scale of crystallization during decompression-cooling of mafic alkaline magmas. As a test case, microlites and microphenocrysts from scoria clasts ejected during 2011-2012 lava fountains at Mt. Etna have been considered. Results from calculations give rise to a conceptual model for the time scale of magma dynamics recorded by the (dis)equilibrium textural evolution of clinopyroxene and for the rapid acceleration of magma ascending within the volcanic conduit, immediately before eruption at the vent.

2. Methods

2.1. Experimental strategy

The starting material used for the experiments is a natural basalt from the Monte Maletto Formation erupted at Mt. Etna around 7,000 years ago. Monte Maletto Formation comprises basaltic to trachybasaltic products that have been interpreted by numerous authors as the parental compositions of historic and recent Etnean eruptions (see the review study of Mollo et al., 2018 and references therein). The powdered rock was melted to ensure homogeneity of the final starting

material at the HP-HT Laboratory of Experimental Volcanology and Geophysics of the Istituto Nazionale di Geofisica e Vulcanologia (INGV), Rome, Italy. A crucible containing the natural powder was loaded in a 1 atm vertical tube CO–CO_2 gas-mixing furnace at 1,300 °C for 1 h. The redox state was 2 log unit above the Ni-NiO buffer (NNO+2), comparable to that estimated at the Mt. Etna (Mollo et al., 2015a). Iron loss was kept to < 5% of the initial amount by adopting a Fe pre-saturated Pt crucible. The quenched glass was analyzed by scanning electron microscopy and no crystalline phases were detected. Twenty microprobe analyses of the glass yielded an average composition (in wt.%) of 47.56 (±0.39) SiO_2, 1.48 (±0.11) TiO_2, 15.42 (±0.23) Al_2O_3, 10.79 (±0.17) FeO_{tot}, 0.21 (±0.04) MnO, 7.98 (±0.15) MgO, 12.13 (±0.18) CaO, 2.61 (±0.13) Na_2O, 1.25 (±0.12) K_2O, and 0.57 (±0.04) P_2O_5.

Isothermal and decompression experiments were carried out in an internally heated pressure vessel (IHPV) equipped with a continuum decompression system and a rapid quenching device (drop quench) at the Abteilung Experimentelle und Angewandte Mineralogie, Georg August Universität Göttingen (Germany). The powdered starting glass was loaded in Fe-presaturated Pt-capsules. Isobaric experiments (*Experimental Set ISO*) were conducted at 300 MPa and temperatures of 1,100 (*ISO-1100*), 1,075 (*ISO-1075*), and 1,050 °C (*ISO-1050*) that were kept constant over an equilibration time of ~24 hours (Table 1). The experiments were heated directly to the target temperature at a rate of 50 °C min^{-1} and were carried out under nominally anhydrous and hydrous conditions, corresponding to 0 wt.% $H_2O_{initial}$ (*ISO-0H2O*, i.e., nominally anhydrous system), 2 wt.% $H_2O_{initial}$ (*ISO-2H2O*), 5 wt.% $H_2O_{initial}$ (*ISO-5H2O*), and 2 wt.% $H_2O_{initial}$ + 0.2 wt.% $CO_{2initial}$ (*ISO-H2O+CO2*). H_2O and CO_2 were added as deionized water and oxalic acid, respectively. Decompression experiments (*Experimental Set ΔP*) were conducted at the same temperatures and anhydrous-hydrous conditions by depressurizing the charges from 300 to 30 MPa at slow (*ΔPs*) and fast (*ΔPf*) rates of 0.018 and 0.98 MPa s^{-1}, respectively (Table 1). Pressures, temperatures, and melt-H_2O+CO_2 contents have been selected in order to reproduce the most common crystallization-degassing path of magmas at Mt. Etna, as derived by thermobarometric-hygrometric calculations and

melt inclusion data (Mollo et al., 2018 and references therein). Slow to fast decompression experiments correspond to magma ascent velocities in the range of 0.45-24.5 m s^{-1}, in agreement with previous estimates suggested by geophysical, crystallochemical, and numerical studies focusing on magma conduit dynamics at Mt. Etna (Aloisi et al., 2006; Mollo et al., 2015b; La Spina et al., 2016; Giuffrida et al., 2017). Note that the solubility of H_2O in this melt composition is ~2.9 and ~0.5 wt.% at 300 (i.e., fluid-absent) and 30 (i.e., fluid-present) MPa, respectively, as derived by the thermodynamic model of Duan (2014) and corroborated by numerous studies carried out on mafic alkaline magmas (Mollo et al., 2018 and references therein). Coherently, magma dynamics at Mt. Etna volcano are frequently recognized as the result of complex crystallization regimes that, at shallow crustal levels, change from H_2O-undersaturated to H_2O-saturated (i.e., $P_{H2O} = P_{total}$) conditions, in conjunction with abundant volatile degassing (Mollo et al., 2015b, 2018; Perinelli et al., 2016, 2018). The temperature was monitored by three S-type (Pt90Rh10/Pt with uncertainty of ±3 °C) thermocouples and pressure was recorded by a transducer, calibrated against a Heise tube gauge with accuracy ±5 MPa. Experiments were quenched using a drop quench device imposing a cooling rate of ~150 °C s^{-1}. Recovered charges were mounted in epoxy and polished thin sections was produced from the epoxy blocks. The use of Ar as a pressure medium provided an intrinsic fO_2 variable from NNO+2 to NNO+4 (Schanofski et al., 2019). Within the sample capsule, fH_2 was controlled by hydrogen permeation through the capsule walls driven by the fugacity gradient between the pressure medium and the capsule interior. This in turn determined the fO_2 inside the capsule through the equilibrium $H_2 + 1/2\ O_2 \leftrightarrow H_2O$. However, under fluid-present conditions and with the addition of CO_2, the redox state of the system changed in response to the variable activity of H_2O in the melt (Botcharnikov et al. 2008). In this respect, the redox state of the system was estimated at the end of experimental runs through the oxygen barometer of Ishibashi (2013) based on spinel–melt equilibria and with uncertainty (±0.3 log unit). This model was calibrated using an alkaline data set, returning fO_2 estimates variable from NNO+1.9 and NNO+2.3 buffer (Mollo et al., 2015a).

Cooling rate experiments (Table 1) were carried out in a non-end loaded piston cylinder apparatus ("QUICKpress", Depths of the Earth co.) using a 19-mm NaCl-pyrex-graphite-MgO assembly that produced an apparent redox state close to NNO+2 buffer (Mollo and Masotta, 2014). The assembly was loaded with a Fe-presaturated Pt-capsule containing the hydrous (2 wt.% $H_2O_{initial}$) glass. The capsules were surrounded by powdered pyrophyllite to prevent H_2O loss and enhance stress homogenization during initial compression. After cold pressurization to a nominal pressure 10% higher than desired, the pressure was decreased down to 300 MPa. The temperature was monitored by a factory-calibrated C-type (W-5Re/W-26Re) thermocouple, which gives an uncertainty of ±3 °C. Following Masotta et al. (2020), the experiments were carried out by heating the starting glass to superliquidus condition of 1,300 °C at a rate of 80 °C min^{-1}. After 30 min, the temperature was cooled to 1,050 °C at the same rate of 80 °C min^{-1} (*Experimental Set CR*). This isothermal condition was kept constant for 0.25 (*CR-025*), 0.5 (*CR-05*), 1 (*CR-1*), 4 (*CR-4*), 24 (*CR-24*), and 72 (*CR-72*) hours, before isobaric quench at a rate of 100 °C s^{-1} (Table 1).

As a whole, *Experimental Set ISO*, *Experimental Set ΔP*, and *Experimental Set CR* were carried out at the temperatures (i.e., 1,100, 1,075, and 1,050 °C) more frequently encountered during the crystallization of clinopyroxene at Mt. Etna volcano (e.g., Mollo et al., 2018). Similarly, the pressure condition of 300 MPa corresponds to a magma storage region at an intermediate depth of 7-13 km (Murru et al., 1999) where microphenocrysts of clinopyroxene initiate to nucleate and grow during magma ascent towards the surface (e.g., Mollo et al., 2015b). In this context, *Experimental Set ISO* approached from the solidus directly to the subliquidus temperature (i.e., nominal ΔT = 0) in order to quantify the textural parameters of clinopyroxene under interface-controlled growth regimes. Conversely, *Experimental Set ΔP* and *Experimental Set CR* were designed to impose variable supersaturation conditions (i.e., actual ΔT = 14-125 °C; Table 1), leading to diffusion-controlled growth regimes and clinopyroxene textural changes.

2.2. Image processing and CSD correction

Photomicrographs of the experimental products were collected in backscattered electron (BSE) mode of a JEOL 6500F field emission gun scanning electron microscope (FE-SEM) equipped with an energy-dispersive spectrometer (EDS) detector at the HP-HT Lab of INGV.

The acquired photomicrographs were processed via NIH ImageJ software and reduced to binary type images (i.e., black and white color) by grey level thresholding (i.e., image segmentation; Armienti, 2008). The segmentation method was employed to identify clinopyroxene microphenocrysts and microlites relative to other mineral phases (Fig. 1). The uncertainty associated with the segmentation process and the identification of larger crystals growing by attachment of smaller ones has been evaluated according to the method reported in Pontesilli et al. (2019) and based on the addition/subtraction of pixel layers around each crystal in the binary image. A Matlab© code (see Supplementary Material 1) was developed to perform image processing operations in conjunction with NIH ImageJ. The retrieved textural parameters were 1) the equal-area best-fit ellipses and lengths of major (L) and minor (W) axes (Fig. 1), 2) the surface area per unit volume (S_v^P as 3D aspect ratio; Table 1), and 3) the area fraction of a given population within a plane that is comparable to its volume fraction (ϕ). Following one of the most common methods reported in literature (cf. Pontesilli et al., 2019 and references therein), L and W data were used to calculate the maximum growth rate (G_{max} in mm s^{-1}) of clinopyroxene, as an average of the ten largest crystals measured in each experimental run (Supplementary Material 2):

$$G_{max} = (L\,W)^{0.5} / (2\,t) \quad (1)$$

where t is the experimental time.

The magnitude of S_v^P was determined for the experimental crystals as (Hammer, 2006; First and Hammer, 2016):

$$S_v^P = S_v^T / \phi \quad (2)$$

S_v^T is the total interfacial area of a population per unit volume of sample and can be expressed as $2 \times N_L$, where N_L is the density of phase boundary intersections in a given length of randomly oriented test line. The Matlab© code from this study allows to overlay the desired number of circular test lines over a binary type image (Fig. 1) and determine the N_L value by counting the locus of points where crystal-melt boundaries intersect the test lines. The lower is the magnitude of S_v^P parameter, the higher is the crystal euhedrality. Therefore, clinopyroxene crystals characterized by S_v^P < 1,000 mm^{-1} are interpreted as euhedral, whereas crystal with S_v^P >1,000 mm^{-1} are anhedral (Hammer, 2008). S_v^P data listed in Table 1 are the mean resulting from the analysis of eight binary type images for sample, each one overlaid by six circles with radius variable as a function of BSE image magnification (Fig. 1).

CSD analysis was carried out on BSE images of natural rock samples from 2011-2012 lava fountains outpoured at Mt. Etna volcano. Textural data were collected at ×500 and ×100 magnifications for microlites (<0.1 mm) and microphenocrysts (≥0.1 mm) populations, respectively, and then combined each other to obtain one single CSD curve. Intersection planar data were converted in volume data by applying stereological correction (Higgins, 2000), in order to gain information on the contribution of larger crystals to the population of smaller ones. This correction method accounts for 1) potential cut-section effects in case of larger crystals are cut by a plane shifted with respect to the center, therefore contributing to smaller crystal populations, and 2) intersection probability effects when, for a poly-disperse distribution, smaller crystals are less likely to be intersected by a plane than larger crystals (Higgins, 2000). The crystal shape, assumed as the crystal aspect ratio S:I:L of short:intermediate:long dimensions (Higgins, 2000), was determined by the Excel© spreadsheet *CSDslice* developed by Morgan and Jerram (2006). Through this model, 2D raw data were compared with a crystal habit database (i.e., S:I:L of 1:10:10, 1:1:10, and 1:1:1) to constrain the five best-matching crystal shapes. The best linear binning was selected for each sample by the procedure

reported in Armienti (2008) for the minimization of residuals between the particles effectively measured and those re-calculated by CSD analysis (zeroth moment of the distribution):

$$N_{tot} = Area \sum L_i \, N_V(L_i) \tag{3}$$

where L_i is the major axis length of crystal and N_V is the volumetric number density. This latter parameter is calculated as the ratio of the area number density (N_A) to the characteristic crystal size (L_D). The routine of Armienti (2008) requires also the minimization of residuals between the measured volume crystal fraction and the volume resulting from CSD analysis (third moment of the distribution):

$$V_f = \sum N_V\,(L_i)\,\frac{4}{3}\pi\left(\frac{L_i}{2}\right)^3 = \frac{\pi}{6}\sum {L_i}^3 N_V(L_i) \tag{4}$$

According to Eqns. (3) and (4), a linear binning ΔL of 0.02 mm was derived, for a total of 21 classes ranging from 0.006 to 0.406 mm. Crystals with L < 0.006 mm (i.e., artefacts caused by image segmentation) and crystal fragments at the edge of photomicrographs were removed from the dataset (Armienti et al., 1994). The program *CSDCorrection*s 1.38 of Higgins (2000) was finally employed to calculate a binned CSD curve for different crystal size classes by specifying the crystal shape values reported in Supplementary Material 3, rock fabric of massive type, and crystal roundness factor of 0.5. The formulated CSD diagrams are in the form of semi-logarithmic plots based on ln *N(L)* vs. *L* that describe the evolution of crystal size as (Marsh, 1988):

$$\ln N(L) = \frac{-L}{G\,\tau} + \ln N_0 \tag{5}$$

where $N(L)$ is the number of crystals per size of length L per unit volume (i.e., the density distribution of crystals per unit volume per bin size), G is the crystal growth rate, τ is the time of a system crystallizing at steady state, and N_0 is the nucleation density (i.e., the number of crystals of zero size). When the dominant size of the crystal population results from steady growth over an appropriate duration of time, the linear regression fit of CSD curve has slope $m = 1 / (G \times \tau)$ and intercept $b = \ln(N_0)$. According to previous works focused on crystallization kinetics (see the review study of Giuliani et al., 2020 and references therein), the decrease of m with increasing crystal size may reflect the growth of early-formed nuclei by agglomeration and attachment. Under such kinetic growth conditions, both m and b parameters are strictly correlated with the variation of temperature as a function of time, and G_{max} linearly decreases with decreasing $\Delta T/\Delta \tau$ (cf. Giuliani et al., 2020). CSD statistics were obtained from the quantitative study of 16 thin sections and 243 photomicrographs. CSD plots were constructed considering ~1,500-4,000 crystals.

2.3. Microanalysis

Major element concentrations were obtained at the HP-HT Lab of INGV using a JEOL-JXA8200 electron probe micro-analyzer (EPMA) equipped with five wavelength dispersive spectrometers (Supplementary Material 4). For glasses, a slightly defocused 3 μm beam was used with a counting time of 5 s on background and 15 s on peak. For crystals, beam size was 1 μm with a counting time of 20 and 10 s on peak and background, respectively. The following standards were used for calibration: jadeite (Si and Na), corundum (Al), forsterite (Mg), andradite (Fe), rutile (Ti), orthoclase (K), barite (Ba), apatite (P), spessartine (Mn) and chromite (Cr). Sodium and potassium were analyzed first to prevent alkali migration effects. The precision of the microprobe was measured through the analysis of well-characterized synthetic standards. Based on counting statistics, analytical uncertainties relative to their reported concentrations indicate that precision and accuracy were better than 5% for all cations.

3. Results

3.1. Textural features

Selected BSE photomicrographs representative of run products from *Experimental Set ISO*, *Experimental Set ΔP*, and *Experimental Set CR* are displayed in Figs. 1 and 2 (note that photomicrographs of all the experiments are reported in Supplementary Material 2). The mineral assemblage consists of abundant clinopyroxene and titanomagnetite, with subordinate plagioclase (in order of crystallization sequence).

Clinopyroxene crystals from *Experimental Set ISO* show euhedral morphologies, with a great number of well-faced crystals (Figs. 1 and 2) and L_{max} variable from 0.07 to 0.23 mm (Supplementary Material 2). Run products are characterized by a dense mosaic of either isolated or aggregated microlites, suggesting rapid attainment of an interface-controlled crystal growth regime. Indeed, most of clinopyroxene crystallization initiated upon crossing the glass transition temperature (Tg = 723 °C, Giordano et al., 2005) and further continued over time (i.e., there is no effective ΔT caused by cooling and/or decompression). The amount of residual glass found in the experimental charges increases with increasing T and $H_2O_{initial}$ (Figs. 1 and 2, and Supplementary Material 2). In contrast, the presence of CO_2 lowers the amount of H_2O dissolved in the melt, raising the liquidus temperature of the experimental system and increasing the crystal content (Supplementary Material 2).

Clinopyroxene crystals from *Experimental Set ΔP* consist of sector-zoned crystals with prismatic shapes and well-formed planar edges (Figs. 1 and 2, and Supplementary Material 2). L_{max} ranges from 0.02 to 0.25 mm, depicting an increasing trend with increasing T and $H_2O_{initial}$. Under slow decompression regimes, the crystal size substantially increases due to the effect of sluggish decompression-driven crystal growth kinetics. Therefore, L_{max} measured for *ΔPs-1100-5H2O* (0.14-0.25 mm) is much higher than that determined for *ΔPf-1100-5H2O* (0.06-0.09 mm). Notably, the lack of anhedral (hopper to dendritic) forms in both *ΔPs* and *ΔPf* experiments accounts for the effect of

relative slow ΔT (14-30 °C; Table 1), consistently with previous literature data (see the review study of Giuliani et al., 2020).

Clinopyroxene crystals from *Experimental Set CR* show substantial textural differences as a function of relaxation time (Figs. 1 and 2, and Supplementary Material 2). *CR-1050-025*, *CR-1050-05*, and *CR-1050-1* are characterized by the ubiquitous occurrence of acicular and skeletal crystals, whereas *CR-1050-4*, *CR-1050-24*, and *CR-1050-72* exhibit clear euhedral morphologies (Fig. 2 and Supplementary Material 2). The shift from a diffusion-controlled to an interface-controlled crystal growth conditions is marked, taking place in a time interval comprised between 1 and 4 h. Once crystallization proceeds under nucleation-dominated regimes, L_{max} ranges from 0.07 to 0.10 mm for *CR-1050-025*, *CR-1050-05*, and *CR-1050-1*. In contrast, due to superimposition of growth-dominated regimes, L_{max} ranges from 0.08 to 0.25 mm for *CR-1050-4*, *CR-1050-24*, and *CR-1050-72*.

3.2. Crystal content variation

Fig. 3 shows the variation of clinopyroxene content (% area) in *Experimental Set ISO*, *Experimental Set ΔP*, and *Experimental Set CR*.

As the target temperature increases, the degree of crystallization decreases from 28% to 18% and from 21% to 5% for *Experimental Set ISO* and *Experimental Set ΔP*, respectively (Fig. 3a). A similar decrease is attained by increasing $H_2O_{initial}$, whereas the crystal content slightly increases by ~4% when CO_2 is added to the experimental charge.

Experimental Set CR exhibits the highest clinopyroxene content within the whole data set. As the relaxation time increases, the degree of crystallization slightly decreases from 37% to 32% (Fig. 3b). A modest drop in crystal content takes place in the time interval comprised between 1 and 4 h, once the crystallization regime shifts from nucleation-dominated to growth-dominated regimes.

3.3. Clinopyroxene euhedrality

Fig. 4 shows the variation of S_v^P determined for *Experimental Set ISO*, *Experimental Set ΔP*, *and Experimental Set CR*. As temperature and/or H_2O content increase, clinopyroxene S_v^P decreases with decreasing the surface area of crystals per unit volume. Moreover, the probability of phase boundary intersections increases with increasing the number of crystals, thus leading to most of trends defined for S_v^P (Fig. 4).

For *Experimental Set ISO* (730-477 mm^{-1} S_v^P) and *Experimental Set ΔP* (548-113 mm^{-1} S_v^P), the euhedrality of clinopyroxene increases with increasing temperature and $H_2O_{initial}$ (Fig. 4a). Both isothermal and decompression data confirm that values of S_v^P < 1,000 mm^{-1} account for the development of well-faced morphologies (cf. Hammer, 2008).

On the other hand, the magnitude of crystal euhedrality radically changes in *Experimental Set CR* (Fig. 4b). S_v^P ranges from 1,365 to 1,194 mm^{-1} for *CR-1050-025*, *CR-1050-05* and *CR-1050-1*. A much more restricted S_v^P range of 896-815 mm^{-1} is measured for *CR-1050-4*, *CR-1050-24*, and *CR-1050-72*. Since the experimental cooling rate was fixed and only the relaxation time was changed, the abrupt variation of S_v^P is a proxy for the control of relaxation time on the crystallization regime, after that the system is subjected to an early stage of undercooling (Arzilli et al., 2018; Pontesilli et al., 2019).

3.4. Compositional features

Chemical changes of residual glasses and coexisting clinopyroxene crystals will be the object of a forthcoming and more comprehensive work on cation partitioning under isobaric-isothermal vs. cooling-decompression conditions. Here we briefly summarize the most important compositional features of the experimental charges (Fig. 5):

1) according to the TAS (total alkali vs. silica) classification diagram, the glass chemistry (Fig. 5a) can be divided into two groups as a function of temperature and $H_2O_{initial}$ conditions (i.e., the degree of crystallization);

2) at high-*T* (1,100 °C), high-$H_2O_{initial}$ contents (5 wt.%), residual melts exhibit basaltic-trachybasaltic compositions (Fig. 5a) similar to those of recent (post-1971) eruptions at Mt. Etna volcano (natural data set from Mollo et al., 2018);

3) at low-*T* (1,050-1,075 °C), low-$H_2O_{initial}$ contents (0-2 wt.%), residual melts are more differentiated, resembling trachybasalts to basaltic trachyandesites erupted during the historic (pre-1971) period of activity (Fig. 5a);

4) clinopyroxene chemistry follows the same evolutionary path depicted by the melt phase, with the exception of sector-zoned crystals obtained under slow and fast decompression conditions (Fig. 5b);

5) at high-*T*, high- $H_2O_{initial}$ contents, clinopyroxene crystals are enriched in Di (diopside) + Hd (hedenbergite) and depleted in CaTs (Ca-Tschermak) + CaTiTs (CaTi-Tschermak) components (Fig. 5b);

6) at low-*T*, low- $H_2O_{initial}$ contents, the amount of Di + Hd in clinopyroxene crystals decreases at the expense of CaTs + CaTiTs (Fig. 5b), responding to the higher degree of melt differentiation;

7) kinetic effects in decompression experiments produce sector-zoned clinopyroxene crystals characterized by Di-Hd-rich, CaTs-CaTiTs-poor hourglass (or basal) sectors {- 1 1 1} and Di-Hd-poor, CaTs-CaTiTs-rich prism sectors {1 0 0};

8) the chemistry of hourglass sectors {- 1 1 1} closely matches with that of experimental crystals obtained at high-*T*, high-$H_2O_{initial}$ contents, as well as with the natural hourglass sectors of phenocrysts from recent eruptions at Mt. Etna volcano;

9) the chemistry of prism sectors {1 0 0} depicts a distinct crystal population, with substantial enrichment in Tschermak components, as also observed for the prism sectors of clinopyroxene phenocrysts from recent eruptions;

10) overall, the development of sector-zoned clinopyroxene crystals from decompression experiments is consistent with kinetic cation partitioning caused by decompression and degassing of Etnean magmas (Ubide and Kamber, 2018; Masotta et al., 2020), in conjunction with charge balance

mechanisms due to $Si^{4+} \leftrightarrow Al^{3+}$ substitution in the tetrahedral site and $Mg^{2+} + Fe^{2+} \leftrightarrow Ti^{4+} + Fe^{3+}$ exchange in octahedral sites (Mollo et al., 2018).

4. Discussion

4.1. Clinopyroxene growth rate and thermodynamic constraints

Values of G_{max} for clinopyroxene crystals from this study are listed in Table 1 and plotted in Fig. 6 on a logarithmic scale as a function of the different experimental conditions.

For *Experimental Set ISO* and *Experimental Set ΔP*, the value of G_{max} is positively correlated with temperature and $H_2O_{initial}$, but this correlation is more evident for the decompression experiments rather than isothermal runs where G_{max} values overlap within their uncertainty (Fig. 6a). Major changes of G_{max} are measured as the experimental conditions change in the order of *Experimental Set ISO* (~10^{-15}-10^{-14} mm s^{-1}), *Experimental Set ΔPs* (~10^{-14}-10^{-12} mm s^{-1}), and *Experimental Set ΔPf* (~10^{-10}-10^{-9} mm s^{-1}).

Under isothermal conditions, the nucleation of clinopyroxene initiates when the system is heated from the room temperature to the target temperature of the experiment. At nominal $\Delta T = 0$, the degree of melt supersaturation is expected to be close to near-equilibrium crystallization conditions (Baker, 2008). The bulk system tends to minimize the interfacial free energy between small size crystals and the surrounding melt (Bonechi et al., 2020; Masotta et al., 2020), resulting in a closer approach to equilibrium far from dynamic undercooling conditions encountered by magmas rising along the shallower parts of a plumbing system and/or along the volcanic conduit (Mollo and Hammer, 2017 and references therein). Therefore, the rate of attachment/detachment reactions of cations from the melt onto the crystalline surface (and *vice versa*) approaches a steady-state condition in a relatively short experimental time (Kirkpatrick, 1981, 1983; Pontesilli et al., 2019).

H_2O exsolution in decompression experiments raises the liquidus region of the melt, thus imposing melt supersaturation (i.e., ΔT = 14-30 °C; Table 1) and facilitating the growth of

clinopyroxene (Simakin et al., 2003; Orlando et al., 2008; Hammer, 2008; Mollo and Hammer, 2017). Moreover, Fig. 6a shows that the magnitude of G_{max} from H_2O-CO_2-bearing charges (ΔT = 14-18 °C) is systematically lower than that measured for H_2O-bearing charges (ΔT = 16-30 °C), accounting for the presence of CO_2 and its rival effect on H_2O contents dissolved in the melt. This observation is consistent with the knowledge that a slow mobility of Si and Al in low-*T*, low-H_2O melts is rate-limiting for divalent Ca and Mg cations, and the addition of tetrahedral groups to the surface of a crystal is the rate-controlling step of the crystal growth (Nascimento et al., 2004).

For *Experimental Set CR*, the effect of ΔT (125 °C) on G_{max} corresponds to a large degree of melt supersaturation and the crystal growth regime shifts from interface-controlled to diffusion-controlled (Lofgren, 1974; Sunagawa, 1981; Webb and Dingwell, 1995). Nonetheless, as reported in Pontesilli et al. (2019), relaxation kinetics control the crystal growth as a function of dwell time. G_{max} decreases by orders of magnitude, from ~10^{-11} (*CR-1050-025*) to ~10^{-15} mm s^{-1} (*CR-1050-72*) (Fig. 6b). Short relaxation times of 0.25-1 h favor melt supersaturation and diffusion-limited growth regimes, with more pronounced nucleation of crystals showing disequilibrium textures (Mollo et al., 2010, 2012; Lofgren, 1974; Sunagawa, 1981). As the relaxation time increases up to 72 h, an interface-controlled growth promotes formation of euhedral crystals (Fig. 6b). This textual maturation pairs with the progressive decay of G_{max} towards a steady-state condition (Hammer, 2006, 2008; Pontesilli et al., 2019). Superheating can also fundamentally alter the structure of silicate melts and variable superheating intensity can cause textural differences in subsequently nucleated crystals (First and Hammer, 2016; First et al., 2020). However, it has been also observed that the relaxation of a basaltic melt at 1,300 °C occurs in a very short time (from milli- to micro-seconds) and can be considered independent on the superheating path used in laboratory (Vetere et al., 2013, 2015).

The dependence of crystal growth rate on the degree of undercooling can be calculated as:

$$G \propto \exp\left(\frac{-E}{RT_{exp}}\right)\left[1-\exp\left(\frac{\Delta H\,\Delta T}{R\,T_{exp}\,T_{liquidus}}\right)\right] \quad (6)$$

Eq. (6) from Armienti (2008) is the rearranged form of equations reported in Cashman (1990) and Toramaru (1991). R is the gas constant (8.310 J mol^{-1} K^{-1}), ΔH is the molar enthalpy of fusion (50-100 kJ mol^{-1}; Weill et al., 1980; Toramaru, 1991), and E is the activation energy of clinopyroxene crystal growth (200-377 kJ mol^{-1}; Toramaru, 1991; Yilmaz et al., 1996; Karamarov et al., 2000; Burkhard, 2005). T_{exp} is the experimental temperature, whereas $T_{liquidus}$ is the liquidus temperature of 1,150-1,220 °C, as determined by rhyolite-MELTS thermodynamic simulations carried out at 300 MPa, 0-5 wt.% H_2O, and NNO+2 buffer (v.1.2.0; Gualda et al., 2012). Within these thermodynamic constraints, the growth rates estimated for clinopyroxene are ~10^{-11}-10^{-9} mm s^{-1} (*Experimental Set ΔPf*), ~10^{-13}-10^{-12} mm s^{-1} (*Experimental Set ΔPs*), and ~10^{-15}-10^{-14} mm s^{-1} (*Experimental Set CR*). Fig. 6a shows that G_{max} values modeled for *Experimental Set ΔP* are comparable with those measured in laboratory, also corroborating the strong control of ΔT on clinopyroxene crystallization. However, for *Experimental Set CR*, the derived thermodynamic quantities match only with G_{max} measured for *CR-1050-24* and *CR-1050-72* experiments (Fig. 6b), whereas Eq. (6) fails to precinct G_{max} at shorter relaxation times of 0.25, 0.5, 1, and 4 h. From a comparative textural analysis emerges that crystal growth mismatches are caused by nucleation kinetics and abundant dendritic crystallization (Fig. 2). A higher time-averaged nucleation rate over a shorter relaxation time causes a more pronounced melt supersaturation and a diffusion-controlled growth regime (Toramaru, 1991). This agrees with 4D crystallization experiments conducted by Arzilli et al. (2019) on a trachybasalt erupted during 2001 eruption at Mt. Etna. It is interesting to note that, in the first part of the experiments, crystallization was induced by decreasing the temperature from superliquidus to subliquidus conditions, with a dwell time at the final temperature of 4 h. During this dwell time, blocky and prismatic clinopyroxene and oxide crystals grew. After 4 h at subliquidus condition, the temperature was further decreased to induce a continuous increase of undercooling. At $\Delta T \geq 60$ °C, dendritic clinopyroxene crystals developed by diffusion-controlled branching growth in multiple directions to reach a maximum size of 40 μm. Clinopyroxene nucleated heterogeneously on plagioclase and the equilibrium crystal content was achieved in ~3 min (Arzilli et al., 2019). In the present study, however, as the relaxation

time increases to 24-72 h, early clinopyroxene dendritic crystals are replaced by euhedral morphologies typical of interface-controlled growth regimes (Supplementary Material 2). The attachment of cations on the crystal surface increases with increasing the relaxation time (Kirkpatrick, 1981, 1983) and euhedral morphologies are more adequately modeled by Eq. (6) for *CR-1050-24* and *CR-1050-72* experiments (Fig. 6b).

According to clinopyroxene growth kinetics, the transition between interface-controlled and diffusion-controlled regimes is governed by a screw dislocation growth model, where the crystal-melt interface is assumed to be smooth and growth takes place at step sites provided by screw dislocations (Kirkpatrick et al., 1981, 1983). The thermodynamic equations behind screw dislocations are approximated to a temperature-dependent growth rate system (Nascimento et al., 2004):

$$G = f\,\frac{D}{\lambda}\left[1 - \exp\left(-\frac{|\Delta G|}{R\,T}\right)\right], \tag{7}$$

$$f = \frac{\lambda\,\Delta G}{4\,\pi\,\sigma\,V}, \text{ and} \tag{8}$$

$$\sigma = \frac{\alpha\,\Delta H\,\lambda}{V} \tag{9}$$

where D is the diffusion coefficient of slow diffusing Si and Al cations in the melt (~10^{-14}-10^{-15} m^2 s^{-1} at 1,050-1,100 °C; Zhang et al., 2010). λ (2.7 Å) and V (7.59 × 10^{-5} m^3 mol^{-1}) are the diameter of the diffusing building molecules and the molar volume of a pure diopside, respectively (data from Nascimento et al., 2004). ΔG is the Gibbs free energy of clinopyroxene formation estimated by rhyolite-MELTS at the experiment conditions (~7-22 kJ mol^{-1}; Gualda et al., 2012). The parameters f, σ, and α are the fraction of preferred growth sites at the crystal interface, the crystal-melt surface energy, and the reduced surface energy, respectively (cf. Nascimento et al., 2004 and references therein). The crystal growth path modeled through this approach is depicted as green (1,050 °C) and

blue (1,100 °C) trends in Fig. 7. In order to isolate the effect of ΔT, the modeled trends are compared with values of G_{max} (green and blue diamonds for 1,050 and 1,100 °C, respectively) from decompression and cooling rate experiments conducted over similar relaxation times (i.e., on the order of minutes for *ΔPf-1100-2H2O, ΔPf-1100-5H2O, ΔPf-1100-H2O+CO2, ΔPf-1050-2H2O, ΔPf-1050-5H2O, ΔPf-1050-H2O+CO2, CR-1050-0.25, CR-1050-0.5*). Small values of ΔT from *Experimental Set ΔPf* promote an interface-controlled growth (Fig. 7) and the development of large, euhedral sector-zoned crystals characterized by well-formed prismatic morphologies (Figs. 2 and 4, and Supplementary Material 2). The lack of skeletal shapes and formation of sector-zoned clinopyroxene crystals indicate sluggish crystallization kinetics typically observed at $\Delta T \leq 30$ °C (Kouchi et al., 1983; Ubide et al., 2019a; Giuliani et al., 2020; Masotta et al., 2020). Sector-zoned crystals have identical three-dimensional atomic configurations, but the surface of each individual growing sector has a specific two-dimensional atomic arrangement (Dowty, 1976 and references therein). Adjacent crystal regions grow simultaneously and form crystallographically nonequivalent faces with distinctively intersectoral chemical variations, with Di-Hd-rich, CaTs-CaTiTs-poor hourglass sectors {- 1 1 1} and Di-Hd-poor, CaTs-CaTiTs-rich prism sectors {1 0 0} (Fig. 5). These intersectoral differences emerge only under the effect of small ΔT (Kouchi et al., 1983; Masotta et al., 2020), when slow crystal growth kinetics ensure the attainment of clinopyroxene euhedrality (Fig. 4a). As a consequence, the different types of cation substitutions in the sectors reflect the variable spatial structural distributions of M and T sites as a function of the growth velocity of polyhedral sectors (Dowty, 1976 and references therein) rather than the disequilibrium advancement of a skeletal crystal surface via kinetic roughening transition (Sunagawa, 2005).

According to the above criteria, Fig. 7 displays thermodynamic modeling paths that confirm transition between interface-controlled and diffusion-controlled growth at $\Delta T \geq 30$ °C, as texturally constrained by our experimental data set. A diffusion-controlled growth regime develops only when large ΔT from *Experimental Set CR* operate in combination with short relaxation times (Fig. 7). The

interface kinetics become extremely fast and tiny, anhedral clinopyroxene crystals develop from supersaturated melt regions where nucleation kinetics strongly prevail over the growth (Figs. 2 and 4b, and Supplementary Material 2). Kinetic effects due to different cation diffusivities in the melt overprint the control exercised by the structural sites of the advancing crystal surface (Giuliani et al., 2020). As a result, there is no evident control of crystal structural sites on cation incorporation and precise chemical correlations amongst the zoning patterns of skeletal clinopyroxene crystals cannot be identified (Kouchi et al., 1983; Masotta et al., 2020).

4.3 Parameterization of clinopyroxene growth kinetics

Growth rates obtained in this study are compared in Fig. 8a with those measured by previous experimental works investigating basaltic and trachybasaltic compositions that reproduce the overall intrinsic variability of rocks from the Monte Maletto Formation (Baker, 2008; Mollo et al., 2013; Pontesilli et al., 2019; Masotta et al., 2020). As pointed out by Bonechi et al. (2020), there is a strong control of melt composition on the crystal growth rate due to polymerization effects caused by an increasing number of tetrahedral sites relative to octahedral sites, thereby increasing the melt viscosity and lowering the diffusivity of elements in the melt. Accounting also for the major effects of T and H_2O on melt viscosity, all the parameterized experiments were performed at conditions analogous to those estimated for magmas erupted at Mt. Etna volcano (i.e., P = 0.1-1,000 MPa, T = 1,050-1,150 °C, H_2O = 0-4 wt.%, fO_2 = NNO+1.5-NNO+2, ΔT = 75-233 °C, and CR = 0.001-100 °C s^{-1}; see the review study of Mollo et al., 2018 and references therein). Fig. 8a shows that G_{max} decreases by approximately six orders of magnitude, from ~10^{-9} to ~10^{-15} mm s^{-1}, as the relaxation time increases from 0.08 to 72 h (Fig. 8a). Statistical calculations were carried out on the experimental data set with the Statgraphics Centurion 18® algorithm (Statpoint Technologies, Inc., Warrenton, VA, USA) by running a weighted least square (WLS) regression analysis. While in ordinary least square (OLS) regressions the standard deviation (σ) of error is assumed constant over all values of the explanatory variable, in WLS regressions the efficiency of estimation is maximized by giving to each data its

proper amount of influence (i.e., weight *w*) over the estimate. This is especially important in modeling of logarithmic data sets that are susceptible to uncertainties associated with the linearization of the model (i.e., heteroskedasticity; Hair et al., 1995). On this basis, error minimization is attained by 1) incorporating weights into the fitting criterion and 2) performing Monte Carlo propagation of errors (Ratkowsky, 1990). The general form of WLS model is written in matrix notation as:

$$\mathbf{Y} = \mathbf{X\beta} + \boldsymbol{\varepsilon} \tag{10}$$

where $\mathbf{Y}$ = ($n \times 1$) vector of y observations, $\mathbf{X}$ = ($n \times k$) matrix of x variables, and $\boldsymbol{\beta}$ = ($k \times 1$) vector of β regression coefficients. The $\boldsymbol{\varepsilon}$ = ($n \times 1$) vector of random errors ε is expressed as ($\mathbf{0}$, $\sigma^2\mathbf{W}$). In OLS, ε has mean equals to zero and variance close to the square of the standard deviation [$var(\varepsilon) = \sigma^2$]. Conversely, in WLS, ε does not have constant variance [$var(\varepsilon) = \sigma^2/w$] and the weight given to each observation is inversely proportional to the variance of the explanatory variable. $\mathbf{W}$ represents an ($n \times n$) diagonal matrix with diagonal entries corresponding to weights and $\mathbf{Var(\varepsilon)} = \mathbf{W^{-1}\sigma^2}$. The solution of Eq. (10) is:

$$\boldsymbol{\beta}^* = \frac{\mathbf{X^T W Y^*}}{\mathbf{X^T W X}} \tag{11}$$

where $\boldsymbol{\beta}^*$ and $\mathbf{Y}^*$ are estimates of $\boldsymbol{\beta}$ and $\mathbf{Y}$, respectively, and $\mathbf{X^T}$ is the transpose of matrix $\mathbf{X}$. WLS regression of experimental data displayed in Fig. 8a have the following form:

$$\ln G_{max} = \beta_0 + \beta_1 \ln t_{max} \tag{12}$$

The best predicting model for G_{max} has been calculated by optimizing the weighted fitting criterion and estimating the variance of the data set for each fixed covariate vector in Eq. (11). This statistical

approach allows to downweight outliers and reduce their impact on the overall model. The least square minimization of Eq. (12) yields β_0 = -5.512 (±0.041 $\sigma_{\beta 0}$) and β_1 = -0.778 (±0.012 $\sigma_{\beta 1}$). The coefficient of determination (R^2), standard error of estimate (SEE_{Gmax}), and mean absolute error (ε) are 0.977, 0.242, and 0.181, respectively. As a further error test, the regression constants β_0 and β_1 have been also recalculated by perturbing Eq. (12) via Monte Carlo simulations over a normal distribution with the mean centered on the original value of G_{max} and with deviation close to SEE_{Gmax} (Hair et al., 1995). After generating 1,000 sets of hypothetical regression coefficients, results from probability density functions confirm data from least square minimization. Therefore, it is calculated that ~68% of β_0 (Fig. 8b) and β_1 (Fig. 8c) have uncertainties of ±0.039 $\sigma_{\beta 0}$ and ±0.011 $\sigma_{\beta 1}$, respectively. Since most of the calibration data were obtained at 0 and 2 wt.% H_2O contents in both the present study and previous works, WLS regressions have been replicated on two distinct data sets for anhydrous (0 wt.% H_2O) and hydrous (2 wt.% H_2O) experiments. These calculations yield very similar regression coefficients ($^{anhydrous}\beta_0$ = -5.589 vs. $^{hydrous}\beta_0$ = -5.521, as well as $^{anhydrous}\beta_1$ = -0.771 vs. $^{hydrous}\beta_0$ = -0.778) and errors of estimate ($^{anhydrous}SEE_{Gmax}$ = 0.251 vs. $^{hydrous}SEE_{Gmax}$ = 0.244). Attainment of comparable regression coefficients points out that an increase in H_2O of 5 wt.% or an increase in temperature of 50 °C produce a similar magnitude of increase in G_{max} (Fig. 6a) and similar clinopyroxene contents (Fig. 3a). For example, at constant T, G_{max} increases by 20% as the melt-H_2O content increases from 0 to 5 wt.%. Analogously, at constant H_2O concentration, G_{max} increases by 18% as T increases from 1,050 to 1,100 °C. As previously observed by Pontesilli et al. (2019), the magnitude of G_{max} is mostly dictated by the duration of crystal growth (Fig. 6b), in concert with the increase in crystal size (L_{max}) and the clinopyroxene euhedrality (S_v^P).

Recalling the crystal size distribution (CSD) theory and Eq. (5), the crystal nucleation rate is related to the growth rate as $J = N_0 \times G$. By assuming $G = G_{max}$ and $\tau = t_{max}$, we can substitute Eq. (12) into the slope $m = 1 / (G \times \tau)$ of Eq. (5) and then rearrange this algebraic expression to isolate the crystallization time of clinopyroxene forming under naturally undercooling conditions:

$$G_{\max} = t_{max}^{\beta_1} \exp\beta_0, \quad (13)$$

$$m = -\frac{1}{\left|t_{max}^{(\beta_1+1)} \exp\beta_0\right|}, \text{ and} \quad (14)$$

$$t_{max} = \left(-\frac{1}{m \exp\beta_0}\right)^{\left(\frac{1}{\beta_1+1}\right)} \quad (15)$$

The overall uncertainty associated with the estimate of t_{max} has been determined by propagating into Eq. (15) the values of SEE_{Gmax}, $\sigma_{\beta 0}$, and $\sigma_{\beta 1}$ via Monte Carlo simulations. Density estimations indicate that the uncertainty of t_{max} varies from 22% to 28%, with an average close to 26% (Fig. 8d). The calculation of t_{max} can be performed through the Microsoft Excel spreadsheet available online as Supplementary Material 5.

4.4. Application to magma dynamics at Mt. Etna volcano

Mt. Etna is one of the most studied and monitored volcanoes in the world. The persistent eruptive activity of Mt. Etna threatens the populations living in its shadow, also causing regional climate changes in Sicily and the temporary closure of the Fontanarossa International airport of Catania. The plumbing system is governed by frequent input and mixing of primitive, volatile-rich magmas rising from a deeper (~10 km) storage region into shallower reservoirs (3-5 km) and, occasionally, ponding within the volcanic edifice (0.5-2.5 km; Patanè et al., 2003; Corsaro et al., 2009; Ubide and Kamber, 2018; Mollo et al., 2018). Abundant volatile exsolution and degassing are the key mechanisms controlling mineral and melt compositions, degree of crystallization, magma ascent velocity, and eruptive style (Armienti et al., 2007; Lanzafame et al., 2013). Magma can be erupted either quickly through deep dykes feeding eccentric eruptions (i.e., bypassing the central conduits) or gradually through the central conduits feeding shallow reservoirs (Ubide and Kamber, 2018).

A cyclic fountaining activity occurred at the New Southeast Crater (NSEC) in 2011–2012 and 2013, including normal paroxysmal sequences and energetic episodes with high eruption columns (7–8 km above the vent). A detailed multi-disciplinary data set referring to these eruptions can be found in literature, including mineral and melt compositions, volcanological constraints, thermal mapping, and structural surveys (Andronico et al., 2005; Ferlito et al., 2009, 2012; Mollo et al., 2015b, 2018; Perinelli et al., 2016; Giuffrida and Viccaro, 2017; Giuffrida et al., 2018; Giacomoni et al., 2018). In this study, we focus on clinopyroxene microphenocrysts and microlites from fourteen 2011-2012 scoria clasts that are representative of 12/01/2011, 18/02/2011, 10/04/2011, 12/05/2011, 30/07/2011, 20/08/2011, 29/08/2011, 08/09/2011, 15/11/2011, 05/01/2012, 04/03/2012, 18/03/2012, 01/04/2012, and 24/04/2012 lava fountains (Supplementary Material 3). These samples have variable vesicularity (15-30%) and porphyritic index (30-60%), but a uniform phase assemblage of olivine + clinopyroxene + plagioclase + titanomagnetite + glass (see Supplementary Material 3 and Giacomoni et al., 2018 for a detailed petrographic description). By analyzing cation redistributions in 2011-2012 clinopyroxene and titanomagnetite crystals, Mollo et al. (2015b) documented the ability of microphenocrysts and microlites to record variable undercooling histories between the sub-liquidus temperature of the magmatic reservoir and the closure temperature of crystal growth, when the kinetics and energetics of solidification were rapidly frozen-in at the time of eruption.

The saturation conditions of clinopyroxene crystals from 2011-2012 lava fountains, prior to dynamic ascent of magma towards the surface, have been estimated in this study through the integrated *P*-*T*-H_2O model of Mollo et al. (2018) specifically designed to Etnean minerals and their host magmas (Supplementary Material 4). The model uncertainty is minimized by adjusting the *P*-*T*-H_2O estimates within the calibration errors of the barometer (±150 MPa), thermometer (±20 °C), and hygrometer (±0.45 wt.% H_2O), in order to reduce the difference (Δ) between measured and predicted equilibrium values of $Kd_{Fe\text{-}Mg}$ (Fe-Mg exchange partition coefficient; Putirka, 2008), K_{Na} (Na partition coefficient; Blundy et al., 1995), and *DiHd* (diopside + hedenbergite; Mollo et al., 2013). These correction criteria and probability density functions are applied to microphenocryst and bulk rock

compositions (Supplementary Material 4), providing the most reliable near-equilibrium conditions for clinopyroxene saturation at ~210-260 MPa (i.e., ~8-10 km, presuming a continental crust density of 2.6 g cm^{-3}; Armienti et al., 2013), ~1,070-1,080 °C, and ~2.2-2.4 wt.% H_2O (Fig. 9). Notably, the estimated pressure range matches with magma storage at an intermediate depth of 7-13 km (Murru et al., 1999) and within a major aseismic high P-wave velocity body extending down to 18 km (Aloisi et al., 2002).

Fig. 10 shows CSD curves of 2011-2012 clinopyroxene crystals, with kinked concave-up shapes and marked changes in slope, from a shallower gradient in the larger crystals to a steeper gradient in the smaller ones (Burney et al., 2020). Regression coefficients determined for microphenocrysts (m from -13.589 to -16.914 mm^{-1} and N_0 from 8.177 to 10.358 mm^{-4}) and microlites (m from -45.981 to -93.140 mm^{-1} and N_0 from 13.796 to 16.764 mm^{-4}) are characteristically different (Table 2). Coherently, the systematic kink of CSD curves attests the occurrence of distinct crystal size distributions for microphenocrysts ($L \geq 0.1$ mm) and microlites ($L < 0.1$ mm). In a few samples the kink shifts at 0.14 mm because of the higher crystallinity of the erupted products (Cashman and Marsh 1988; Higgins 1996). These kinked shape trends are generally attributed to variable crystal growth rates and undercooling histories of magmas during ascent along different portions of the plumbing system and volcanic conduit, without any gain or loss from/to external magma batches (Kirkpatrick, 1981, 1983; Maaloe et al., 1989; Armienti et al., 1994; Armienti, 2008). In this context, $N(L)$ vs. L trajectories displayed in Fig. 10 and their regression coefficients (Table 2) are principally the result of different crystallization regime upon the P-T-H_2O array experienced by dynamically erupted magmas (Armienti et al., 2013).

By applying Eq. (15) to the slope of each CSD curve, we have quantified the growth time recorded by the textual evolution of 2011-2012 clinopyroxene crystals. Results from calculations are listed in Table 2 and return values of t_{max} ranging from ~1.4±0.3 to ~33.4±8 min and from ~50.7±13 to ~136.2±35 h for microlite and microphenocryst populations, respectively. The low magnitude of t_{max} measured for microlites testifies to fast kinetic effects and rapid crystal growth regimes, when

magma acceleration within the uppermost part of the conduit leads to large ΔT (Armienti, 2008). According to this proposition, fluid mechanic mechanisms governing magma ascent indicate that, upon abundant volatile exsolution within a narrow degassing path, the volume expansion of magma by the growth of gas bubbles is balanced by an increasing acceleration towards the surface (Gonnermann and Manga, 2013). Conversely, the high magnitude of t_{max} derived for microphenocrysts indicates sluggish kinetic effects associated with small ΔT and slow crystal growth regimes from more relaxed melts. Evidently, at greater depths and within the plumbing system of Mt. Etna volcano, clinopyroxene microphenocrysts have more time to grow and equilibrate with the melt under steady-state conditions (Armienti et al., 2013).

We emphasize that values of t_{max} are intrinsically related to the kinetic aspects and thermodynamics of clinopyroxene growth. Therefore, caution should be exercised in comparing the magnitude of t_{max} with the time scale of magma dynamics derived by numerical modeling of volcanic conduit processes (e.g., La Spina et al., 2016, 2021; Polacci et al., 2019) and/or time scales from elemental diffusion (e.g., Giuffrida et al., 2018; Ubide and Kamber, 2018). The corollary is that the crystal growth will never occur when a full thermodynamic equilibrium (i.e., a minimum energy state) is achieved throughout the crystal-melt interface. There is an energy barrier to overcome in order to promote imbalance between the attachment and detachment energies of cations at the crystal-melt interface. This excess energy is attained by melt supersaturation, when the thermodynamic driving force is higher than a critical threshold above which crystal growth takes place (Sunagawa, 2005). At large ΔT, such as those typically occurring during rapid ascent of magma within a volcanic conduit, the effective mechanism controlling clinopyroxene growth rate depends on the slow diffusivity of Si and Al in the melt with respect to Ca and Mg. The addition of network-former species to the growing surface of crystals is the rate-controlling step for the textural maturation of clinopyroxene (Mollo and Hammer, 2017). Moreover, since the strength of the ^{T}Al–O bonds in the melt is weaker than that of ^{T}Si–O bonds (Kirkpatrick, 1983), the transfer rate of incompatible cations (i.e., Al + Ti) from the melt to the crystal surface is much more facilitated than that of compatible elements (i.e., Ca + Mg; Mollo

et al., 2010, 2012; Pontesilli et al., 2019; Masotta et al., 2020). According to these kinetic principles, G_{max} and t_{max} are inextricably interrelated to the morphological stability of the crystal-melt interface throughout the growth process (Sunagawa, 2005). The crystal-melt interface is the locus where growth or dissolution take place upon dynamic changes of P-T-H_2O during magma ascent towards the surface and upon decompression-cooling paths. Melt supersaturation causes morphological instability of the crystal and shifts from polyhedral to hopper to dendritic forms, by imposing temperature and concentration gradients at the interface (Sunagawa, 2005).

According to the above considerations, the magnitude of G_{max} and t_{max} mostly depends on 1) morphological instability as a function of attachment/detachment energies of cations with increasing ΔT and 2) concentration gradients in the melt next to the advancing crystal surface and disequilibrium uptake of incompatible cations within the lattice site (Pontesilli et al., 2019; Masotta et al., 2020). However, it is interesting to note that values of t_{max} (~1-41 min; Table 2) measured for 2011-2012 clinopyroxene microlites are consistent with the numerical analysis of magma ascent times of 1995–2019 eruptions at Mt. Etna (Polacci et al., 2019). The 1995–2019 explosive activity produced, among other products, significant ash emissions. The numerical analysis was performed by considering volcanic conduits with either cylindrical or dyke geometries, yielding ascent time minimum (~2.5 min) at the center of the conduit and maximum (~25 min) at the conduit walls, corresponding to ~1% of the total magma rising within the conduit (Polacci et al., 2019). Similarly, the estimated ascent time of magma within a dyke ranges from ~3.3 min to ~33 min, corresponding to less than 0.4% of the total magma (Polacci et al., 2019). According to La Spina et al. (2021), lava fountaining at Mt. Etna consists of an eruptive style distinct from effusive and explosive eruptions, as the result of rapid magma ascent with most of fragmentation above the vent rather than within the conduit. Magma ascent times of ~40 min determined by La Spina et al. (2021) are in the same order of magnitude of t_{max} calculated for some 2011-2012 microlites and microphenocrysts from this study.

A conceptual model of open conduit dynamics at Mt. Etna is schematized in Fig. 11. Most of the clinopyroxene microlite crystallization occurs within the uppermost segment of the volcanic

conduit under the effect of large ΔT and short t_{max} (Fig. 11). This short time is also comparable with that (< 60 min) estimated for plagioclase during dynamic ascent of magma and under strong disequilibrium conditions driven by abundant volatile exsolution (La Spina et al., 2016). *In-situ* experiments carried out on a typical Etnean trachybasalt reveal that ΔT = 60-140 °C drive exceptionally rapid crystallization of plagioclase and clinopyroxene microlites in several minutes, also inducing a step change in viscosity that may trigger magma fragmentation (Arzilli et al., 2019). Moreover, because of rapid fractionation of lithium between melt and fluid during magma degassing, the decrease in Li concentration in plagioclase by diffusion corresponds to magma ascent time scales variable from 0.2 to 3 min for paroxysmal sequences (Giuffrida et al., 2018). This syn-eruptive stage of magma is outlined by t_{max} of ~1-3 min calculated for 2011-2012 clinopyroxene microlites (Fig. 11), as well as by rapid decompression (12 MPa min^{-1}) and cooling experiments (12 °C min^{-1}) of Arzilli et al. (2019) showing that abundant clinopyroxene microlite crystallization occurs in only 5 min at ΔT > 100 °C. Considering that most of the disequilibrium crystallization takes place at ~1.5 km below the vent (cf. La Spina et al., 2016, 2021), we derive maximum magma ascent rates of ~1-23 m s^{-1} considering the model error (Table 2 and Fig. 11). These estimates are statistically comparable with syn-eruptive ascent rates of ~3 m s^{-1} determined for mild lava fountaining activity at Mt. Etna, Stromboli, and Kilauea (La Spina et al., 2016, 2021), as well as for syn-eruptive ascent rates measured for shallow subvolcanic magma storage zones (depth ≤10 km) feeding more silicic explosive eruptions worldwide (~0.5-50 m s^{-1}; Cassidy et al., 2018).

Notably, the compositional difference between the initial melt and the final three-dimensional structural arrangement of the crystal requires that stable nuclei can form only when the local configuration of molecular units attains a critical cluster radius (e.g., Vetere et al., 2015 and references therein). As the microlite crystallization increases during ascent of magma within the conduit, the residual melt composition becomes progressively more differentiated (i.e., SiO_2-Na_2O-rich and CaO-MgO-poor) favoring the enlargement of plagioclase stability field (i.e., albite end-member) at the expense of clinopyroxene (i.e., diopside end-member). For this reason, at ΔT > 100 °C, the growth

kinetics of 2011-2012 clinopyroxene microlites does not return magma ascent rates > 23 m s^{-1} (Fig. 11), such as those also measured at Mt. Etna that are related to strong degassing processes governing Li diffusion in plagioclase (~43 m s^{-1}; Giuffrida et al., 2018) and further magma acceleration at the vent (~75 m s^{-1}; La Spina et al., 2021).

Differently from shallow conduit and vent dynamics, values of t_{max} (~38-171 h; Table 2) calculated for 2011-2012 clinopyroxene microphenocrysts are orders of magnitude greater than the very fast crystallization history recorded by microlites. Evidently, the growth of microphenocrysts does not represent the timing of eruption within the upper conduit or immediately before ejection from the vent, where large degrees of supersaturation are driven by fast cooling, decompression, and degassing of magma (Fig. 11). Rather, most of microphenocryst growth is governed by a small ΔT and long t_{max} at depth (Fig. 11), where crystallization kinetics are slow and the crystal surface has enough time to develop polyhedral morphology (Armienti et al., 2013). Moreover, there is no systematic change of t_{max} with the 1) 2011-2012 paroxysmal phase duration, 2) Strombolian activity preceding lava fountaining, and 3) associated seismic signals or volcanic tremors (data from the multidisciplinary reports of the INGV Osservatorio Etneo available at www.ct.ingv.it). This suggests that the onset of microphenocryst growth takes place at the early saturation condition of clinopyroxene and under a near-equilibrium crystallization state corresponding to the main storage region of magma at ~8-10 km of depth. It is also not excluded that microphenocryst crystallization continues via open system processes governed by the invasion of the plumbing system with fresh magma (Fig. 11). Time scales from this study closely match with those (~17-168 h) derived by Ubide and Kamber (2018) for the development of Cr zoning in clinopyroxene caused by continuous magma recharge and mixing events at depth of ~10 km (Fig. 11). Under such conditions, both volatile exsolution and crystallization are low, bubble expansion and magma buoyancy are limited, and the slow upward migration of magma provides more time for mineral-melt-fluid equilibration (e.g., Cassidy et al., 2018). Ubide and Kamber (2018) estimated magma ascent rates of 0.02-0.17 m s^{-1} that are analogous to those (0.02-0.07 m s^{-1}; Table 2) determined for the growth of 2011-2012

clinopyroxene microphenocrysts. Therefore, differently from the fast acceleration of magma within the conduit, open system dynamics at depth require longer time periods for the migration of magma through interconnected storage regions (Fig. 11). This conclusion is supported by similar estimates obtained through different methodologies based on cation redistributions in minerals (0.01-0.31 m s^{-1}; Mollo et al., 2015b) and geophysical signals (0.04-0.4 m s^{-1}; Aloisi et al., 2006) at Mt. Etna volcano, as well as by authors investigating other volcanic settings worldwide, such as Hawaii (0.01–0.04 m s^{-1}; Rutherford, 2008; Gonnermann and Manga, 2013), Unzen (0.01–0.07 m s^{-1}; Toramaru et al., 2008) and Mount St. Helens (0.01–0.15 m s^{-1}; Rutherford and Hill, 1993).

5. Conclusions

Clinopyroxene growth kinetics have been experimentally investigated and parameterized under a broad range of isothermal-isobaric, decompression, and cooling rate conditions, representative of variable crystallization conditions at Mt. Etna volcano. Through this approach, the following main conclusions can be drawn:

1) the texture of clinopyroxene is greatly controlled by melt supersaturation (i.e., undercooling) and relaxation time resulting from *P*-*T*-H_2O changes;
2) crystal euhedrality is maintained either under substantially subliquidus isothermal-isobaric or slow-to-fast decompression conditions, with the main difference represented by the development of sector-zoned clinopyroxene crystals during melt decompression;
3) as the relaxation time increases, the crystal growth rate radically decreases, whereas the crystal euhedrality increases;
4) thermodynamic modeling suggests that the transition between interface-controlled and diffusion-controlled growth arises at undercooling higher than 30 °C;
5) below this threshold value, sluggish crystallization kinetics lead to the formation of sector-zoned clinopyroxene crystals, with Di-Hd-rich, CaTs-CaTiTs-poor hourglass sectors {- 1 1

1} and Di-Hd-poor, CaTs-CaTiTs-rich prism sectors {1 0 0} typically observed at Mt. Etna volcano;

6) by integrating experimental textural data and the algebraic expression of crystal size distribution (CSD), the crystallization time of clinopyroxene can be parameterized as a function of growth rate;
7) for the case of 2011-2012 lava fountains, results from calculations return time scales variable from ~10^0-10^1 min and ~10^1-10^2 h for microlite and microphenocryst populations, respectively;
8) while shorter time scales of microlites testify to fast kinetic effects due to large undercoolings during magma acceleration in the uppermost part of the volcanic conduit, longer time scales of microphenocrysts are associated with near-equilibrium crystallization due to small undercoolings at depth;
9) we conclude that fast ascent rates of magmas (~10^0-10^1 m s^{-1}) lead to disequilibrium growth of microlites and supersaturation (i.e., undercooling) effects due to strong degassing and cooling before eruption from the vent. In contrast, slow ascent rates of magmas (~10^{-2} m s^{-1}) favor near-equilibrium crystallization of microphenocrysts over longer time periods and within the interconnected storage regions that characterize the plumbing system architecture of Mt. Etna volcano.

Acknowledgments

The authors would like to thank Alessandro Vona and Alessio Pontesilli for their kind help with crystal size distribution (CSD) analysis. This work has been greatly improved by the helpful and thoughtful reviews of Fabio Arzilli and Emily First. Michael Roden is also acknowledged for his valuable editorial guidance.

References

Aloisi, M., Cocina, O., Neri, G., Orecchio, B., Privitera, E., 2002. Seismic tomography of the crust underneath the Etna volcano, Sicily. Phys. Earth Planet. Inter. 134, 139–155.

Aloisi, M., Bonaccorso, A., Gambino, S., 2006. Imaging composite dike propagation (Etna, 2002 case). J. Geophys. Res. 111.

Andronico, D., Branca, S., Calvari, S., Burton, M., Caltabiano, T., Corsaro, R.A., Del Carlo, P., Garfì, G., Lodato, L., Miraglia, L., Murè, F., Neri, M., Pecora, E., Pompilio, M., Salerno, G., Spampinato, L., 2005. A multi-disciplinary study of the 2002-03 Etna eruption: insights into a complex plumbing system. Bull Volcanol 67, 314–330.

Armienti, P., Pareschi, M.T., Innocenti, F., Pompilio, M., 1994. Effects of magma storage and ascent on the kinetics of crystal growth. Contr. Mineral. and Petrol. 115, 402–414.

Armienti, P., Francalanci, L., Landi, P., 2007. Textural effects of steady state behaviour of the Stromboli feeding system. J. Volcanol. Geotherm. Res. 160, 86–98.

Armienti, P., 2008. Decryption of Igneous Rock Textures: Crystal Size Distribution Tools. Rev Mineral Geochem 69, 623–649.

Armienti, P., Perinelli, C., Putirka, K.D., 2013. A New Model to Estimate Deep-level Magma Ascent Rates, with Applications to Mt. Etna (Sicily, Italy). J. Petrol. 54, 795–813.

Arzilli, F., Fabbrizio, A., Schmidt, M.W., Petrelli, M., Maimaiti, M., Dingwell, D.B., Paris, E., Burton, M., Carroll, M.R., 2018. The effect of diffusive re-equilibration time on trace element partitioning between alkali feldspar and trachytic melts. Chem. Geol. 495, 50–66.

Arzilli, F., La Spina, G., Burton, M.R., Polacci, M., Le Gall, N., Hartley, M.E., Di Genova, D., Cai, B., Vo, N.T., Bamber, E.C., Nonni, S., Atwood, R., Llewellin, E.W., Brooker, R.A., Mader, H.M., Lee, P.D., 2019. Magma fragmentation in highly explosive basaltic eruptions induced by rapid crystallization. Nat. Geosci. 12, 1023–1028.

Baker, D.R., 2008. The fidelity of melt inclusions as records of melt composition. Contrib Mineral Petrol 156, 377–395.

Blundy, J.D., Falloon, T.J., Wood, B.J., Dalton, J.A., 1995. Sodium partitioning between clinopyroxene and silicate melts. J. Geophys. Res. Solid Earth 100, 15501–15515.

Bonechi, B., Perinelli, C., Gaeta, M. Clinopyroxene growth rates at high pressure: constraints on magma recharge of the deep reservoir of the Campi Flegrei Volcanic District (south Italy). Bull Volcanol 82, 5.

Botcharnikov, R.E., Almeev, R.R., Koepke, J., Holtz, F., 2008. Phase Relations and Liquid Lines of Descent in Hydrous Ferrobasalt--Implications for the Skaergaard Intrusion and Columbia River Flood Basalts. J. Petrol. 49, 1687–1727.

Burkhard, D.J.M., 2005. Nucleation and growth rates of pyroxene, plagioclase, and Fe-Ti oxides in basalt under atmospheric conditions. European Journal of Mineralogy 17, 675–686.

Burney, D., Peate, D.W., Riishuus, M.S., Ukstins, I.A., 2020. Reconstructing the plumbing system of an off-rift primitive alkaline tuya (Vatnafell, Iceland) using geothermobarometry and CSDs. J. Volcanol. Geotherm. Res. 399, 106914.

Cashman, K.V., Marsh, B.D., 1988. Crystal size distribution (CSD) in rocks and the kinetics and dynamics of crystallization II: Makaopuhi lava lake. Contr. Mineral. and Petrol. 99, 292–305.

Cashman, K.V., 1990. Textural constraints on the kinetics of crystallization of igneous rocks. Rev. Mineral. 24, 259–314.

Cassidy, M., Manga, M., Cashman, K., Bachmann, O., 2018. Controls on explosive-effusive volcanic eruption styles. Nat Commun 9.

Corsaro, R.A., Civetta, L., Di Renzo, V., Miraglia, L., 2009. Petrology of lavas from the 2004-2005 flank eruption of Mt. Etna, Italy: inferences on the dynamics of magma in the shallow plumbing system. Bull. Volcanol. 71, 781–793.

Di Stefano, F., Mollo, S., Ubide, T., Petrone, C.M., Caulfield, J., Scarlato, P., Nazzari, M., Andronico, D., Del Bello, E., 2020. Mush cannibalism and disruption recorded by clinopyroxene phenocrysts at Stromboli volcano: New insights from recent 2003–2017 activity. Lithos 360–361, 105440.

Dowty, E., 1976. Crystal structure and crystal growth: II. Sector zoning in minerals. Am. Mineral. 61, 460–469.

Duan, X., 2014. A general model for predicting the solubility behavior of H2O-CO2 fluids in silicate melts over a wide range of pressure, temperature and compositions. Geochim. Cosmochim. Acta 125, 582–609. http://dx.doi.org/10.1016/j.gca.2013.10.018.

Ferlito, C., Coltorti, M., Cristofolini, R., Giacomoni, P.P., 2009. The contemporaneous emission of low-K and high-K trachybasalts and the role of the NE Rift during the 2002 eruptive event, Mt. Etna, Italy. Bull Volcanol 71, 575–587.

Ferlito, C., Viccaro, M., Nicotra, E., Cristofolini, R., 2012. Regimes of magma recharge and their control on the eruptive behaviour during the period 2001–2005 at Mt. Etna volcano. Bull Volcanol 74, 533–543.

First E.C., Hammer J.E., 2016. Igneous cooling history of olivine-phyric shergottite Yamato 980459 constrained by dynamic crystallization experiments. Meteorit Planet Sci. 51, 1233–1255.

First, E.C., Leonhardi, T.C., Hammer, J.E., 2020. Effects of superheating magnitude on olivine growth. Contrib Mineral Petrol 175, 13.

Giacomoni, P.P., Coltorti, M., Mollo, S., Ferlito, C., Braiato, M., Scarlato, P., 2018. The 2011–2012 paroxysmal eruptions at Mt. Etna volcano: Insights on the vertically zoned plumbing system. J. Volcanol. Geotherm. Res. 349, 370–391.

Giordano, D., Nichols, A.R.L., Dingwell, D.B., 2005. Glass transition temperatures of natural hydrous melts: a relationship with shear viscosity and implications for the welding process. J. Volcanol. Geotherm. Res. 142, 105–118.

Giuffrida, M., Viccaro, M., 2017. Three years (2011–2013) of eruptive activity at Mt. Etna: Working modes and timescales of the modern volcano plumbing system from micro-analytical studies of crystals. Earth Sci Rev 171, 289–322.

Giuffrida, M., Viccaro, M., Ottolini, L., 2018. Ultrafast syn-eruptive degassing and ascent trigger high-energy basic eruptions. Sci Rep 8.

Giuliani, L., Iezzi, G., Vetere, F., Behrens, H., Mollo, S., Cauti, F., Ventura, G., Scarlato, P., 2020. Evolution of textures, crystal size distributions and growth rates of plagioclase, clinopyroxene and spinel crystallized at variable cooling rates from a mid-ocean ridge basaltic melt. Earth Sci Rev 204, 103165.

Gonnermann, H.M., Manga, M., 2013. Dynamics of magma ascent in the volcanic conduit. In: Fagents, S.A., Gregg, T.K.P., Lopes, R.M.C. (Eds.), Modeling Volcanic Processes. Cambridge Univ Press, pp.55–84.

Gualda, G.A., Ghiorso, M.S., Lemons, R.V., Carley, T. L., 2012. Rhyolite-MELTS: a modified calibration of MELTS optimized for silica-rich, fluid-bearing magmatic systems. J. Petrol. 53, 875–890.

Hammer, J.E., 2006. Influence of fO2 and cooling rate on the kinetics and energetics of Fe-rich basalt crystallization. Earth Planet. Sci. Lett. 248, 618–637.

Hammer, J.E., 2008. Experimental Studies of the Kinetics and Energetics of Magma Crystallization. Rev Mineral Geochem 69, 9–59.

Hammer, J., Jacob, S., Welsch, B., Hellebrand, E., Sinton, J., 2016. Clinopyroxene in postshield Haleakala ankaramite: 1. Efficacy of thermobarometry. Contrib Mineral Petrol 171.

Hair Jr., J.F., Anderson, R.E., Tatham, R.L., Black, W.C., 1995. Multivariate Data Analysis. 3rd ed. Macmillan, New York (742 pp.).

Higgins, M.D., 1996. Magma dynamics beneath Kameni volcano, Thera, Greece, as revealed by crystal size and shape measurements. J. Volcanol. Geotherm. Res. 70, 37–48.

Higgins, M.D., 2000. Measurement of crystal size distributions. Am. Mineral. 85, 1105–1116.

Iezzi, G., Mollo, S., Shaini, E., Cavallo, A., Scarlato, P., 2014. The cooling kinetics of plagioclase revealed by electron microprobe mapping. Am. Mineral. 99, 898–907.

Ishibashi, H., 2013. Spinel–melt oxygen barometry: a method and application to Cenozoic alkali basaltic magmas from the Higashi–Matsuura district, NW Kyushu, Japan. Geosci. Repts. 40, 21–32.

Karamanov, A., Pisciella, P., Pelino, M., 2000a. The crystallisation kinetics of iron rich glass in different

atmospheres. J. Eur. Ceram. Soc. 20, 2233–2237.

Kirkpatrick, R.J., 1981. Kinetics of crystallization of igneous rocks. In: Lasaga, A.C., Kirkpatrick, R.J. (Eds.), Reviews in Mineralogy 8. pp. 321–395.

Kirkpatrick, R.J., 1983. Theory of nucleation in silicate melts. Am. Mineral. 68, 66–77.

Kostov, I., Kostov, R.I., 1999. Crystal Habits of Minerals. Bulgarian Academic Monographs, Sophia.

Kouchi, A., Sugawara, Y., Kashima, K., Sunagawa, I., 1983. Laboratory growth of sector zoned clinopyroxenes in the system CaMgSi2O6-CaTiAl2O6. Contrib. Mineral. Petrol. 83, 177–184.

Lanzafame, G., Mollo, S., Iezzi, G., Ferlito, C., Ventura, G., 2013. Unraveling the solidification path of a pahoehoe "cicirara" lava from Mount Etna volcano. Bull Volcanol 75.

La Spina, G., Burton, M., de' Michieli Vitturi, M., Arzilli, F., 2016. Role of syn-eruptive plagioclase disequilibrium crystallization in basaltic magma ascent dynamics. Nat Commun 7.

La Spina, G., Arzilli, F., Llewellin, E.W., Burton, M.R., Clarke, A.B., de' Michieli Vitturi, M., Polacci, M., Hartley, M.E., Di Genova, D., Mader, H.M., 2021. Explosivity of basaltic lava fountains is controlled by magma rheology, ascent rate and outgassing. Earth Planet. Sci. Lett. 553, 116658.

Lasaga, A.C., 1998. Kinetic Theory in the Earth Sciences. Princeton University Press, Princeton, New York.

Lofgren, G.E., 1974. An experimental study of plagioclase morphology: isothermal crystallization. Am. J. Sci. 264, 243–273.

Maaløe, S., Tumyr, O., James, D., 1989. Population density and zoning of olivine phenocrysts in tholeiites from Kauai, Hawaii. Contr. Mineral. and Petrol. 101, 176–186.

Marsh, B.D., 1988. Crystal size distribution (CSD) in rocks and the kinetics and dynamics of crystallization. Contr. Mineral. and Petrol. 99, 277–291.

Masotta, M., Pontesilli, A., Mollo, S., Armienti, P., Ubide, T., Nazzari, M., Scarlato, P., 2020. The role of undercooling during clinopyroxene growth in trachybasaltic magmas: Insights on magma decompression and cooling at Mt. Etna volcano. Geochim. Cosmochim. Acta 268, 258–276.

Mollo, S., Del Gaudio, P., Ventura, G., Iezzi, G., Scarlato, P., 2010. Dependence of clinopyroxene composition on cooling rate in basaltic magmas: implications for thermobarometry. Lithos 118, 302–312.

Mollo, S., Misiti, V., Scarlato, P., Soligo, M., 2012. The role of cooling rate in the origin of high temperature phases at the chilled margin of magmatic intrusions. Chem. Geol. 322–323, 28–46.

Mollo, S., Blundy, J.D., Iezzi, G., Scarlato, P., Langone, A., 2013. The partitioning of trace elements between clinopyroxene and trachybasaltic melt during rapid cooling and crystal growth. Contrib Mineral Petrol 166, 1633–1654.

Mollo, S., Masotta, M., 2014. Optimizing pre-eruptive temperature estimates in thermally and chemically zoned magma chambers. Chem. Geol. 368, 97–103.

Mollo, S., Giacomoni, P.P., Andronico, D., Scarlato, P., 2015a. Clinopyroxene and titanomagnetite cation redistributions at Mt. Etna volcano (Sicily, Italy): footprints of the final solidification history of lava fountains and lava flows. Chem. Geol. 406, 45–54.

Mollo, S., Giacomoni, P.P., Coltorti, M., Ferlito, C., Iezzi, G., Scarlato, P., 2015b. Reconstruction of magmatic variables governing recent Etnean eruptions: constraints from mineral chemistry and P–T–fO2–H2O conditions. Lithos 212–215, 311–320.

Mollo, S., Hammer, J.E., 2017. Dynamic crystallization in magmas. In: EMU Notes in Mineralogy. 16. pp. 373–418.

Mollo, S., Blundy, J., Scarlato, P., De Cristofaro, S.P., Tecchiato, V., Di Stefano, F., Vetere, F., Holtz, F., Bachmann, O., 2018. An integrated P-T-H2O-lattice strain model to quantify the role of clinopyroxene fractionation on REE+Y and HFSE patterns of mafic alkaline magmas: Application to eruptions at Mt. Etna. Earth Sci Rev 185, 32–56.

Morgan, D.J., Jerram, D.A., 2006. On estimating crystal shape for crystal size distribution analysis. J. Volcanol. Geotherm. Res. 154, 1–7.

Murru, M., Montuori, C., Wyss, M., Privitera, E., 1999. The locations of magma chambers at Mt. Etna, Italy, mapped by b-values. Geophys. Res. Lett. 26, 2553–2556.

Nascimento, M.L.F., Ferreira, E.B., Zanotto, E.D., 2004. Kinetics and mechanisms of crystal growth and diffusion in a glass-forming liquid. J. Chem. Phys. 121, 8924–8928.

Orlando, A., D'Orazio, M., Armienti, P., Borrini, D., 2008. Experimental determination of plagioclase and clinopyroxene crystal growth rates in an anhydrous trachybasalt from Mt Etna (Italy). European Journal of Mineralogy 20, 653–664.

Patanè, D., De Gori, P., Chiarabba, C., Bonaccorso, A., 2003. Magma Ascent and the Pressurization of Mount Etna's Volcanic System. Science 299, 2061–2063.

Perinelli, C., Mollo, S., Gaeta, M., De Cristofaro, S.P., Palladino, D.M., Armienti, P., Scarlato, P., Putirka, K.D., 2016. An improved clinopyroxene-based hygrometer for Etnean magmas and implications for eruption triggering mechanisms. Am. Mineral. 101, 2774–2777.

Perinelli, C., Mollo, S., Gaeta, M., De Cristofaro, S.P., Palladino, D.M., Scarlato, P., 2018. Impulsive supply of volatile-rich magmas in the shallow plumbing system of Mt. Etna Volcano. Minerals 8, 482.

Petrone, C.M., Bugatti, G., Braschi, E., Tommasini, S., 2016. Pre-eruptive magmatic processes re-timed using a non-isothermal approach to magma chamber dynamics. Nat Commun 7.

Petrone, C.M., Braschi, E., Francalanci, L., Casalini, M., Tommasini, S., 2018. Rapid mixing and short storage timescale in the magma dynamics of a steady-state volcano. Earth Planet. Sci. Lett. 492, 206–221.

Polacci, M., Arzilli, F., La Spina, G., Le Gall, N., Cai, B., Hartley, M.E., Di Genova, D., Vo, N.T., Nonni, S., Atwood, R.C., Llewellin, E.W., Lee, P.D., Burton, M.R., 2018. Crystallisation in basaltic magmas revealed via in situ 4D synchrotron X-ray microtomography. Sci Rep 8, 8377–8383.

Polacci, M., Andronico, D., de' Michieli Vitturi, M., Taddeucci, J., Cristaldi, A., 2019. Mechanisms of Ash Generation at Basaltic Volcanoes: The Case of Mount Etna, Italy. Front. Earth Sci. 7.

Pontesilli, A., Masotta, M., Nazzari, M., Mollo, S., Armienti, P., Scarlato, P., Brenna, M., 2019. Crystallization kinetics of clinopyroxene and titanomagnetite growing from a trachybasaltic melt: New insights from isothermal time-series experiments. Chem. Geol. 510, 113–129.

Putirka, K., 2008. Thermometers and barometers for volcanic systems. Rev. Mineral. Geochem. 69, 61–120. http://dx.doi.org/10.2138/rmg.2008.69.3.

Ratkowsky, D.A., 1990. Handbook of Non-linear Regression Models. Marcel Decker Inc., New York.

Rutherford, M.J., Hill, P.M., 1993. Magma ascent rates from amphibole breakdown: An experimental study applied to the 1980-1986 Mount St. Helens eruptions. J. Geophys. Res. 98, 19667–19685.

Rutherford, M.J., 2008. Magma Ascent Rates. Rev Mineral Geochem 69, 241–271.

Schanofski, M., Fanara, S., Schmidt, B.C., 2019. CO2–H2O solubility in K-rich phonolitic and leucititic melts. Contrib Mineral Petrol 174.

Shea, T., and Hammer, J.E., 2013. Kinetics of cooling- and decompression-induced crystallization in hydrous mafic-intermediate magmas. J. Volcanol. Geotherm. Res., 260, 127–145.

Simakin, A.G., Salova T.P., Armienti P., 2003. Kinetics of clinopyroxene growth from a hydrous hawaiite melt. Geochemistry Int. 41, 1275-1286.

Sunagawa, I., 1981. Characteristics of crystal growth in nature as seen from the morphology of mineral crystals. Bull. Mineral. 104, 81–87.

Sunagawa, I., 2005. Crystals: Growth, Morphology and Perfection. Cambridge University Press, Cambridge.

Toramaru, A., 1991. Model of nucleation and growth of crystals in cooling magmas. Contr. Mineral. and Petrol. 108, 106–117.

Toramaru, A., Noguchi, S., Oyoshihara, S., Tsune, A., 2008. MND(microlite number density) water exsolution rate meter. J. Volcanol. Geotherm. Res. 175, 156–167.

Ubide, T., Kamber, B.S., 2018. Volcanic crystals as time capsules of eruption history. Nat Commun 9.

Ubide, T., Mollo, S., Zhao, J., Nazzari, M., Scarlato, P., 2019a. Sector-zoned clinopyroxene as a recorder of magma history, eruption triggers, and ascent rates. Geochim. Cosmochim. Acta 251, 265–283.

Ubide, T., Caulfield, J., Brandt, C., Bussweiler, Y., Mollo, S., Di Stefano, F., Nazzari, M., Scarlato, P., 2019b. Deep Magma Storage Revealed by Multi-Method Elemental Mapping of Clinopyroxene Megacrysts at Stromboli Volcano. Front. Earth Sci. 7.

Vetere, F., Iezzi, G., Behrens, H., Holtz, F., Ventura, G., Misiti, V., Cavallo, A., Mollo, S., Dietrich, M., 2015. Glass forming ability and crystallization behavior of sub-alkaline silicate melts. Earth Sci Rev 150, 25–44.

Vetere, F., Iezzi, G., Behrens, H., Cavallo, A., Misiti, V., Dietrich, M., Knipping, J., Ventura, G., Mollo, S., 2013. Intrinsic solidification behaviour of basaltic to rhyolitic melts: a cooling rate experimental study. Chem. Geol. 354, 233–242.

Webb, S.L., Dingwell, D.B., 1995. Viscoelasticity. Rev. Mineral. Geochem. 32, 95–119.

Weill, D.E., Hon, R., Navrotsky, A., 1980. The igneous system CaMgSi2O6-CaAlaSi2O6-NaAlSi3O6: variations on a classic theme by Bowen. In: Hargraves RB (ed) Physics of magmatic processes. Princeton University Press, Princeton, pp 49-92.

Welsch, B., Hammer, J., Baronnet, A., Jacob, S., Hellebrand, E., Sinton, J., 2016. Clinopyroxene in postshield Haleakala ankaramite: 2. Texture, compositional zoning and supersaturation in the magma. Contrib. Mineral. Petrol. 171, 6.

Yilmaz, S., Özkan, O.T., Günay, V., 1996. Crystallization kinetics of basalt glass. Ceram. Int. 22, 477–481.

Zhang, Y., Ni, H., Chen, Y., 2010. Diffusion data in silicate melts. Rev. Mineral. Geochem. 72, 311–408.

Figure captions

Figure 1. Example of BSE (back-scattered electron) photomicrographs processed via NIH ImageJ software and reduced to binary type images (i.e., black vs. white color) by grey level thresholding (i.e., image segmentation; Armienti, 2008). A Matlab© code is also reported in Supplementary Material 1 to perform image processing operations in conjunction with NIH ImageJ. The retrieved textural parameters are 1) the equal-area best-fit ellipses and lengths of major (L) and minor (W) axes, 2) the surface area per unit volume, and 3) the area fraction of a given population within a plane that is comparable to its volume fraction. Bright BSE intensity phases refer to titanomagnetite crystals.

Figure 2. Selected BSE (back-scattered electron) photomicrographs representative of run products from *Experimental Set ISO*, *Experimental Set ΔP*, and *Experimental Set CR*. Bright BSE intensity phases refer to titanomagnetite crystals.

Figure 3. Variation of clinopyroxene content (% area) as a function of experimental conditions. Data refer to *Experimental Set ISO* and *Experimental Set ΔP* (a), and *Experimental Set CR* (b). Error bars refer to the uncertainties reported in Table 1.

Figure 4. Variation of 3D aspect ratio (S_V^P) as a function of experimental conditions. Data refer to *Experimental Set ISO* and *Experimental Set ΔP* (a), and *Experimental Set CR* (b). Error bars refer to the uncertainties reported in Table 1.

Figure 5. Total alkali *versus* silica (a) and Di + Hd *versus* CaTs + CaTiTs (b) diagrams showing experimental glass and clinopyroxene compositions, respectively. Natural compositions from eruptions at Mt. Etna volcano are also displayed for comparison.

Figure 6. Variation of $\ln G_{max}$ as a function of experimental conditions. Data refer to *Experimental Set ISO* and *Experimental Set ΔP* (a), and *Experimental Set CR* (b). Values of G_{max} modeled through the

thermodynamic expression of crystal growth (cf. Armienti, 2008) are also displayed for comparison. According to Eq. (6) reported in the text, thermodynamic data can be calculated for $\Delta T \geq 0$. Error bars refer to the uncertainties reported in Table 1.

Figure 7. Thermodynamic modeling of crystal growth kinetics for the transition between interface-controlled and diffusion-controlled growth regimes arising at undercooling higher than 30 °C. Modeled trends are depicted in green and blue for temperatures of 1,050 and 1,100 °C, respectively. In order to isolate the effect of ΔT, modeled trends are also compared with values of G_{max} (green and blue diamonds for 1,050 and 1,100 °C, respectively) from decompression and cooling rate experiments conducted over similar relaxation times (i.e., in the order of minutes for *ΔPf-1100-2H2O, ΔPf-1100-5H2O, ΔPf-1100-H2O+CO2, ΔPf-1050-2H2O, ΔPf-1050-5H2O, ΔPf-1050-H2O+CO2, CR-1050-0.25*, *CR-1050-0.5*).

Figure 8. Regression plot of maximum growth rate (G_{max}) *versus* experimental time (t) on a logarithmic scale (a). Data from this study are compared with those from previous experimental works investigating basaltic and trachybasaltic compositions that virtually reproduce the overall intrinsic variability of Monte Maletto Formation. Experiments were performed at conditions comparable with those of magmas erupted at Mt. Etna volcano (i.e., P = 0.1-1,000 MPa, T = 1,050-1,150 °C, H_2O = 0-4 wt.%, fO_2 = NNO+1.5-NNO+2, ΔT = 75-233 °C, and CR = 0.001-100 °C s^{-1}; Baker, 2008; Mollo et al., 2013; Pontesilli et al., 2019; Masotta et al., 2020). Probability density functions of regression coefficients β_0 (b) and β_1 (c) obtained from Monte Carlo simulations, as well model uncertainty associated with the estimate of t_{max} (d) are also displayed.

Figure 9. Saturation conditions calculated for clinopyroxene crystals from 2011-2012 lava fountains erupted at Mt. Etna volcano. Uncorrected equilibrium between microphenocryst and bulk rock

compositions has been determined for values of $Kd_{Fe\text{-}Mg}$ (Fe-Mg exchange partition coefficient; Putirka, 2008), K_{Na} (Na partition coefficient; Blundy et al., 1995), and *DiHd* (diopside + hedenbergite; Mollo et al., 2013). The equilibrium state of the bulk system has been corrected by minimizing the difference (Δ) between measured and predicted values. Using the model of Mollo et al. (2018), *P*-*T*-H_2O estimates have been adjusted within the calibration errors of the barometer (±150 MPa), thermometer (±20 °C), and hygrometer (±0.45 wt.% H_2O), in order to minimize the overall uncertainty.

Figure 10. Crystal size distribution (CSD) analysis of clinopyroxene crystals from 2011-2012 lava fountains erupted at Mt. Etna volcano. *N(L) versus L* curves attest the occurrence of two distinct microphenocryst and microlite populations.

Figure 11. Conceptual model of magma dynamics at Mt. Etna volcano describing the different time scales estimated for microlite and microphenocryst crystallization. Magma ascent velocities are also modeled accounting for either slow magma ascent rates within the interconnected storage regions forming the plumbing system architecture at depth or fast magma ascent rates within the uppermost part of the volcanic conduit and before eruption at the vent.

Figures

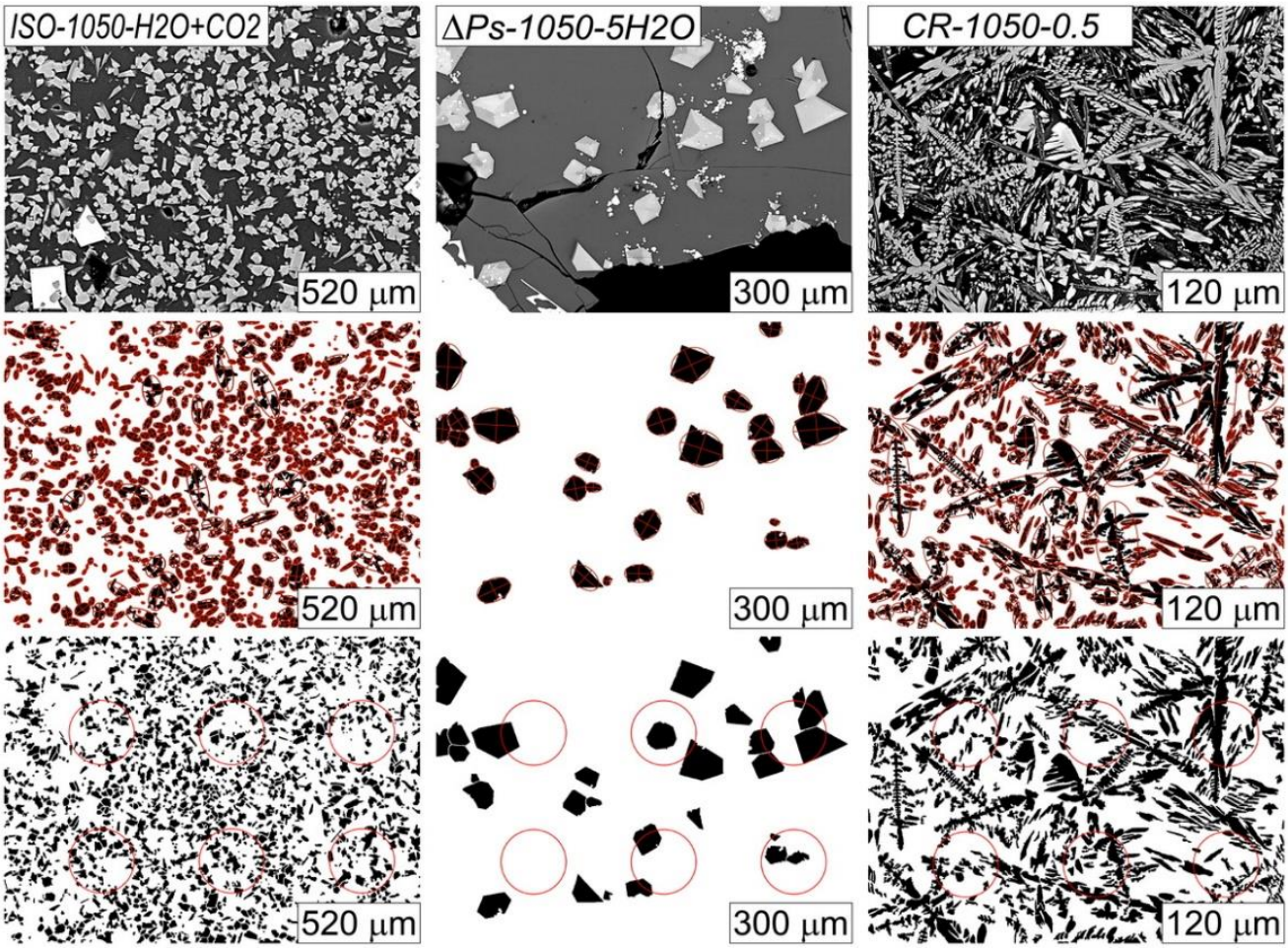

Figure 1

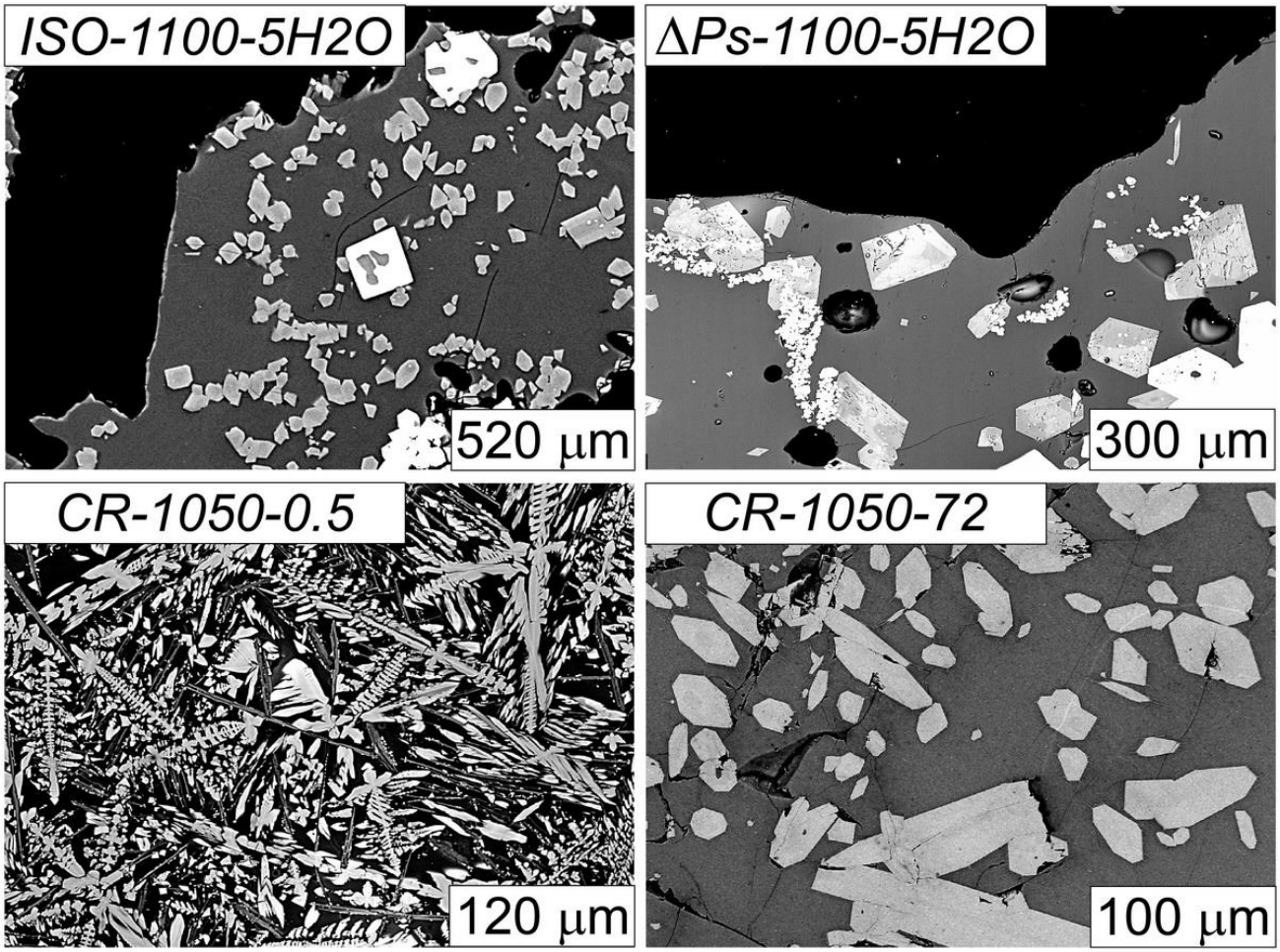
ISO-1100-5H2O
520 μm
ΔPs-1100-5H2O
300 μm
CR-1050-0.5
120 μm
CR-1050-72
100 μm

Figure 2

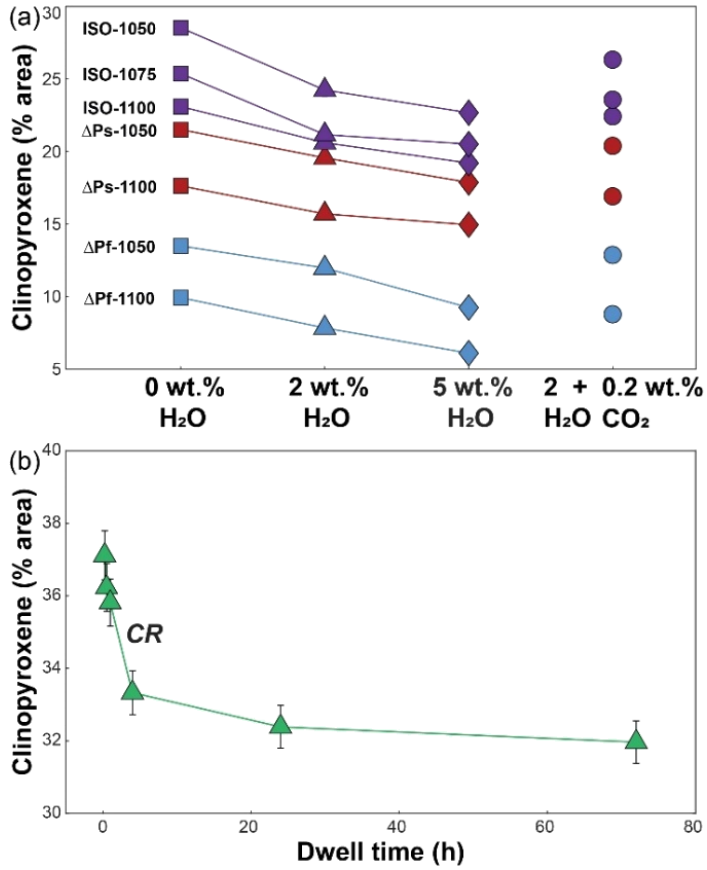

Figure 3

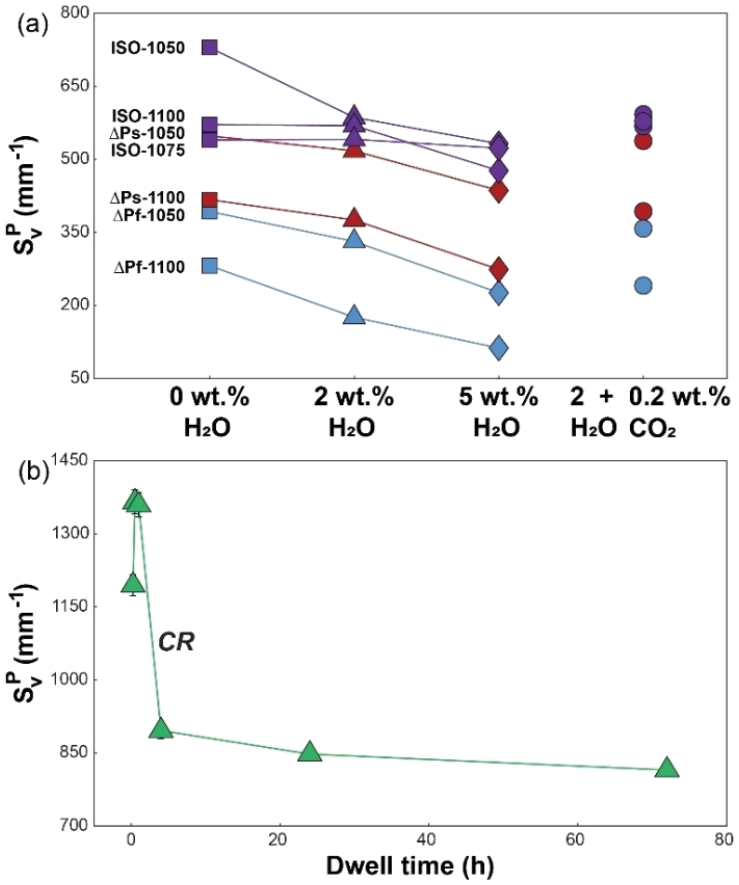

Figure 4

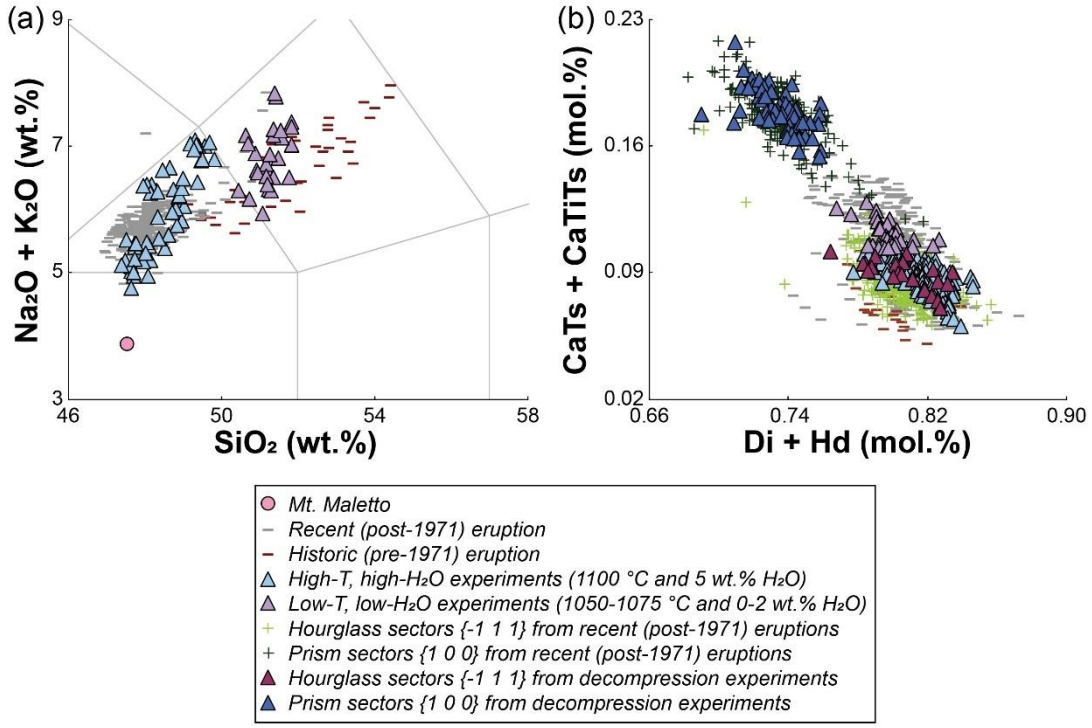

Figure 5

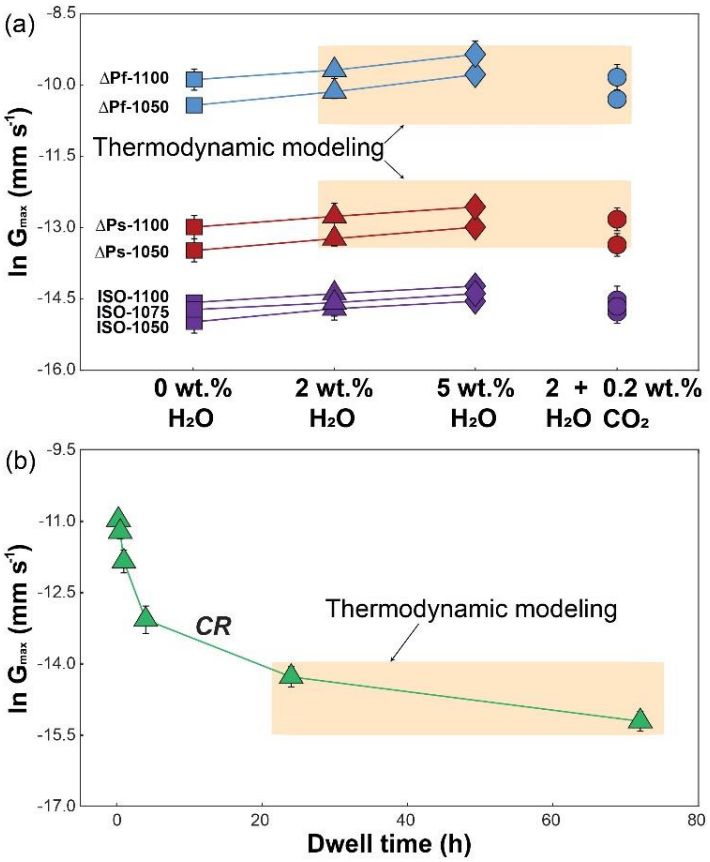

Figure 6

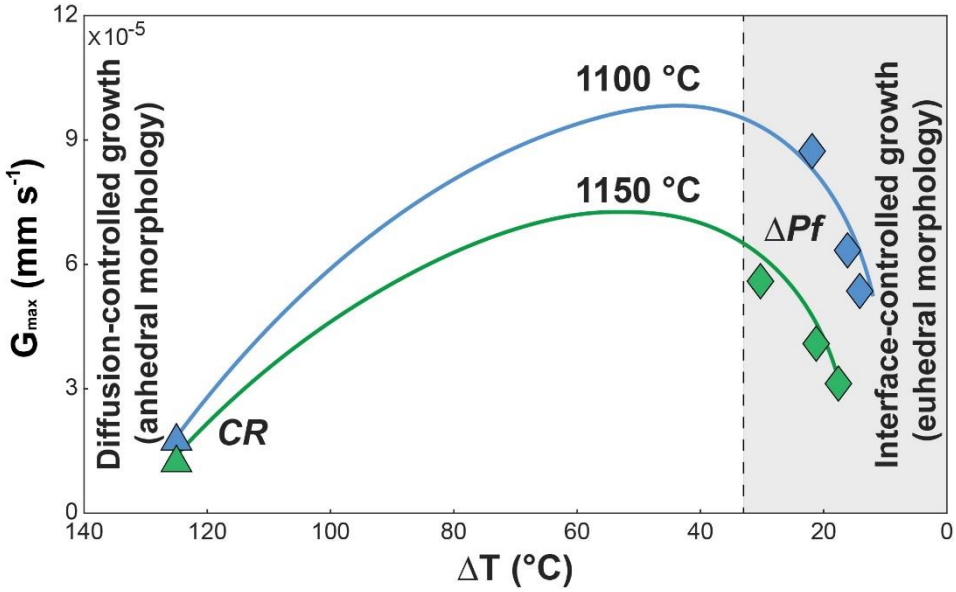

Figure 7

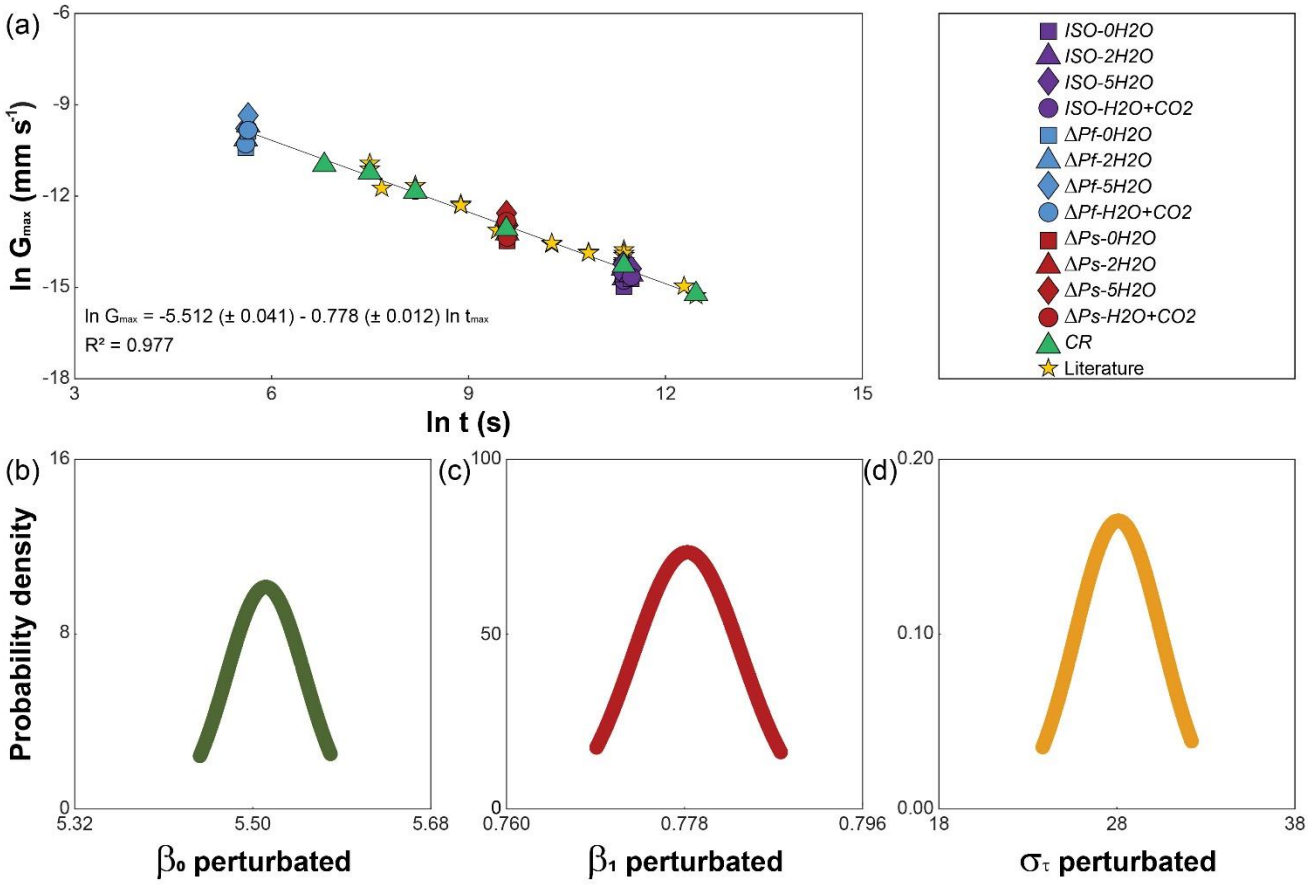

Figure 8

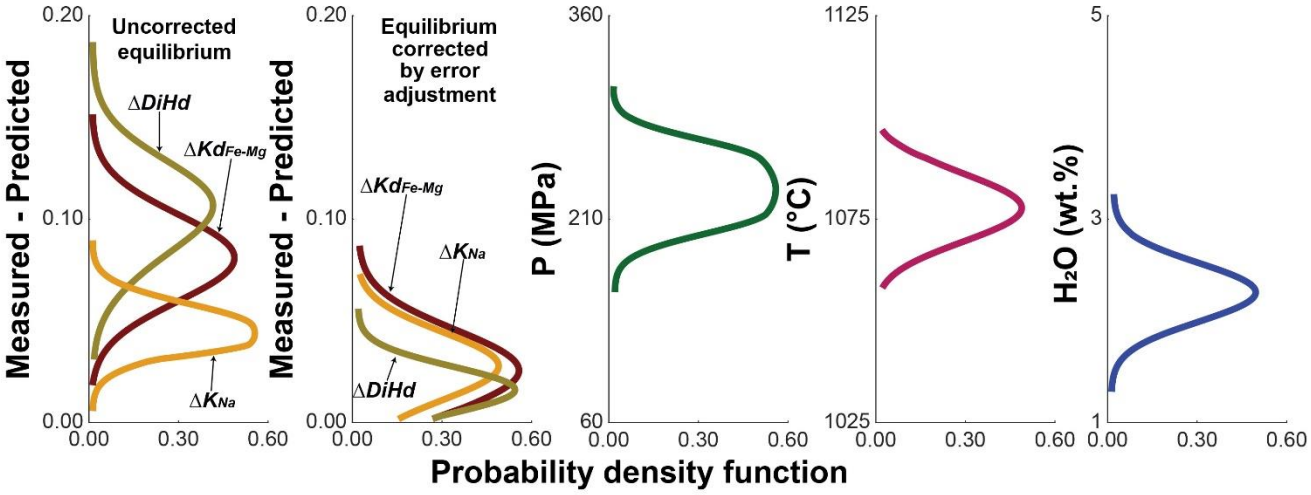
Measured - Predicted
Uncorrected equilibrium
ΔDiHd
ΔKdFe-Mg
ΔKNa
Equilibrium corrected by error adjustment
ΔKdFe-Mg
ΔKNa
ΔDiHd
P (MPa)
T (°C)
H2O (wt.%)
Probability density function

Figure 9

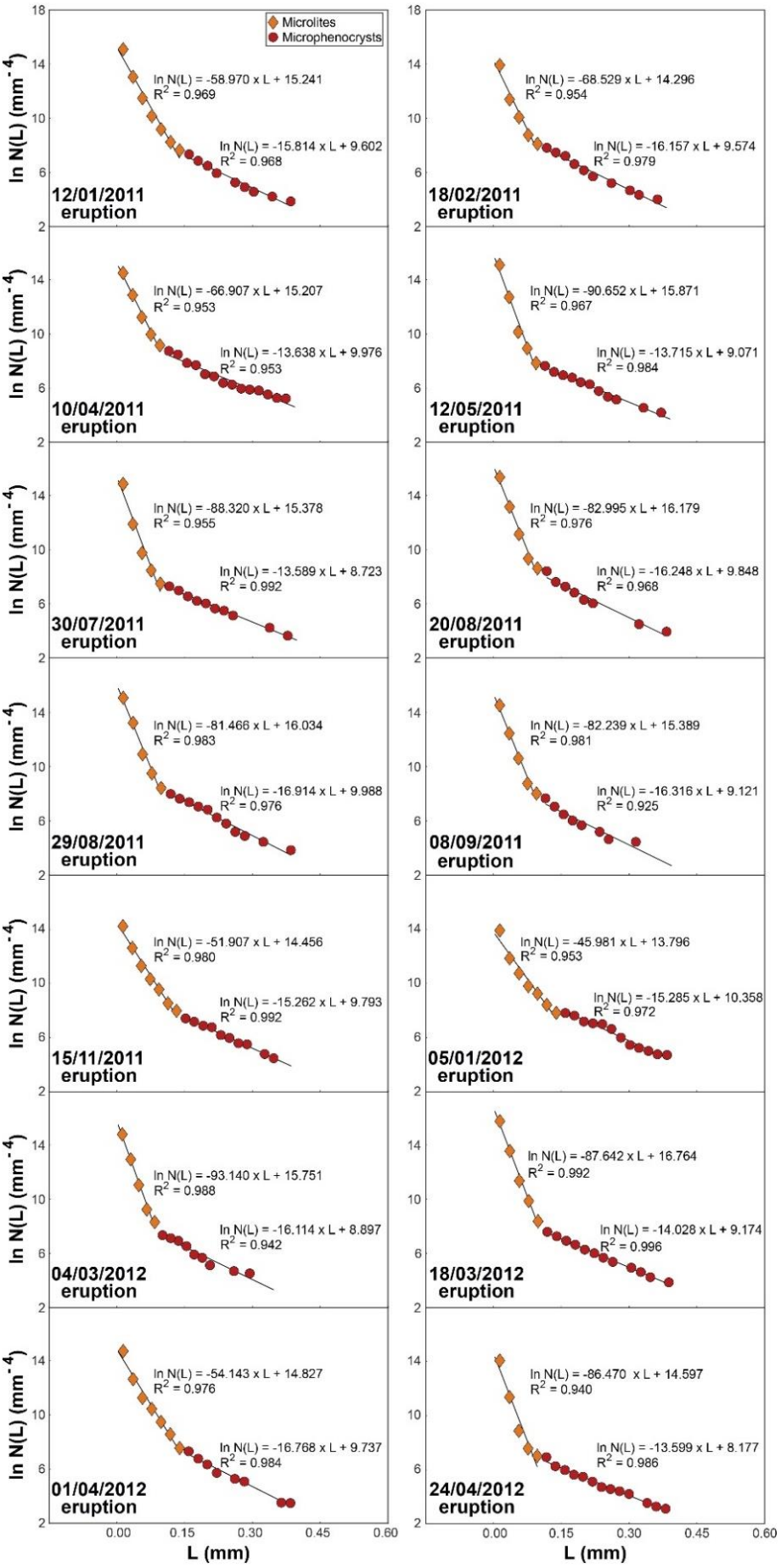
Microlites
Microphenocrysts
ln N(L) = -58.970 x L + 15.241
R2 = 0.969
ln N(L) = -15.814 x L + 9.602
R2 = 0.968
12/01/2011 eruption
ln N(L) = -68.529 x L + 14.296
R2 = 0.954
ln N(L) = -16.157 x L + 9.574
R2 = 0.979
18/02/2011 eruption
ln N(L) = -66.907 x L + 15.207
R2 = 0.953
ln N(L) = -13.638 x L + 9.976
R2 = 0.953
10/04/2011 eruption
ln N(L) = -90.652 x L + 15.871
R2 = 0.967
ln N(L) = -13.715 x L + 9.071
R2 = 0.984
12/05/2011 eruption
ln N(L) = -88.320 x L + 15.378
R2 = 0.955
ln N(L) = -13.589 x L + 8.723
R2 = 0.992
30/07/2011 eruption
ln N(L) = -82.995 x L + 16.179
R2 = 0.976
ln N(L) = -16.248 x L + 9.848
R2 = 0.968
20/08/2011 eruption
ln N(L) = -81.466 x L + 16.034
R2 = 0.983
ln N(L) = -16.914 x L + 9.988
R2 = 0.976
29/08/2011 eruption
ln N(L) = -82.239 x L + 15.389
R2 = 0.981
ln N(L) = -16.316 x L + 9.121
R2 = 0.925
08/09/2011 eruption
ln N(L) = -51.907 x L + 14.456
R2 = 0.980
ln N(L) = -15.262 x L + 9.793
R2 = 0.992
15/11/2011 eruption
ln N(L) = -45.981 x L + 13.796
R2 = 0.953
ln N(L) = -15.285 x L + 10.358
R2 = 0.972
05/01/2012 eruption
ln N(L) = -93.140 x L + 15.751
R2 = 0.988
ln N(L) = -16.114 x L + 8.897
R2 = 0.942
04/03/2012 eruption
ln N(L) = -87.642 x L + 16.764
R2 = 0.992
ln N(L) = -14.028 x L + 9.174
R2 = 0.996
18/03/2012 eruption
ln N(L) = -54.143 x L + 14.827
R2 = 0.976
ln N(L) = -16.768 x L + 9.737
R2 = 0.984
01/04/2012 eruption
ln N(L) = -86.470 x L + 14.597
R2 = 0.940
ln N(L) = -13.599 x L + 8.177
R2 = 0.986
24/04/2012 eruption
ln N(L) (mm-4)
L (mm)
0.00
0.15
0.30
0.45
0.60
2
6
10
14
18

Figure 10

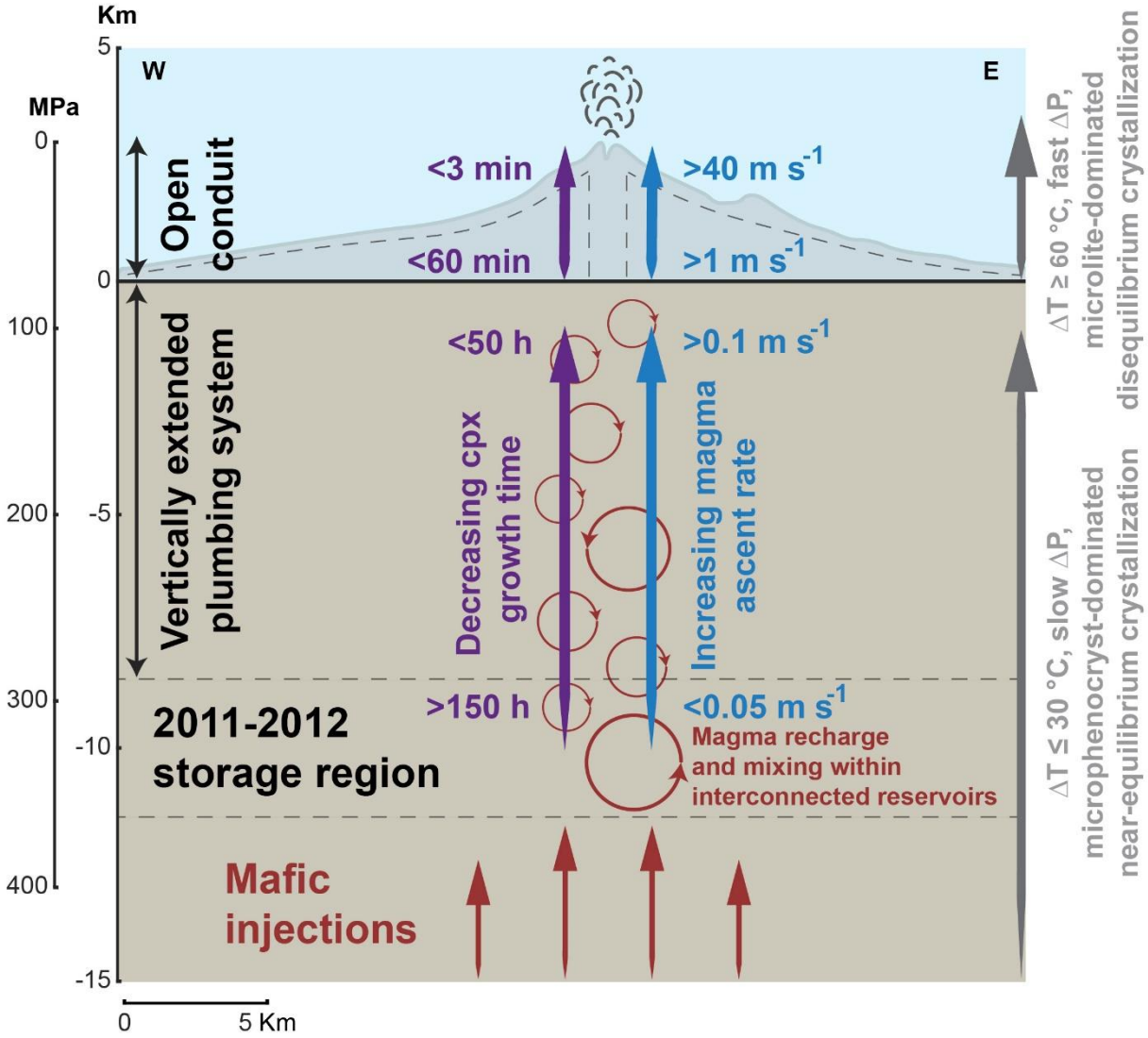
Km
5
W
E
MPa
0
Open conduit
<3 min
>40 m s-1
<60 min
>1 m s-1
0
100
Vertically extended plumbing system
<50 h
>0.1 m s-1
Decreasing cpx growth time
Increasing magma ascent rate
200
-5
ΔT ≥ 60 °C, fast ΔP, microlite-dominated disequilibrium crystallization
300
2011-2012 storage region
>150 h
<0.05 m s-1
Magma recharge and mixing within interconnected reservoirs
-10
ΔT ≤ 30 °C, slow ΔP, microphenocryst-dominated near-equilibrium crystallization
400
Mafic injections
-15
0
5 Km

Figure 11

Tables

Table 1. Experimental conditions and clinopyroxene textural parameters.

	T (°C)	ΔT (°C)	H_2O (wt.%)	CO_2 (wt.%)	t (h)	fO_2 buffer	P_f (MPa)	ΔP (MPa s^{-1})	CR (°C min^{-1})	$G_{max} \times 10^8$ (mm s^{-1})	Area %	S_v^P (mm^{-1})
Isothermal experiments - 300 MPa												
ISO-1100-0H2O	1100	-	0	-	23.70	NNO+2.1±0.2	-	-	-	46.88±7.1	22.82±0.43	571.43±10.42
ISO-1100-2H2O	1100	-	2	-	23.70	NNO+2.1±0.2	-	-	-	56.45±4.96	20.23±0.38	569.3±10.38
ISO-1100-5H2O	1100	-	5	-	23.70	NNO+2.1±0.2	-	-	-	66.25±3.84	18.77±0.35	476.81±8.7
ISO-1100-H2O+CO2	1100	-	2	0.2	23.70	NNO+2.1±0.2	-	-	-	49.44±8.24	22.12±0.42	568.1±10.36
ISO-1075-0H2O	1075	-	0	-	26.87	NNO+2.1±0.2	-	-	-	40.36±4.13	25.18±0.47	539.67±9.84
ISO-1075-2H2O	1075	-	2	-	26.87	NNO+2.1±0.2	-	-	-	46.7±7.76	20.81±0.39	541.16±9.87
ISO-1075-5H2O	1075	-	5	-	26.87	NNO+2.1±0.2	-	-	-	56.53±5.02	20.13±0.38	523.06±9.54
ISO-1075-H2O+CO2	1075	-	2	0.2	26.87	NNO+2.1±0.2	-	-	-	43.14±4.41	23.32±0.44	577.96±10.54
ISO-1050-0H2O	1050	-	0	-	24.00	NNO+2.1±0.2	-	-	-	31.17±3.68	28.47±0.54	729.64±13.31
ISO-1050-2H2O	1050	-	2	-	24.00	NNO+2.1±0.2	-	-	-	41.09±4.85	24±0.45	586.28±10.69
ISO-1050-5H2O	1050	-	5	-	24.00	NNO+2.1±0.2	-	-	-	48.19±1.94	22.38±0.42	532.11±9.71
ISO-1050-H2O+CO2	1050	-	2	0.2	24.00	NNO+2.1±0.2	-	-	-	38.25±4.51	26.18±0.49	592.65±10.81
Decompression experiments - 300 MPa												
DPf-1100-0H2O	1100	-	0	-	0.08	NNO+2.1±0.2	30	0.965	-	5092.01±565.09	9.12±0.16	281.59±5.13
DPf-1100-2H2O	1100	16	2	-	0.08	NNO+2.1±0.2	30	0.965	-	6240.78±832.28	6.94±0.12	175.67±3.2
DPf-1100-5H2O	1100	22	5	-	0.08	NNO+2.1±0.2	30	0.965	-	8677.78±1090.97	5.14±0.09	112.56±2.05
DPf-1100-H2O+CO2	1100	14	2	0.2	0.08	NNO+2.1±0.2	30	0.965	-	5370.43±684.36	7.93±0.14	240.81±4.39
DPf-1050-0H2O	1050	-	0	-	0.08	NNO+2.1±0.2	30	0.980	-	2970.19±225.2	12.83±0.23	392.86±7.16
DPf-1050-2H2O	1050	20	2	-	0.08	NNO+2.1±0.2	30	0.980	-	3960.26±300.26	11.24±0.2	331.47±6.04
DPf-1050-5H2O	1050	30	5	-	0.08	NNO+2.1±0.2	30	0.980	-	5673.47±558.95	8.4±0.15	226.13±4.12
DPf-1050-H2O+CO2	1050	18	2	0.2	0.08	NNO+2.1±0.2	30	0.980	-	3377.53±307.94	12.18±0.22	358.13±6.53
DPs-1100-0H2O	1100	-	0	-	4.01	NNO+2.1±0.2	30	0.019	-	228.86±26.83	17.13±0.31	417.19±7.61
DPs-1100-2H2O	1100	16	2	-	4.01	NNO+2.1±0.2	30	0.019	-	287.4±38.34	15.12±0.27	375.47±6.85
DPs-1100-5H2O	1100	22	5	-	4.01	NNO+2.1±0.2	30	0.019	-	350.34±24.56	14.34±0.26	273.84±4.99
DPs-1100-H2O+CO2	1100	14	2	0.2	4.01	NNO+2.1±0.2	30	0.019	-	270.06±31.66	16.39±0.29	393.29±7.17
DPs-1050-0H2O	1050	-	0	-	4.05	NNO+2.1±0.2	30	0.018	-	139.81±16.51	21.17±0.38	548.21±10
DPs-1050-2H2O	1050	20	2	-	4.05	NNO+2.1±0.2	30	0.018	-	179.9±14.01	19.14±0.34	517.53±9.44
DPs-1050-5H2O	1050	30	5	-	4.05	NNO+2.1±0.2	30	0.018	-	228.94±7.34	17.38±0.31	436.09±7.95
DPs-1050-H2O+CO2	1050	18	2	0.2	4.05	NNO+2.1±0.2	30	0.018	-	157.29±18.57	20±0.36	537.89±9.81
Cooling rate experiments - 300 MPa												
CR-1050-0.25	1050	125	2	-	0.25	NNO+2	-	-	80	1706.11±134.49	37.11±0.67	1194.08±21.79
CR-1050-0.5	1050	125	2	-	0.5	NNO+2	-	-	80	1323.1±104.61	36.23±0.66	1365.44±24.91

CR-1050-1	1050	125	2	-	1	NNO+2	-	-	80	708.45±83.66	35.81±0.65	1359.31±24.8
CR-1050-4	1050	125	2	-	4	NNO+2	-	-	80	208.29±26.34	33.32±0.6	895.86±16.34
CR-1050-24	1050	125	2	-	24	NNO+2	-	-	80	62.53±6.47	32.38±0.59	847.57±2.74
CR-1050-72	1050	125	2	-	72	NNO+2	-	-	80	24.58±2.53	31.96±0.58	814.87±1.73

Table 2. Clinopyroxene lenght, CSD slope and intercept, maximum growth time and ascent rate of 2011-2012 lava fountains.

Eruption date	Clinopyroxene population	Crystal length (L) (mm)	CSD slope (m) (mm^{-1})	CSD intercept (N_0) (mm^{-4})	Maximum growth time (min)	error (±)	Maximum growth time (h)	error (±)	Ascent rate ($m\ s^{-1}$) 1.5 km depth	error (±)	Ascent rate ($m\ s^{-1}$) 10 km depth	error (±)
12/01/2011	Microlite	L < 0.14	-58.970	15.241	10.85	2.82	0.18	0.05	2.30	0.60	-	-
	Microphenocryst	0.14≤ L <0.4	-15.814	9.602	4122.86	1071.94	68.71	17.87	-	-	0.04	0.01
18/02/2011	Microlite	L < 0.1	-68.529	14.296	5.51	1.43	0.09	0.02	4.54	1.18	-	-
	Microphenocryst	0.1 ≤ L < 0.4	-16.157	9.574	3742.32	973.00	62.37	16.22	-	-	0.04	0.01
10/04/2011	Microlite	L < 0.1	-66.907	15.207	6.14	1.60	0.10	0.03	4.07	1.06	-	-
	Microphenocryst	0.1 ≤ L < 0.4	-13.638	9.976	8039.13	2090.17	133.99	34.84	-	-	0.02	0.01
12/05/2011	Microlite	L < 0.1	-90.652	15.871	1.56	0.41	0.03	0.01	16.04	4.17	-	-
	Microphenocryst	0.1 ≤ L < 0.4	-13.715	9.071	7837.45	2037.74	130.62	33.96	-	-	0.02	0.01
30/07/2011	Microlite	L < 0.1	-88.320	15.378	1.75	0.46	0.03	0.01	14.26	3.71	-	-
	Microphenocryst	0.1 ≤ L < 0.4	-13.589	8.723	8173.49	2125.11	136.22	35.42	-	-	0.02	0.01
20/08/2011	Microlite	L < 0.1	-82.995	16.179	2.32	0.60	0.04	0.01	10.77	2.80	-	-
	Microphenocryst	0.1 ≤ L < 0.4	-16.248	9.848	3648.66	948.65	60.81	15.81	-	-	0.05	0.01
29/08/2011	Microlite	L < 0.1	-81.466	16.034	2.52	0.66	0.04	0.01	9.90	2.57	-	-
	Microphenocryst	0.1 ≤ L < 0.4	-16.914	9.988	3043.65	791.35	50.73	13.19	-	-	0.05	0.01
08/09/2011	Microlite	L < 0.1	-82.239	15.389	2.42	0.63	0.04	0.01	10.34	2.69	-	-
	Microphenocryst	0.1 ≤ L < 0.4	-16.316	9.121	3580.53	930.94	59.68	15.52	-	-	0.05	0.01
15/11/2011	Microlite	L < 0.14	-51.907	14.456	19.30	5.02	0.32	0.08	1.30	0.34	-	-
	Microphenocryst	0.14 ≤ L < 0.4	-15.262	9.793	4839.92	1258.38	80.67	20.97	-	-	0.03	0.01
05/01/2012	Microlite	L < 0.14	-45.981	13.796	33.36	8.67	0.56	0.14	0.75	0.19	-	-
	Microphenocryst	0.14 ≤ L < 0.4	-15.285	10.358	4807.14	1249.86	80.12	20.83	-	-	0.03	0.01
04/03/2012	Microlite	L < 0.1	-93.140	15.751	1.38	0.36	0.02	0.01	18.13	4.71	-	-
	Microphenocryst	0.1 ≤ L < 0.4	-16.114	8.897	3787.60	984.78	63.13	16.41	-	-	0.04	0.01
18/03/2012	Microlite	L < 0.1	-87.642	16.764	1.82	0.47	0.03	0.01	13.77	3.58	-	-
	Microphenocryst	0.1 ≤ L < 0.4	-14.028	9.174	7080.91	1841.04	118.02	30.68	-	-	0.02	0.01
01/04/2012	Microlite	L < 0.14	-54.143	14.827	15.96	4.15	0.27	0.07	1.57	0.41	-	-
	Microphenocryst	0.14 ≤ L < 0.4	-16.768	9.737	3165.10	822.93	52.75	13.72	-	-	0.05	0.01
24/04/2012	Microlite	L < 0.1	-86.470	14.597	1.93	0.50	0.03	0.01	12.96	3.37	-	-
	Microphenocryst	0.1 ≤ L < 0.4	-13.599	8.177	8146.40	2118.06	135.77	35.30	-	-	0.02	0.01

Supplementary data to this article can be found online at https://doi.org/10.1016/j.lithos.2021.106225.

A review of plagioclase growth rate and compositional evolution in mafic alkaline magmas: Guidelines for modeling plumbing system dynamics at Stromboli and Mt. Etna

[1]Piergiorgio Moschini, [1,2]Silvio Mollo, [2]Alessio Pontesilli, [2]Manuela Nazzari, [3]Chiara Maria Petrone, [4]Sara Fanara, [5]Alessandro Vona, [1]Mario Gaeta, [5]Claudia Romano, [2]Piergiorgio Scarlato

[1]Department of Earth Sciences, Sapienza - University of Rome, P. le Aldo Moro 5, 00185 Roma, Italy

[2]Istituto Nazionale di Geofisica e Vulcanologia - Department Roma 1, Via di Vigna Murata 605, 00143 Roma, Italy

[3]The Natural History Museum, Department of Earth Sciences, Cromwell Road, SW7 5BD London, United Kingdom

[4]Abteilung Experimentelle und Angewandte Mineralogie, Georg August Universität Göttingen, Goldschmidtstraße 1, 37077 Göttingen, Germany

[5]Dipartimento di Scienze, Università degli Studi Roma Tre, L.go San Leonardo Murialdo 1, 00146 Roma, Italy

Corresponding author:

Piergiorgio Moschini

piergiorgio.moschini@uniroma1.it

Department of Earth Sciences,

Sapienza - University of Rome,

P. le Aldo Moro 5,

00185 Roma, Italy

Under review in Earth-Science Reviews

Abstract

Mafic alkaline magmas, such as those feeding the persistent eruptive activity of Stromboli and Mt. Etna volcanoes in Italy, are dominated by the crystallization of plagioclase via cooling and degassing phenomena related to the dynamics of shallow crustal reservoirs and eruptive conduits. Because plagioclase textures and compositions are extremely sensitive to the changes of intensive variables in subvolcanic plumbing systems, the phenomenological variability of erupted crystals preserves detailed evidence of complex growth histories. From this point of view, we reappraise the textural maturation and compositional complexity of plagioclase by allying thermodynamic and kinetic principles to natural and experimental observations, with the purpose of drawing up guidelines for reconstructing magma dynamics in mafic alkaline volcanic settings. A multifaceted statistical method is adopted to parameterize the decay of crystal growth rate with increasing crystallization time, as relaxation kinetics prevails over melt supersaturation effects. This model parameterization is combined with the textural analysis of natural plagioclase crystals to quantify the residence time of phenocrysts in equilibrium with magmas at Stromboli and Mt. Etna and/or the timescale of rapid microlite growth during disequilibrium ascent of magmas within the conduit. The role played by temperature and melt-water content on plagioclase components and major cation substitution mechanisms is also evaluated under both isobaric-isothermal and decompression conditions. The emerging paradigm is that the influence of dissolved water on anorthite-albite exchange between plagioclase and melt is overwhelmingly mitigated by changes in temperature. As a corollary, anorthite and albite melt activities are almost fully encapsulated in the variation of anhydrous melt components as the crystallization of plagioclase proceeds during magma cooling. Following this line of reasoning, we propose an integrated modeling approach to decipher complex zoning patterns in natural plagioclase phenocrysts from mafic alkaline eruptions. Key findings from our re-assessment of equilibrium, thermometric, and hygrometric models indicate that temperature and dissolved water can be iteratively estimated for different plagioclase textural patterns if crystals are sufficiently

strongly zoned, and probability-based criteria are applied to determine the maximum probability distribution from kernel density analysis.

Keywords: mafic alkaline magmas; plagioclase-melt equilibria; crystal growth kinetics; crystal zoning patterns

1. Introduction

Plagioclase is one of the most common and investigated mineral phases in volcanic settings, as both its texture and composition are ultimately controlled by plumbing system and conduit dynamics (e.g., Giacomoni et al., 2014; Arzilli et al., 2019). Plagioclase morphological evolution gives rise to a plethora of textural terminologies associated with different magma crystallization conditions (e.g., equant, faceted, tabular, cellular, acicular, hopper, dendritic, skeletal, swallowtail, dusty, spongy, patchy, honeycomb, sieved, etc.; Singer et al., 1993; Hammer and Rutherford, 2002). In the ideal formula of plagioclase (MT_4O_8), cations are ordered in both tetrahedral (T) and octahedral (M) sites, thus forming two characteristic end-members: anorthite ($CaAl_2Si_2O_8$; An) and albite ($NaAlSi_3O_8$; Ab). Intracrystalline heterogeneities in plagioclase are generally described as grading An chemical variations or alternating An-rich and An-poor zones, which are categorized as normal zoning, reverse zoning, concentric zoning, oscillatory zoning, and sector zoning (Smith and Lofgren, 1983).

Different crystal habits and zoning patterns reflect changes in temperature (cooling) and melt-water content (decompression) during convective stirring (Couch et al., 2001) or ascent of magma towards shallower crustal reservoirs (Couch et al., 2003; Brugger and Hammer, 2010; Mollo et al., 2011; Iezzi et al., 2014). Plagioclase preserves evidence of extensive dissolution and recrystallization reactions associated with inputs of hot, water-poor (Cassidy et al., 2016) or water-rich (Cashman and Blundy, 2013) magmas from depth. The saturation temperature of plagioclase may also increase with increasing magma crystallinity as the result of latent heat release during exothermic, decompression-driven crystallization of water-saturated melts (Couch et al., 2003; Blundy et al., 2006).

According to the processes illustrated above, plagioclase is acknowledged as a powerful recorder of the physio-chemical conditions controlling the differentiation of magma and its crystallization history (Putirka, 2008; Humphreys et al., 2016; Pontesilli et al., 2021). Several efforts have been made by authors for interrogating plagioclase textures and compositions in terms of crystal growth dynamics (Cashman, 1993; Agostini et al., 2013; Vona and Romano, 2013; Andrews, 2021),

cation partitioning (Dohmen and Blundy, 2014; Sun et al., 2017), equilibrium components (Ghiorso and Carmichael, 1980; Glazner, 1984; Putirka, 2005; Namur et al., 2012), thermodynamic, thermometric, and hygrometric modeling (Ghiorso and Carmichael, 1980; Glazner, 1984; Housh and Luhr, 1991; Lange et al., 2009; Putirka, 2005, 2008, 2017; Waters and Lange, 2015; Huggins et al., 2021). The free energy difference between crystal and melt is also responsible for the stability and morphological evolution of plagioclase under cooling and/or decompression-degassing crystallization regimes controlling subvolcanic plumbing system dynamics (Hammer and Rutherford, 2002; Arzilli et al., 2019). In this scenario, reaction kinetics related to the total free energy change of the system are inhibited by the prevailing control of relaxation phenomena on cation equilibrium partitioning as the plagioclase-melt interface approaches equilibrium at lower degrees of undercooling (Mollo et al., 2011; Mollo and Hammer, 2017).

Particular attention is given in this review study to the parameterization of crystal growth kinetics and the modeling of plagioclase equilibrium composition and temperature during solidification of mafic alkaline magmas, such as those typifying the present-day activity at Stromboli and Mt. Etna, two of the most active and monitored volcanoes in Italy and in the world (e.g., La Spina et al., 2016; Di Stefano et al., 2020). Upon identifying disparate aspects of plagioclase growth scenarios, we integrate experimental and natural data from literature with an internally consistent data set retrieved for mafic to intermediate magmas. Plagioclase textural and compositional parameters are comparatively examined under the rationale of thermodynamic and kinetic principles. This approach is pivotal to track the temporal scales of magma dynamics via plagioclase growth histories, as well as to disambiguate the role of temperature and melt-water content on plagioclase zoning patterns at Stromboli and Mt. Etna. Our final purpose is to provide a comprehensive background for future investigations, as well as informative guidelines and a secure methodology to model pre- and syn-eruptive conditions in active volcanic settings.

2. Methods

For the purpose of this study, we present here an internally consistent data set consisting of seventy-two new experiments carried out using as natural starting materials two mafic alkaline basalts erupted at Mt. Etna (i.e., Monte Maletto Formation dated ~7 kyr ago) and Stromboli (i.e., 3 July 2019 paroxysm).

2.1 Experimental procedure

The powdered rocks are melted to ensure homogeneity at the HP-HT Laboratory of Experimental Volcanology and Geophysics of the Istituto Nazionale di Geofisica e Vulcanologia (INGV), Rome, Italy. A crucible containing the natural powder is loaded in a 1 atm vertical tube CO–CO_2 gas-mixing furnace at 1300 °C for 1 h. The redox state is 2 log unit above the Ni-NiO buffer (NNO+2), comparable to the oxygen fugacity estimated at Mt. Etna (Mollo et al., 2015a) and Stromboli (Di Stefano et al., 2020). Iron loss is kept to < 5% of the initial amount by adopting a Fe pre-saturated Pt crucible. Quenched glasses are analyzed by scanning electron microscopy and no crystalline phases are detected. Averages of twenty microprobe analyses of different glass chips for Mt. Etna and Stromboli are reported in Supplementary Material 1.

Isothermal-isobaric and decompression experiments are carried out in an internally heated pressure vessel (IHPV) equipped with a continuum decompression system and a rapid quenching device (drop quench) at the Abteilung Experimentelle und Angewandte Mineralogie, Georg August Universität Göttingen in Germany (Supplementary Material 1). Powdered starting glasses are loaded in Fe-presaturated Pt-capsules (e.g., Gaetani and Grove, 1998). Isothermal-isobaric experiments are conducted at 300 MPa and 1150, 1125, 1100, 1075, and 1050 °C. These experimental conditions reproduce most of magma crystallization paths at Mt. Etna (Mollo et al., 2015a) and Stromboli (Di Stefano et al., 2020). Experiments are heated directly to the target temperature at a rate of 50 °C min^{-1} and then the temperature is kept constant for ~23-27 h. No superliquidus pretreatment is imposed to the experimental charge and the system relaxes toward equilibrium as temperature and pressure are

kept constant over the experimental time (cf. Moschini et al., 2021). Decompression experiments are conducted at the same temperatures of isothermal-isobaric runs by depressurizing the charges from 300 to 30 MPa at slow (0.018 MPa s^{-1}) and fast (0.98 MPa s^{-1}) rates over experimental times of ~4 h and ~5 min, respectively (Supplementary Material 1). Depressurization rates are selected in conformity with magma ascent velocities in the upper crust (0.45-24.5 m s^{-1}), as reported in geophysical, petrological, and numerical studies on Mt. Etna and Stromboli (Aloisi et al., 2006; Mollo et al., 2015b; La Spina et al., 2016, 2021; Polacci et al., 2019; Moschini et al., 2021). Water solubility in the mafic alkaline basalts is ~3 wt.% at 300 MPa under isothermal-isobaric equilibrium, whereas disequilibrium degassing due to melt decompression results in volatile supersaturation and kinetic melt-fluid fractionation (Mollo et al., 2017). On this basis, deionized water (up to ~5 wt.%) and oxalic acid (~0.2 wt.% CO_2 by thermal decomposition) are added to the starting materials to attain both fluid-absent and fluid-present crystallization conditions (Supplementary Material 1). Plagioclase liquidus is independent of P_{H2O} under fluid-absent crystallization conditions. Conversely, under fluid-present crystallization conditions, plagioclase liquidus is controlled by volatile exsolution that imposes an actual undercooling variable of 14 to 30 °C (Moschini et al., 2021). Undercooling is regarded as the difference between the system temperature and the temperature at which a mineral phase saturates in the given liquid (Kirkpatrick, 1981). The degree of undercooling is associated with either a decrease in temperature or compositionally induced increase of melt's liquidus temperature by decompression under H_2O-saturated conditions. The term actual undercooling is used to distinguish the driving force induced by compositional change from that of temperature change, as reported in Mollo and Hammer (2017). In both cases, the actual undercooling is quantified by the difference between the phase-in and system temperatures. In our decompression experiments, plagioclase liquidus as a function of P_{H2O} and T has been determined by Moschini et al. (2021) using the MELTS code (v.1.2.0; Gualda et al., 2012). The experimental temperature is monitored by three S-type (Pt90Rh10/Pt with uncertainty of ±3 °C) thermocouples and pressure is recorded by a transducer, calibrated against a Heise tube gauge with accuracy ±5 MPa. Experiments are quenched

using a drop quench device imposing a cooling rate of ~150 °C s^{-1}. The use of Ar as a pressure medium provided an intrinsic fO_2 variable from NNO+2 to NNO+4 (Schanofski et al., 2019). Within the sample capsule, fH_2 is controlled by hydrogen permeation through the capsule walls driven by the fugacity gradient between the pressure medium and the capsule interior. Hydrogen permeation determined the fO_2 inside the capsule through the equilibrium: $H_2 + 1/2\ O_2 \leftrightarrow H_2O$. However, under fluid-present conditions and with the addition of CO_2, the redox state of the system changes in response to the variable activity of water in the melt (Botcharnikov et al. 2008). Under such conditions, a more accurate fO_2 estimate is obtained at the end of experimental runs through the oxygen barometer of Ishibashi (2013) that is based on spinel–melt equilibria in alkaline systems, with uncertainty ±0.3 log unit. This model returns fO_2 estimates variable from NNO+1.9 and NNO+2.3 buffer, as reported in Moschini et al. (2021).

2.2 Microchemical analysis

Major element concentrations are obtained at the HP-HT Lab of INGV using a JEOL-JXA8200 electron probe micro-analyzer (EPMA) equipped with five wavelength dispersive spectrometers (Supplementary Material 2). For glasses, a slightly defocused 5 μm beam is used with a counting time of 5 s on background and 15 s on peak. For crystals, beam size is 1 μm with a counting time of 20 and 10 s on peak and background, respectively. The analytical conditions are 15 kV accelerating voltage and 10 nA beam current. The following standards are used for calibration: jadeite (Si and Na), corundum (Al), forsterite (Mg), andradite (Fe), rutile (Ti), orthoclase (K), apatite (P), and spessartine (Mn). Sodium and potassium are analyzed first to prevent alkali migration effects. Counting statistics are used to determine precision for each element on each analysis, whereas the secondary standards are used to determine the accuracy. Precision and accuracy are better than 5% for all cations.

Raman spectra are acquired at EVPLab of Roma Tre University (Rome, Italy) using a Jobin Yvon LABRAM HR800 Horiba micro-Raman spectrometer, equipped with an attenuated doubled

Nd3:YAG laser (532 nm wavelength) and calibrated using a silicon standard. The operating conditions are 600 grooves/mm grating density, confocal hole opening 300 μm, and slit aperture 200 μm, exposure time of 60 s (3 times). The laser power at source is 60 mW (0.15 mW on the sample surface). A nominal spatial resolution of ~5 μm^2 is obtained with the 100× objective. For each sample, 5 spectra are acquired to assess data reproducibility. The backscattered Raman radiation is collected over ranges of 100-1500 cm^{-1} and 2700-4000 cm^{-1}, corresponding to low-wavenumber (*LW*) silicate and high-wavenumber (*HW*) water regions, respectively. The Matlab© code developed by Di Genova et al. (2017) is used to perform Long correction (Long, 1977), background subtraction, and *HW*/*LW* parameterization (i.e., Raman band area ratio). For the quantification of melt-water content, Raman spectra are standardized against a set of well characterized glasses with mafic alkaline compositions (see Mollo et al., 2017). Their water contents are independently determined by Fourier transform infrared spectroscopy (FTIR) and Karl Fischer titration (KFT). Raman data and calibration fit [$(HW/LW)_{Raman}$ against $H_2O_{Standard}$] are reported in Supplementary Material 3.

2.3 Textural analysis

Photomicrographs are collected in backscattered electron (BSE) mode with a JEOL 6500F field emission gun scanning electron microscope (FE-SEM) equipped with an energy-dispersive spectrometer (EDS) detector at the HP-HT Lab of INGV. The acquired photomicrographs are processed using NIH ImageJ software and reduced to binary images (i.e., black and white color) by grey level thresholding (i.e., image segmentation). The uncertainty associated with the segmentation process is evaluated by adding/subtracting pixel layers around each crystal in the binary image (cf. Pontesilli et al., 2019). Error propagation analysis yields an uncertainty of 30% for the determination of plagioclase growth rate. The Matlab© code designed by Moschini et al. (2021) is used to perform image processing operations and measure equal-area best-fit ellipses and lengths of major (*L* in mm) and minor (*W* in mm) axes. Following Armienti et al. (1994) and Armienti (2008), crystals with $L <$ 0.006 mm are considered artefacts produced by image segmentation analysis carried out with NIH

ImageJ software and are removed from the data set, together with crystal fragments at the edge of photomicrographs.

Crystal size distribution (CSD) analysis is carried out through *CSDCorrection*s 1.38 (Higgins, 2000) to determine binned curves sorted in different crystal size classes. Intersection planar data are converted in volume data by applying stereological correction to retrieve the actual distribution of crystal sizes from the measured population of intersections (Higgins, 2000). This correction method accounts for 1) potential cut-section effects in case of larger crystals cut by a plane shifted with respect to the center, therefore contributing to smaller crystal populations, and 2) intersection probability effects when, for a poly-disperse distribution, smaller crystals are less likely to be intersected by a plane than larger crystals (Higgins, 2000). The crystal aspect ratio (*L*/*W*) is determined by *CSDslice* (Morgan and Jerram, 2006), in which 2D raw data are compared with a crystal habit database to constrain the five best-matching 3D crystal shapes. CSD diagrams are in the form of semi-logarithmic ln*N(L)* against *L* plots (Marsh, 1988):

$$\ln N(L) = \frac{-L}{G\,\tau} + \ln N_0 \qquad (1)$$

where *N(L)* is the number of crystals per unit length per unit volume (i.e., the density distribution of crystals per unit volume per bin size), *G* is the crystal growth rate, τ is the steady-state crystallization time, and N_0 is the nucleation density (i.e., the number of crystals of zero size). The linear regression fit of a CSD curve has slope $m = 1 / (G \times \tau)$ and intercept $b = \ln(N_0)$.

Knowing that τ from classical CSD theory can be rewritten as *t*, the volumetric growth rate of plagioclase for the mean area investigated is calculated through the formulation:

$$G = (L\,W)^{0.5} / (2\,t) \qquad (2)$$

where the factor ½ accounts for the growth of crystals in both directions. L and W are measured as the average of ten largest crystals and their incorporation in Eq. (2) has the virtue of minimizing the uncertainty related to crystal size classification and quantification. This increases the probabilities to intersect the true maximum L. Moreover, crystal inequidimensionality and sectioning artefacts related to crystal cuts are mediated over both major and minor lengths (Fenn, 1977; Swanson, 1977).

2.4 Statistical analysis

Through the statistical algorithm of Statgraphics Centurion 18® (Statpoint Technologies, Inc., Warrenton, VA, USA), we perform multivariate regression analysis among different variables to determine the *p-value*. This is an important metric for identifying the best subset of independent *n* variables relative to a selected target variable. The *p-value* is a probability number describing the likelihood that the data distribution occurs under the null hypothesis. If the null hypothesis is true, an independent *n* variable has no significant effect over the target variable. If the null hypothesis is rejected, the alternate hypothesis is that the independent *n* variable has a significant effect on the target variable. A *p-value* < 0.05 is assumed as a statistically significant result, which implies that the null hypothesis should be rejected. In conjunction with *p-value*, the product moment correlation coefficient *Pearson's r* is derived from the correlation matrix to quantify the strength of correlation among *n* variables. Statistical significance of *Pearson's r* = ±1 is equivalent to $\pm 1^2 \times 100 = 100\%$ of correlation, whose magnitude ranges between −1 (highest negative correlation) and +1 (highest positive correlation). *Pearson's r* from a correlation matrix is proportional to the standardized regression coefficient *I* derived by multiple linear regression analysis. *I* in percentage represents the influence exerted by independent *n* variables on the target variable, calculated as the unstandardized regression coefficient of the independent variable multiplied by its standard deviation and divided by the standard deviation of the target variable. To test if regression variables are indeed independent or, alternatively, are highly correlated providing unreliable regression statistics (i.e., multicollinearity), the variance inflation factor (*VIF*) is employed. *VIF* quantifies how much the variance of a coefficient

is inflated because of linear dependence with other regression variables and values exceeding 10 are often regarded as indicating multicollinearity (Hair et al., 1995).

Multiple linear regression analysis is adopted in this study to develop and test different models. With this approach some independent variables may closely describe the variance of the data, whereas some others may generate a set of predictions with low degrees of freedom that lead to data overfitting. We identify and remove variables that do not improve the fit by using *a priori* the correlation matrix and assuming as unsuitable predictors those with *p-value* ≥ 0.05, *Pearson's r* ≤ 0.60 (as absolute value), and *VIF* > 10. Among all the remaining filtered predictors, we select the best independent variables for the model through the *Mallows' Cp* statistic. This parameter is expressed as $RSS_k/RSS_p - n + 2p$, where RSS_k is the ratio of the residual sum of squares of all predictors k, RSS_p is the residual sum of squares of only p of the k predictors, and n is the number of observations. *Mallows' Cp* is a measure of the bias in a model: if the type and number of selected predictors p (including the constant term in linear regression) are sufficient to provide a good description of the data, then *Cp* has values as close as possible to p. The accuracy of the calibrated model is verified as follows: 1) ~20% of data are randomly subtracted from the data set before the regression analysis, 2) the remaining ~80% of the data are regressed to derive a preliminary model, 3) subtracted data are used as test data for the preliminary model, and 4) the whole data set is regressed to calculate the overall predictive model. Regression statistics associated with these calculations are the coefficient of determination (R^2), standard error of estimate (*SEE*), and average absolute deviation (*AAD*).

3. Plagioclase growth rate parameterization

3.1. Plagioclase growth principles

The crystal growth process is strictly related to crystal-melt interface kinetics resulting from the attachment/detachment of cations to the advancing crystal interface and the diffusion of chemical components in the liquid (Jackson, 1969; Dowty, 1980; Kirkpatrick, 1981; Cashman, 1990; Lasaga,

1998; Hammer, 2008; Mollo and Hammer, 2017). Attainment of bulk thermodynamic equilibrium (i.e., a minimum energy state) at the crystal-melt interface corresponds to a time-independent steady-state crystallization condition at which the crystal growth is halted (Tsuchiyama, 1983). Because crystallization is an exothermic process, the crystal growth rate depends on the temperature at which interface kinetics develop. Hence, a certain degree of undercooling is essential to promote the growth and textural maturation of crystals (Kirkpatrick, 1981). For a small degree of undercooling, the crystal growth rate initially increases towards a maximum corresponding to a small energetic barrier to overcome for the attachment of atoms on the advancing plagioclase surface (Kirkpatrick et al., 1979; Muncill and Lasaga, 1987). However, as the degree of undercooling increases, the crystal growth rate does not further increase but rather decreases, as the activation energy for cation attachment onto the plagioclase surface becomes prohibitively large (Kirkpatrick et al., 1979; Muncill and Lasaga, 1987).

Interface kinetics resulting from a large degree of undercooling lead to development of diffusive boundary layers in the melt next to the advancing plagioclase surfaces (Lofgren, 1980). Under such condition, the solidifying system shifts from an interface-controlled crystallization regime to a diffusion-controlled regime (Hammer and Rutherford, 2002; Couch et al., 2003). Imbalance between crystal growth rate and diffusion of cations in the melt implies that the compositional difference between diffusive and far field melt is proportional to the degree of undercooling (Tsuchiyama, 1983, 1985; Mollo et al., 2011). Therefore, in a supersaturated melt, the driving force of undercooling for the crystal growth approximates to supersaturation gradients arising from concentration-dependent reactions induced by interface kinetics (Tsuchiyama, 1983, 1985; Mollo et al., 2011). In other words, both the effects of supersaturation and undercooling are imputable to the same process, as outlined by Kirkpatrick (1981). Moreover, the crystal growth rate approaches to zero as diffusion gradients in the melt decrease over time and the system relaxes toward equilibrium, in response to a minimum free energy difference between crystal and melt.

Initial supersaturation effects and compositional heterogeneities at the interface melt are counterbalanced by relaxation phenomena that become more effective over the timescale of

crystallization (Hammer, 2008). Relaxation kinetics lower the concentration gradients at the crystal-melt interface and favor a steady-state textural maturation of crystals, with development of euhedral forms (Kirkpatrick, 1975). As a consequence, the crystal growth is not always linear in the early stages of crystallization and plagioclase may take time for the establishment of equilibrium texture, a condition at which the growth rate goes to zero (Nabelek et al., 1978). An important consequence of melt relaxation is that the crystal growth rate of plagioclase progressively decreases with increasing crystallization time until bulk chemical gradients cease, and the interface melt returns to homogeneous concentrations (Grove, 1978; Cashman, 1993; Kohut and Nielsen, 2004; Hammer, 2008). Near-equilibrium crystallization conditions are restored when the effect of interface kinetics becomes small and attachment/detachment reactions of cations from the melt onto the crystalline surface (and *vice versa*) occur at comparable rate (Pontesilli et al., 2019).

Because the effect of undercooling and the mobility of melt components are interdependent, crystal growth rate changes as a function of melt composition and viscosity (Zhang, 2010; Vetere et al., 2015). In silicate melts, the energetic barrier to overcome for the onset of nucleation roughly scales with the proportion of tetrahedral relative to octahedra sites, which corresponds to the degree of melt polymerization (Naney and Swanson, 1980; Kirkpatrick, 1983). The internal structure of silicate melt can be assumed as an equilibrium arrangement of silicon-oxygen-metal bonds, in terms of bond lengths and strengths (Bottinga and Weill, 1972). For each subliquidus temperature, a specific equilibrium internal structure must be attained by the melt to nucleate a stable crystalline phase. The effect of undercooling determines a rearrangement of the melt internal structure, which progressively attains a new equilibrium state over a certain time. This temporal interval is defined as incubation time (or lag time) and corresponds to a delay in the crystallization of mineral phases from structurally unrelaxed melts (Swanson, 1977; Tsuchiyama, 1983; Hammer, 2008). In more polymerized melts, the number of oxygens bonded to two tetrahedrally coordinated cations (i.e., bridging oxygens *BO*) increases, whereas the number of oxygens bonded to a tetrahedrally coordinated cation and to a different cation in another coordination state (i.e., non-bridging oxygens *NBO*) decreases. The

parameter NBO/T^{melt}, defined as to the number of *NBO* per tetrahedrally coordinated cations *T*, is used to quantify melt structural changes as a function of compositional variations (Mysen et al. 1985). As the degree of undercooling increases, melts with low NBO/T^{melt} are less inclined to crystallize than those with high NBO/T^{melt} and, comparatively, Si–O rich crystals appear more delayed than Si–O poor ones (Iezzi et al., 2011). Dissolved H_2O also controls the melt structure and viscosity, by producing more depolymerized melts with dramatic effects on the nucleation density and growth rate of plagioclase, as described in Fenn (1977). According to this proposition, the growth rate of plagioclase is observed to decrease with increasing the amount of albite relative to anorthite components in the melt phase (Kirkpatrick et al., 1979, 1983; Muncill and Lasaga, 1987). Moreover, owing to the difference in bonding energy between Si-O (443 kJ mol^{-1}) and Al-O (330-422 kJ mol^{-1}), the transfer of Al^{3+} cations from the melt to the surface of a rapidly growing plagioclase crystal is more facilitated than the transfer of Si^{4+} cations (Iezzi et al., 2011). As a consequence, under cooling-induced crystallization regimes, Ab-rich plagioclase crystals are delayed relative to An-rich ones, such as the delay time increases with increasing undercooling (Mollo et al., 2011, 2012; Iezzi et al., 2014). An opposite effect is documented under decompression-induced crystallization regimes where undercooling is governed by the exsolution of water from the melt (Pupier et al., 2008; Crabtree and Lange, 2011; Waters et al., 2015). A progressive decrease of water concentration dissolved in the melt rises the liquidus-solidus loop of plagioclase for the Ab-An system by changing its topology and enlarging the stability of low-temperature sodic end-member relative to the high-temperature calcic one. The composition of plagioclase resulting from more degassed and undercooled melts becomes preferentially enriched in Ab and depleted in An components (Pupier et al., 2008; Crabtree and Lange, 2011; Waters and Lange, 2015).

3.2 Growth-related plagioclase parameters

The textural change of plagioclase from isobaric-isothermal and decompression experiments from this study and carried out on Mt. Etna and Stromboli mafic alkaline melts conforms to previous

observations reported in a plethora of experimental and natural studies investigating basaltic to rhyolitic terrestrial rocks and lunar samples (Moore and Evans, 1967; Lofgren, 1974; Ikeda, 1977; Swanson, 1977; Wright and Okamura, 1977; Grove, 1978; Nabelek et al., 1978; Corrigan, 1982; Kouchi et al., 1986; Shirley, 1987; Muncill and Lasaga, 1987, 1988; Grove, 1990; Kirkpatrick, 1981; Hammer and Rutherford, 2002; Cashman and Marsh, 1988; Kneedler, 1989; Cashman, 1990, 1993; Cashman et al., 1999; Burkhard, 2002, 2005a, 2005b; Couch, 2003; Couch et al., 2003; Kohut and Nielsen 2004; Simakin and Salova, 2004; Larsen, 2005; Conte et al., 2006; Hammer, 2008; Orlando et al., 2008; Pupier et al., 2008; Schiavi et al., 2009, 2010; Brugger and Hammer, 2010; Crabtree and Lange, 2011; Mollo et al., 2011; Mollard et al., 2012; Agostini et al., 2013; Iezzi et al., 2011, 2014; Shea and Hammer, 2013; Arzilli et al., 2019; Giuliani et al., 2020; Le Gall et al., 2021). We will not reiterate here the textural evolution of plagioclase under interface-controlled and diffusion-controlled growth regimes but rather point to the primary motivation of our experiments, which is the parameterization of plagioclase growth rate in mafic systems.

In short, the mineral phase assemblage of our experiments consists of plagioclase + clinopyroxene ± titanomagnetite (Supplementary Material 1), as already documented in previous experimental works on Stromboli (Agostini et al., 2013 and references therein) and Mt. Etna (Mollo et al., 2018 and references therein). The aspect ratio of plagioclase is observed to change from ≤7 (blocky, prismatic, and tabular) to ≥11 (elongate and acicular) from isothermal-isobaric to decompression conditions (Supplementary Material 1). As the depressurization rate increases, the plagioclase growth rate expressed on a logarithmic scale increases from -14 to -8 mm s^{-1} (Fig. 1a). According to Couch (2003), interface kinetics favors the onset of plagioclase crystals with larger sizes and higher aspect ratios (Supplementary Material 1). Much slower growth rates from -16 to -15 mm s^{-1} are measured for smaller plagioclase crystals obtained from isobaric-isothermal experiments (Fig. 1a). Under these conditions, plagioclase growth is hindered by sluggish kinetic effects resulting from minimum free energy difference between melt and crystal (Hammer and Rutherford, 2002; Hammer, 2008). The growth rate sightly increases with increasing the system temperature and melt-water

content (Fig. 1a,b), in response to a faster chemical diffusion of crystal-forming components in the melt phase (Pupier et al., 2008; Shea and Hammer, 2013; Iezzi et al., 2014; Giuliani et al., 2020).

To understand the correlation between growth rate and other system variables in our experiments that may govern the crystallization process of plagioclase, we adopt multivariate regression analysis by selecting as input parameters the growth rate ($\ln G$), degree of undercooling (ΔT), crystallization temperature (T), crystallization time ($\ln t$), melt composition/structure (NBO/T^{melt}), and melt-water concentration (H_2O^{melt}). Undercooling and crystallization time parameters are expressed on a logarithmic scale to facilitate the mathematical treatment of their small and large quantities. Results from correlation matrix indicate that *p-values* for *lnt* (0.00), ΔT (0.00), and T (0.04) are statistically significant for the overall description of *lnG*. Conversely, no obvious correlation is found between *lnG* and H_2O^{melt} and NBO/T^{melt}, in accord with large *p-values* of 0.71 and 0.48, respectively. We observe that, for subtle compositional ranges confined to mafic systems, the effects of melt-water content and melt depolymerization remain subordinate to the crystallization time and degree of undercooling. *Pearson's r* quantifies the strength of correlation between *lnG* and *lnt* (-0.99), ΔT (0.52), T (-0.25), H_2O^{melt} (-0.05), and NBO/T^{melt} (0.09). A strong negative dependence is found between *lnG* and *lnt*, whereas the correlation between *lnG* and H_2O^{melt} and NBO/T^{melt} is very weak, in agreement with minimum *p-values* calculated for these parameters. The influence of *lnt* on the magnitude of *lnG* is markedly high and corresponds to 60%. Lower values are determined for ΔT (21%) and T (12%). The influence of H_2O^{melt} and NBO/T^{melt} on *lnG* is only 2% and 4%, respectively, and can be considered negligible.

3.3 Control of crystallization time on growth rate

The diagram *lnG* against *lnt* in Fig. 2a shows a net linear decay of plagioclase growth rate from this study with increasing crystallization time. This general trend reflects the achievement of chemical equilibrium over time by diffusive relaxation and minimization of supersaturation effects at the crystal-melt interface (Kirkpatrick, 1981; Kohut and Nielsen, 2004; Hammer, 2008; Pontesilli et

al., 2019; Moschini et al., 2021). To understand the role played by relaxation kinetics on crystal growth, we must recall that at high supersaturation the crystal growth rate exceeds the diffusion of melt components, such that diffusive boundary layers enriched in incompatible components surround the crystal surfaces (Watson and Muller, 2009). Disequilibrium growth may take place in presence of a very thin and not detectable diffusive boundary layer around the crystal. This aspect is not trivial in mafic, depolymerized, low viscosity melts, where diffusion gradients are restricted to the interaction of cations at the crystal-melt interface over length scale from a few microns or even less (Watson and Muller, 2009). Under rapid growth conditions, plagioclase crystals develop elongate shapes and long sizes (i.e., high aspect ratios) to reduce latent heat and penetrate the diffusive boundary layer saturated by rate-limiting components for the crystal growth (i.e., Kirkpatrick and Kuo, 1981; Kohut and Nielsen, 2004). This corresponds to a morphological instability between plagioclase face and the diffusive boundary layer, such that plagioclase crystals grow in the direction of more relaxed melt regions. Conversely, at low supersaturation, the growth rate of plagioclase is slow and incompatible components in the melt are efficiently rejected away from the advancing crystal surface (Watson and Muller, 2009). As a result, the interface melt may easily supply chemical nutrients compatible with the lattice site of plagioclase crystals that develop planar faces and short sizes (i.e., low aspect ratios; Kirkpatrick and Kuo, 1981; Kohut and Nielsen, 2004).

Following the same approach of Moschini et al. (2021), a weighted least square regression analysis is performed on data plotted in Fig. 2a, by giving to each *lnG* value the proper amount of influence over the estimate that corresponds to a weight of 30% according to segmentation process and error propagation analysis. Logarithmic data are susceptible to uncertainties associated with the linearization of the model (i.e., heteroskedasticity; Hair et al., 1995). Therefore, error minimization by incorporating weights into the fitting criterion is extremely important to downweight outliers and reduce their impact on the regression model. Growth rate calculations may also suffer from lack of accurate knowledge concerning the crystallization time. Measuring the time lag caused by delayed crystal appearance due to early supersaturation effects is not a trivial task. The same issue is

encountered in determining the exact time at which the crystal growth ceases, and chemical equilibrium is established at the crystal-melt interface. Bearing in mind these limitations, potentially aberrant data are filtered and not used for regression analysis. We cautionary consider as spurious *lnG* values those returning estimates exceeding 95% confidence interval (2σ) of the model error. The algebraic form of the weighted least square linear regression equation is:

$$\ln G = \beta_0 + \beta_1 \ln t \quad (3)$$

The best regression constants solving Eq. (3) for our experiments are β_0 = -1.567 and β_1 = -1.228, with R^2 = 0.986, *SEE* = ±0.330, and *AAD* = ±0.268 (Fig. 2a).

By considering both plagioclase growth rates from this study and those from literature reported in Supplementary Material 4, we can also derive a global model with β_0 = -2.265 and β_1 = -1.097, with R^2 = 0.864, *SEE* = ±0.938, and *AAD* = ±0.729 (Fig. 2b). For this global data set, values of *Pearson's r* from multivariate regression analysis confirm that *lnG* is prevalently controlled by *lnt* (0.80) and subordinately by ΔT (0.15). Weak correlations are still found between *lnG* and *T* (0.03), H_2O^{melt} (0.07), and NBO/T^{melt} (0.06). The magnitude of *lnG* results primarily influenced by *lnt* (72%) and secondarily by ΔT (13%). The influence related to *T* (3%), H_2O^{melt} (6%), and NBO/T^{melt} (5%) is minimal.

Model robustness and solidity are verified by perturbing Eq. (3) via Monte Carlo simulations over a normal distribution with the mean centered on ln*G* and deviation close to *SEE* (Hair et al., 1995). After generating 1000 sets of hypothetical regression coefficients, probability density functions are used to analyze the Gaussian distribution of perturbed β_0 and β_1. For plagioclase growth rates from this study, the uncertainties of perturbed β_0 and β_1 are ±0.184 and ±0.018, respectively. For the global model, ~95% of perturbed β_0 and β_1 have uncertainties of ±0.392 and ±0.037, respectively. These quantities compare well with those derived by weighted least square regression

analysis and their propagation in Eq. (3) produces perturbed model errors (ε) with mean values close to 25%.

3.4 Estimating eruptive timescales at Stromboli and Mt. Etna

Stromboli is a steady-state volcano whose eruptive activity is related to the dynamics of an open-conduit system undergoing continuous recharge, crystallization, and eruption (Francalanci et al., 2005, 2012; Petrone et al., 2018). The normal eruptive activity at Stromboli consists of ejections of high-porphyritic (*Hp*) black scoria and lapilli during mild "Strombolian" explosions, which are interrupted by more violent explosions, major explosions and paroxysms, producing a characteristic low-porphyritic (*Lp*) light pumice (Metrich et al., 2010; Francalanci et al., 2012). Major explosions consist of single and/or multiple blasts with intervals of few seconds to minutes that do not affect the settled areas, whereas paroxysms refer to higher volumes of erupted juvenile material threatening the inhabitants and villages (Barberi et al., 1993). The Present-day activity (< 1.2 kyr) of Stromboli is fed by a vertically-extended mush column, which is periodically refilled with mafic magmas rising from the deeper *Lp*-reservoir ($P \approx$ 190-260 MPa, $T \geq$ 1150 °C, and H_2O^{melt} up to ~3.8 wt.%) and mixing with more differentiated magmas stored in the shallower *Hp*-reservoir ($P \approx$ 50-100 MPa, $T <$ 1150, and H_2O^{melt} up to ~2.4 wt.%) (Landi et al., 2004, 2006; Metrich et al., 2010; Di Stefano et al., 2020).

Most of plagioclase crystallization is related to extensive magma degassing within the uppermost segment of mush column. Syn-eruptive *Lp-Hp* magma mixing and mush cannibalism are also recorded by the marked chemical heterogeneities and complex textures of plagioclase phenocrysts, showing corroded cores, coarsely sieved mantles, overgrowth rims, and patchy to oscillatory zonations (Francalanci et al., 2005, 2012; Landi et al., 2004, 2006). In response to open-system crystallization conditions and mush remobilization phenomena, plagioclase corroded cores are in Sr isotopic disequilibrium with their host magmas (i.e., bulk rock analyses). Disequilibrium is caused by transport of antecrysts into shallower *Hp*-reservoirs by recurrent arrival of deeper *Lp*-magmas passing through the mush column (Francalanci et al., 2005, 2012; Landi et al., 2004, 2006).

With the purpose of modeling eruption timescales at Stromboli, we focus on scoria clasts from three paroxysms (05/04/2003, 15/03/2007, and 03/07/2019) and one major eruption (01/11/2017). A representative BSE photomicrograph of 05/04/2003 sample obtained at low magnification shows that scoria clasts are dominated by abundant crystallization of plagioclase (Supplementary Material 5). Zoom-in views highlight that plagioclase populations with $L > 0.3$ mm are characterized by strong disequilibrium features as described above, whereas plagioclase populations with $L \leq 0.3$ mm are texturally homogeneous (Supplementary Material 5). This observation is in close agreement with the CSD study by Fornaciai et al. (2009) outlining that changes in slopes and intercepts derived for large plagioclase crystals are caused by cyclic dissolution/recrystallization processes during magma mixing dynamics. Conversely, steeper CSD gradients attained at smaller crystal sizes identify plagioclase crystals that do not show resorption features because of growth via syn-eruptive magma depressurization and degassing. Regression analysis of $N(L)$ against L data for these small crystals returns values of m and N_0 varying from -16.08 to -17.45 and from 4.73 to 8.16, respectively (Supplementary Material 5). The timescale of crystal growth is quantified by taking into consideration the dynamic temporal evolution of G with t, as described in Eq. (3). Following Moschini et al. (2021), we substitute Eq. (3) into the slope $m = 1 / (G \times \tau)$ of CSD Eq. (1) and then rearrange the algebraic expression to isolate the crystallization time of plagioclase as:

$$G = t^{\beta_1} \exp\beta_0, \tag{4}$$

$$m = -\frac{1}{\left|t_{max}^{(\beta_1+1)} \exp\beta_0\right|}, \text{ and} \tag{5}$$

$$t = \left(-\frac{1}{m \exp\beta_0}\right)^{\left(\frac{1}{\beta_1+1}\right)} \tag{6}$$

Using regression coefficients from Eq. (3) from our experiments, we estimate crystallization times of ~5±1 (05/04/2003), ~4±1 (15/07/2007), ~5±1 (01/11/2017), and ~3±1 (03/07/2019) min. For the sake of completeness, we also test regression coefficients for the global model, which yields comparable crystallization times of ~8±2 (05/04/2003), ~5±1 (15/07/2007), ~7±2 (01/11/2017), and ~3±1 (03/07/2019) min. Irrespective of the equation used, we stress that estimates in the order of minutes corroborates data from numerical simulations on syn-eruptive disequilibrium plagioclase crystallization in basaltic magma ascent dynamics at Stromboli, Mt. Etna, and Kilauea volcanos (La Spina et al., 2016). Results from one-dimensional multiphase multi-component steady-state modeling indicate that, after magma depressurization, equilibrium plagioclase content is achieved in ~100 min. However, fast disequilibrium ascent of magma within the conduit causes rapid growth of plagioclase microlites over a timescale of 2 min when the gas exsolution timescale is < 3 min (La Spina et al., 2016). Considering that strong degassing-induced crystallization at Stromboli is expected to take place in the last 2 km of the conduit (cf. Di Stefano et al., 2020), we calculate magma ascent rates of ~7-11 m s^{-1} (regression of mafic data set) and ~4-10 m s^{-1} (regression of overall data set) for paroxysmal and major eruptions, in agreement with previous estimates for mafic alkaline magmas at Stromboli, Mt. Etna, and Kilauea (~1-23 m s^{-1}; La Spina et al., 2016, 2021; Polacci et al., 2019; Moschini et al., 2021) or more silicic explosive eruptions worldwide (~0.5–50 m s^{-1}; Cassidy et al., 2018).

As a further application of growth rate data from this study, we also consider large plagioclase phenocrysts (L > 0.5 mm) from lava flows at Mt. Etna, the largest sub-aerial volcano in Europe and one of the most active on Earth (Armienti et al., 1994, 1997). Over the last 300 kyr, Mt. Etna produced abundant trachybasalt to basaltic trachyandesite and trachyandesite lavas, mainly characterized by the ubiquitous occurrence of clinopyroxene, plagioclase and titanomagnetite (Mollo et al., 2015a). The plumbing system has a multifaceted geometry, variable in space and time, and consisting of storage zones at different depths, where primitive magmas undergo fractional crystallization, degassing, and mixing processes (Armienti et al., 2013). An open-conduit system is persistently filled

with magma feeding spectacular explosive Strombolian eruptions and lava fountains from the summit craters. Effusive flank eruptions occur as both lateral eruptions draining magma from the central conduit (Corsaro et al., 2009) and as eccentric (peripheral) eruptions bypassing the central conduit and draining magma from the deeper feeding system (Andronico et al., 2005). Petrological studies outline that intratelluric crystals generally equilibrate at $P \approx$ 100-500 MPa, $T \approx$ 1000-1200 °C, and $H_2O^{melt} \approx$ 1-3 wt.% (Métrich et al. 2004; Armienti et al. 2013; Mollo et al., 2015a, 2018).

Armienti et al. (1994) reports CSD data for plagioclase phenocrysts from lava flows outpoured over an eruptive period started on December 1991 and ended in March 1993. The eruption started from a fissure near the South East Crater and produced ~300 $\times 10^6$ m^3 of material. Plagioclase dominates the paragenesis of all porphyritic rock samples. In CSD plots, larger phenocrysts with euhedral, tabular shapes are distributed along nearly horizontal trends, identifying a population of intratelluric crystals in equilibrium under deep-seated conditions (i.e., 570-750 MPa and 1140-1160 °C; Armienti et al., 1994). Importantly, isotopic and geochemical data demonstrate that large-scale magma mixing never occurred and that 1991-1993 eruptions represents a single magma batch (Armienti et al., 1994). A similar conclusion is also reported in a companion study by Armienti et al. (1997), in which textural analysis of plagioclase is extended to the eccentric 1974 lava flow and other lavas containing centimeter-sized plagioclase phenocrysts from 1614, 1624, and 1723 subterminal and flank eruptions. By interpolating slopes (from -14 to -17 mm^{-1}) of CSD curves from Armienti et al. (1994, 1997) and plagioclase growth rates from isothermal-isobaric experiments (~10^{-7} mm s^{-1}), we obtain crystal residence times from 3 (±0.25) to 9 (±2.25) years, in accord with low degrees of undercooling (<30 °C; Orlando et al., 2008) and slow cooling rates (0.16 °C h^{-1}; Cashman, 1993) in the lowermost parts of the plumbing system, where most of the volatiles are retained into the melt and/or exsolve gradually during slow degassing (Armienti et al., 2013).

4. Plagioclase and melt compositional changes

4.1 Plagioclase cation substitutions and exchange partition coefficients

In our experiments, plagioclase saturation temperatures range from 1050 °C when H_2O^{melt} = 4.4 wt.% to 1150 °C when H_2O^{melt} = 0 wt.% (Supplementary Material 1). The compositional variation of plagioclase is displayed in Fig. 3 as a function of T and H_2O^{melt}. Appreciable linear correlations (R^2 = 0.51-0.67) are measured between plagioclase cation fractions and the experimental temperature, with fast and slow decompression data that overlap to compositions obtained isothermally at 1050 and 1100 °C. X_{Ca}^{pl} and X_{Mg}^{pl} are preferential incorporated in plagioclase with increasing T, whereas values of X_{Na}^{pl} and X_{Fe}^{pl} decrease (Fig. 3). Regression fits depicted by X_{Ca}^{pl} and X_{Na}^{pl} show opposite directions with almost identical R^2 = 0.63-0.64, as a proxy for the well-established heterovalent coupled substitution [$^{M}Na^{+}$, $^{T}Si^{4+}$] ↔ [$^{M}Ca^{2+}$, $^{T}Al^{3+}$] (Smith and Brown, 1988; Housh and Luhr, 1991). In contrast to the apparent control of T on cation incorporation, the strength of correlation between plagioclase cation fractions and H_2O^{melt} is generally weak for X_{Ca}^{pl}, X_{Na}^{pl}, and X_{Fe}^{pl} (R^2 = 0.15-0.21), with a slightly better fit for X_{Mg}^{pl} (R^2 = 0.44) (Fig. 3).

The site occupancies of Fe and Mg are particularly difficult to establish for plagioclase because these cations show heterovalent substitution (e.g., Fe^{2+} and Fe^{3+}) and/or site splitting (e.g., Mg^{2+} and Fe^{2+}) (Lindsley and Smith, 1971; Smith and Brown, 1988; Xue and Morse, 1994; Sugawara, 2001). Fe^{3+} substitutes for Al^{3+} in tetrahedral coordination as $Ca(Fe^{3+},Al^{3+})Si_2O_8$, whereas Fe^{2+} and Mg^{2+} can alternatively enter both the M- and T-sites to form $(Fe^{2+},Mg^{2+})Al_2Si_2O_8$ and $Ca(Fe^{2+},Mg^{2+})Si_3O_8$ components, respectively (Smith, 1974; Longhi et al., 1976; James and McGee, 1992; Peters et al., 1995; Sugawara, 2001). However, no more than about 10% of Fe^{2+} and Mg^{2+} substitutes in the form of $(Fe,Mg)Al_2Si_2O_8$ and both cations can be reasonably assumed as tetrahedrally coordinated (Sugawara, 2001 and references therein). Substitution mechanisms of these cations in plagioclase are strictly controlled by the compositional dependence of crystal-melt equilibrium reactions on the activities of melt components (Longhi et al., 1976; Peters et al., 1995).

According to Longhi et al. (1976), we can consider only the ideal term of these reactions by plotting mol.% of MgO and FeO (i.e., total iron as FeO from microprobe analysis) in plagioclase against those of melt oxides. The geochemical evolution of MgO and FeO in plagioclase scales with the magnitude of melt oxides (Fig. 4a), with plagioclase crystals from mafic alkaline experiments typically enriched in total iron as a result of high oxidizing equilibration conditions (see Mollo et al., 2011 for further details). Regression fits indicate that experimental partition coefficients (K) of MgO and FeO (K_{Mg} = 0.04 and K_{Fe} = 0.07) are almost identical to those determined by Longhi et al. (1976) for terrestrial basalts (K_{Mg} = 0.04 and K_{Fe} = 0.06).

Wilke and Behrens (1999) show that K_{Fe} measured between plagioclase and low-T (750-850 °C) silicic melts (SiO_2 = 62-68 wt.% and FeO_{tot} = 0.6-1.4 wt.%) increases with increasing temperature. However, as explained by Wilke and Behrens (1999), K_{Fe} is strongly controlled by the oxygen fugacity imposed to the experimental charge, thus overwhelming the effects of temperature and melt components on iron incorporation reactions. This implies that K_{Fe} is independent of temperature when most of FeO_{tot} consists of ferric iron under reducing crystallization conditions (Sato, 1989; Phinney, 1992; Aigner-Torres et al., 2007). For example, little or no variations are observed for K_{Fe} calculated by Aigner-Torres et al. (2007) at high-T (1180-1220 °C) and low-fO_2 (IW-QFM buffer) for basaltic melts (SiO_2 = 49-52 wt.% and FeO_{tot} = 8-10 wt.%). Conversely, the authors document that changing iron speciation from Fe^{2+} to Fe^{3+} in oxidized melts causes K_{Fe} to decrease with increasing T (Aigner-Torres et al., 2007), as described by the negative X_{Fe}-T trend derived for mafic alkaline melts (Fig. 3). Owing to the relative high oxidation conditions of our experiments and natural alkaline magmas at Stromboli and Mt. Etna ($fO_2 \geq$ NNO+1.5; e.g., Mollo et al., 2015a), most of total iron in the melt is ferric iron (i.e., Fe_2O_3 > 60%), as calculated by the model of Kress and Carmichael (1991). Analogously, the partitioning equations of Sugawara (2001) indicate that Fe_2O_3 accounts for ~66-78% of total iron in plagioclase. We can therefore reappraise the plagioclase-melt compositional variation displayed in Fig.4a by considering iron speciation and using

equilibrium reactions for $CaMgSi_3O_8$ and $CaFeAlSi_2O_8$ components of the same type as those reported in Peters et al. (1995):

$$CaO^{melt} + MgO^{melt} + 3SiO_2{}^{melt} = CaMgSi_3O_8{}^{pl} \quad (7)$$

$$K_{eq} = [CaMgSi_3O_8{}^{pl}] / [CaO^{melt}\ MgO^{melt}\ (SiO_2{}^{melt})^3] \quad (8)$$

$$K_{Mg} = [MgO^{pl}] / [MgO^{melt}] \propto K_{eq}\ [CaO^{melt}\ (SiO_2{}^{melt})^3], \text{ and} \quad (9)$$

$$CaO^{melt} + 0.5Fe_2O_3{}^{melt} + 0.5Al_2O_3{}^{melt} + 2SiO_2{}^{melt} = CaFeAlSi_2O_8{}^{pl} \quad (10)$$

$$K_{eq} = [CaFeAlSi_3O_8{}^{pl}] / [CaO^{melt}\ (Fe_2O_3{}^{melt})^{0.5}\ (Al_2O_3{}^{melt})^{0.5}\ (SiO_2{}^{melt})^2] \quad (11)$$

$$K_{Fe} = [Fe_2O_3{}^{pl}] / [Fe_2O_3{}^{melt}] \propto K_{eq}\ [CaO^{melt}\ (Al_2O_3{}^{melt})^{0.5}\ (SiO_2{}^{melt})^2] \quad (12)$$

To solve Eq. (9) and Eq. (12), the activity of melt components is calculated with the two-lattice melt model of Nielsen and Drake (1979) where the melt is assumed as two-independent quasi-lattices formed by network-former and network-modifier cations. These hypothetical thermodynamic components are assumed as proxies for the actual melt species as indicated by the positive linear variation of K_{Mg}^{pl} and K_{Fe}^{pl} as a function of melt oxide activities (Fig. 4b), in accord with the dominant effect of melt energetics on cation occupancies in plagioclase T-site (Peters et al., 1995).

As already reported by several authors (Longhi et al., 1976; Aigner-Torres et al., 2007; Mollo et al., 2011), there is no dependence of Fe-Mg exchange partition coefficient [$K_{Fe-Mg}^{pl-melt} = (X_{Fe}^{pl}/X_{Mg}^{pl})/\ (X_{Fe}^{melt}/X_{Mg}^{melt})$] on T and H_2O^{melt} (R^2 = 0.01-0.31), showing an almost constant value of 2.1 ± 0.4 (Fig. 5). This result closely matches with the range of 2.2 ± 0.1 calculated by Mollo et al.

(2011) for crystals formed from a trachybasalt equilibrated under anhydrous conditions at P = 500 MPa, T = 1000-1100 °C and fO_2 = NNO+1.5. The authors performed also cooling rate experiments inducing rapid plagioclase growth and formation of dendritic crystals surrounded by a diffusive melt with thickness of ~50 μm. Because of strong deviations from chemical equilibrium, $K_{Fe-Mg}^{pl-melt}$ is measured to decrease by Mollo et al. (2011) towards a disequilibrium value of 1.6 ± 0.1. Fe and Mg are incompatible with the lattice site of plagioclase and their partitioning behaviors are extremely sensitive to cation incorporation at non-equilibrium proportions during dendritic crystal growth via diffusion-controlled kinetics (Mollo et al., 2011). The lack of both dendrites and thick diffusive boundary layers in decompression experiments from this study and the constancy of $K_{Fe-Mg}^{pl-melt}$ suggest attainment of local chemical equilibrium at the interface between the advancing plagioclase surface and surrounding melt (Di Fiore et al., 2021; Lang et al., 2021). The entry of cations in plagioclase lattice site at near-equilibrium partitioning conditions is mainly due to the low viscosity of mafic melts and the enhancing effect of water on cation mobility not only under static conditions but also during decompression-driven crystallization. During disequilibrium degassing, water transfer from the melt into vapor phase is less efficient than equilibrium volatile fractionation (Bai et al., 2008). Because part of dissolved water is retained in the supersaturated melt, the transfer rate of cations at the crystal-melt interface is enhanced and the length scale of diffusion fields around decompressed acicular crystals cannot be resolved with microprobe analysis (e.g., Mollo et al., 2018).

Fig. 5 shows that the An-Ab (or Ca-Na) exchange partition coefficient ($K_{An-Ab}^{pl-melt}$ or $K_{Ca-Na}^{pl-melt}$) is strictly dependent on T (R^2 = 0.73) and there is no statistically significant correlation between $K_{An-Ab}^{pl-melt}$ and H_2O^{melt}, at least for the subset of data investigated in this study and specific to mafic alkaline magmas. This lack of correlation is apparently in contrast with the well-established increase of $K_{An-Ab}^{pl-melt}$ with increasing the amount of water dissolved in calcalkaline melts proposed by Sisson and Grove (1993). For experimental plagioclase-melt pairs obtained by equilibrating calcalkaline basalts to rhyolites under water-saturated conditions ($P \approx$ 100-500 MPa and $T \approx$ 940-1120 °C), Sisson

and Grove (1993) found a progressive increase of $K_{An-Ab}^{pl-melt}$ from ~1.7 for H_2O^{melt} ≈ 2 wt.%, ~3-4 for H_2O^{melt} ≈ 4 wt.%, and ~5.5 for H_2O^{melt} ≈ 6 wt.%. These values were obtained by regressing experimental data in the diagram An^{melt}/Ab^{melt} against An^{pl}/Ab^{pl} and forcing the fit to pass through the origin of axis. Here we extend the data set used by Sisson and Grove (1993) to calcalkaline compositions from Lange et al. (2009) and Waters and Lange (2015) obtained under both hydrous and anhydrous conditions (P ≈ 0.1-500 MPa, T ≈ 800-1235 °C, and H_2O^{melt} ≈ 0-8 wt.%) and then compare them with mafic alkaline experiments. In Fig. 6, data are grouped as calcalkaline basalts-andesites (T ≈ 1100-1235 °C and H_2O^{melt} ≈ 0-2 wt.%), calcalkaline dacites-rhyolites (T ≈ 800-1060 °C and H_2O^{melt} ≈ 2-8 wt.%), and mafic alkaline melts (T ≈ 1050-1150 °C and H_2O^{melt} ≈ 0.0-4.4 wt.%), returning $K_{An-Ab}^{pl-melt}$ of 0.8-2.1, 2.5-7.5, and 1.6-3.5, respectively. Importantly, high-T, low-H_2O^{melt} calcalkaline basalts-andesites correspond to low $K_{An-Ab}^{pl-melt}$ endmembers, whereas low-T, high-H_2O^{melt} calcalkaline dacites-rhyolites refer to high $K_{An-Ab}^{pl-melt}$ endmembers (Fig. 6). Because of interrelation between T and H_2O^{melt}, the diagram An^{melt}/Ab^{melt} against An^{pl}/Ab^{pl} cannot unequivocally discriminate and isolate the effect of temperature from that of dissolved water. While the solubility of water in the melt increases with increasing its silicic character, the onset of plagioclase crystallization takes place at lower temperatures as both liquidus and solidus curves of the binary loop for the Ab-An system are depressed by water addition. As a consequence, $K_{An-Ab}^{pl-melt}$ values obtained for mafic alkaline melts at intermediate T and H_2O^{melt} are bounded between those derived for high-T, low-H_2O^{melt} and low-T, high-H_2O^{melt} calcalkaline compositions.

In terms of An-Ab components, our experimental plagioclase crystals show An_{47-87} and Ab_{12-48} compositions (expressed in percentage). As for X_{Ca}^{pl} and X_{Na}^{pl} trends depicted in Fig. 3, An_{47-87} and Ab_{12-48} compositions are more tightly correlated with T ($^{An}R^2$ = 0.65 and $^{Ab}R^2$ = 0.64) rather than H_2O^{melt} ($^{An}R^2$ = 0.15 and $^{Ab}R^2$ = 0.14). Experimental crystals reproduce also most of natural plagioclase phenocrysts at Mt. Etna (An_{43-88} and Ab_{10-48}) and Stromboli (An_{41-90} and Ab_{8-50}), as reported in the GEOROC database (http://georoc.mpch-mainz.gwdg.de).

4.2 Tracking differentiation conditions of natural mafic alkaline melts

Residual glass compositions from our experiments are comparatively plotted in Fig. 7 against *Hp*-*Lp*-glasses and 2003-2020 bulk rocks from Stromboli, as well as historic (from 15 kyr to 1886) and recent (2001-2021) bulk rocks from Mt. Etna (data from the GEOROC database). Experimental glasses become more differentiated as the degree of crystallization increases with decreasing T and H_2O^{melt}. Slow-fast decompression experiments are also characterized by water exsolution and consequent formation of more silicic- and alkali-rich melts (Fig. 7).

For Stromboli, mafic bulk rocks and *Lp*-glasses are described by experiments carried out at $T \geq 1100$ °C and $H_2O^{melt} \geq 1.5$ wt.% (Fig. 7). These compositions are classified as high-K and shoshonitic basalts (Francalanci et al., 2013) and match with primitive, undegassed *Lp*-magmas stored at $P \approx 200$-300 MPa (~7-10 km depth for an average crustal density of 2700 kg m^{-3}; Allard et al., 2000), $T \approx 1165$-1175 °C, and $H_2O^{melt} \approx 2.0$-3.5 wt.% (Clocchiatti 1981; Metrich et al., 2010; Di Stefano et al., 2020). More evolved *Hp*-glasses and bulk rocks with shoshonitic compositions are experimentally reproduced at $T \leq 1100$ °C and $H_2O^{melt} < 1.5$ wt.% (Fig. 7). These conditions correspond to a low-P storage region at 50-100 MPa (~2-4 km depth) where *Hp*-magmas undergo strong cooling and degassing phenomena (Metrich et al., 2010; Francalanci et al., 2013; Di Stefano et al., 2020).

For Mt. Etna, experimental glasses synthetized at $T \geq 1100$ °C and $H_2O^{melt} = 2.1$-6.3 wt.% agree with geochemical modeling and melt inclusions characterization of 2001-2021 trachybasaltic eruptions (Fig. 7), which are fed by recurring inputs of fresh magmas stored at $P \geq 100$ MPa (Metrich and Rutherford, 1998; Métrich et al. 2004; Armienti et al. 2013; Giacomoni et al., 2018; Mollo et al., 2015b, 2018). Note that the plumbing system at Mt. Etna undergoes little crystallization at depth, as most of its water concentration is retained in the melt by lowering its liquidus temperature and the degree of crystallization (Perinelli et al., 2016). On the other hand, historic eruptions with basaltic trachyandesite compositions are obtained at $T < 1100$ °C and $H_2O^{melt} = 0.0$-2.8 wt.% (Fig. 7). These differentiated magmas originate by degassing-induced crystallization at very shallow depths ($P < 100$

MPa), when the degree of crystallization is higher than 20-25% owing to the enlargement of plagioclase stability field (Vetere et al., 2015). Low-*T*, low-H_2O^{melt} isothermal-isobaric experiments and slow-fast decompression experiments describe quite well this mechanism, thereby returning plagioclase-dominated phase assemblages with crystal contents variable from ~30 to ~40%.

5. Thermodynamic and statistical modeling of plagioclase-melt equilibrium

5.1 Preliminary considerations

For the simplest formula of An in plagioclase, the fusion reaction can be expressed as:

$$CaAl_2Si_2O_8^{pl} = CaAl_2Si_2O_8^{melt} \quad (13)$$

At the equilibrium, the chemical potential μ_{An} is the same in both plagioclase and melt:

$$\mu_{\mathrm{An}}^{pl} = \mu_{\mathrm{An}}^{melt}, \quad (14)$$

$$\mu_{\mathrm{An}}^{pl} = \mu_{\mathrm{An}}^{o\,pl} + RTln\left(a_{\mathrm{An}}^{pl}\right), \quad (15)$$

$$\mu_{\mathrm{An}}^{melt} = \mu_{\mathrm{An}}^{o\,melt} + RTln\left(a_{\mathrm{An}}^{melt}\right), \quad (16)$$

$$\mu_{\mathrm{An}}^{o\,pl} + RTln\left(a_{\mathrm{An}}^{pl}\right) = \mu_{\mathrm{An}}^{o\,melt} + RTln\left(a_{\mathrm{An}}^{melt}\right), \text{ and} \quad (17)$$

$$\mu_{\mathrm{An}}^{pl} - \mu_{\mathrm{An}}^{melt} = \Delta\mu_{An} = 0 = \Delta G_{An}^{0}(P,T) + RTln\left(\frac{a_{\mathrm{An}}^{melt}}{a_{\mathrm{An}}^{pl}}\right) \quad (18)$$

For a standard-state of pure An at the pressure and temperature of interest, $\Delta G^{o}_{An}(P,T)$ is referred to the standard Gibbs free energy of reaction (Glazner, 1984; Lange et al., 2009; Waters and Lange, 2015; Namur et al., 2012; Putirka, 2017). $\Delta G^{o}_{An}(P,T)$ is expressed in kJ mol^{-1} and changes as a function of both pressure (P in GPa) and absolute temperature (T in K) but is independent of plagioclase and melt compositions. The activity term a_{An} corresponds to the product of the molar fraction X_{An} and activity coefficient γ_{An}. For an ideal solution model, γ_{An} = 1 and $a_{\mathrm{An}} = X_{\mathrm{An}}$. R is the gas constant in J K^{-1} mol^{-1}. Taking into account the equilibrium constant K^{eq}_{An} of the fusion reaction of An, Eq. (18) can be rewritten as:

$$\frac{\Delta G^{o}_{An}(P,T)}{RT} = ln\left(K^{eq}_{\mathrm{An}}\right) = \ln\left(a^{pl}_{\mathrm{An}}\right) - \ln\left(a^{melt}_{\mathrm{An}}\right) \quad (19)$$

The Gibbs free energy change from Eq. (19) has the thermodynamic form:

$$\Delta G^{o}_{An}(P,T) = \Delta H^{o}_{An}(T) - T\Delta S^{o}_{An}(T) + \int_{1}^{P} \Delta V^{o}_{T\,An}(P)dP \quad (20)$$

where $\Delta H^{o}_{An}(T)$ and $\Delta S^{o}_{An}(T)$ are the standard state change in molar enthalpy and entropy, respectively, for the pure An in plagioclase and melt phases. $\Delta V^{o}_{T\,An}(P)$ is the change in molar volume as a function of pressure (Glazner, 1984; Lange et al., 2009; Waters and Lange, 2015; Namur et al., 2012; Putirka, 2017). This thermodynamic quantity is calculated at the temperature of An reaction by assuming an initial pressure of 1 bar (= 0.0001 GPa).

Along the melting curve of pure An, the equilibrium constant K^{eq}_{An} of Eq. (13) is close to 1 as both plagioclase and melt phases are pure. $\Delta G^{fusion}_{An}(T_m) = \Delta H^{fusion}_{An}(T_m) - T\Delta S^{fusion}_{An}(T_m) = 0$ and $\Delta S^{fusion}_{An}(T_m) = \left[\Delta H^{fusion}_{An}(T_m)\right]/T_m$ at the melting temperature T_m of 1 bar pure phases. The thermodynamic quantities governing the fusion reaction of An at the P-T of interest are reappraised as:

$$\Delta G_{An}^{fusion}(P,T) = \Delta H_{An}^{fusion}(T) + \Delta S_{An}^{fusion}(T) + \Delta V_{T\,An}^{fusion}(P) \quad (21)$$

$$\Delta H_{An}^{fusion}(T) = \left[\Delta H_{An}^{fusion}(T_m) + \int_{Tm}^{T} \Delta C_{p\,An}\, dT\right] \quad (22)$$

$$\Delta S_{An}^{fusion}(T) = \left[\frac{\Delta H_{An}^{fusion}(T_m)}{T_m} + \int_{Tm}^{T} \left(\frac{\Delta C_{p\,An}}{T}\right) dT\right], \text{ and} \quad (23)$$

$$\Delta V_{T\,An}^{fusion}(P) = V_{T\,An}^{melt}(P) - V_{T\,An}^{pl}(P) \quad (24)$$

where $\Delta C_{p\,An}$ is the difference in isobaric heat capacity between plagioclase and melt. $C_{p\,An}^{melt}$ is assumed to be constant over the temperature range of interest, whereas $C_{p\,An}^{pl}$ is approximated to a polynomial function of *T*, in agreement with Glazner (1984).

The same considerations reported above can be extended to pure Ab component and the An-Ab exchange reaction between plagioclase and melt:

$$CaAl_2Si_2O_8^{pl} + NaAlSi_3O_8^{melt} = CaAl_2Si_2O_8^{melt} + NaAlSi_3O_8^{pl} \quad (25)$$

Eq. (19) can be rewritten as:

$$\frac{\Delta G_{An}^{o}(P,T) - \Delta G_{Ab}^{o}(P,T)}{RT} = \frac{\Delta G_{An-Ab}^{o}(P,T)}{RT} = ln\left(K_{\mathrm{An-Ab}}^{eq}\right) = \ln\left(\frac{a_{\mathrm{An}}^{pl}}{a_{\mathrm{Ab}}^{pl}}\right) - \ln\left(\frac{a_{\mathrm{An}}^{melt}}{a_{\mathrm{Ab}}^{melt}}\right) \quad (26)$$

The difference between the Gibbs free energies of plagioclase and melt components in equilibrium at the same *P*-*T* conditions is:

$$\Delta G^{o}_{An-Ab}(P,T) = \Delta H^{o}_{An-Ab}(T) - T\Delta S^{o}_{An-Ab}(T) + \int_1^P \Delta V^{o}_{T\,An-Ab}(P)dP =$$

$$\left[\Delta H^{o}_{An-Ab}(T_m) + \int_{Tm}^{T} \Delta C_{p\,An-Ab}\,dT\right] - T\left[\frac{\Delta H^{o}_{An-Ab}(T_m)}{Tm} + \int_{Tm}^{T}\left(\frac{\Delta C_{p\,An-Ab}}{T}\right)dT\right] +$$

$$\int_1^P \Delta V^{o}_{T\,An-Ab}(P)dP \qquad (27)$$

where $\Delta H^{o}_{An-Ab}(T)$, $\Delta S^{o}_{An-Ab}(T)$, and $\Delta V^{o}_{T\,An-Ab}$ correspond to the difference between the standard state enthalpy, entropy, and volume of fusion of pure An and Ab components, respectively. Eq. (27) is solved by interpolating different thermochemical data from literature (i.e., Table 1 from Glazner, 1984, Table 1 from Lange et al., 2009, Table 1 from Waters and Lange, 2015, and Table 2 from Namur et al., 2012; Supplementary Material 6). Permutation of these data produces an almost negligible variation for $\Delta G^{o}_{An-Ab}(T)$ as a function of *T* that never exceeds ~6%. Ab and An melting curves resulting from Gibbs free energies of pure components substantially overlap with those reported in previous works (i.e., Figure 5 in Lange et al., 2009 and Figure 3 in Namur et al., 2012) and for this reason are not presented here. At the investigated *P*-*T* conditions, we calculate that Eq. (21) for pure An and Ab components returns $\Delta G^{o}_{An-Ab}(P,T)$ from 25.9 to 28.4 kJ mol^{-1}, $\Delta G^{o}_{An-Ab}(T)$ from 28.6 to 27.8 kJ mol^{-1}, and $\Delta G^{o}_{An-Ab}(P)$ from -0.18 to -1.88 kJ mol^{-1}. Notably, within the *P* range of 30-300 MPa, the energetic contribution of $\int_1^P \Delta V^{o}_{T\,An-Ab}(P)dP$ leads to the plot of $\Delta G^{o}_{An-Ab}(T)/RT$ against $\Delta G^{o}_{An-Ab}(P,T)/RT$ which shows a maximum deviation of ~8% from the one-to-one regression line (Supplementary Material 6). Because $\Delta G^{o}_{An-Ab}(T)$ >> $\Delta G^{o}_{An-Ab}(P)$ and $\Delta G^{o}_{An-Ab}(P,T) \approx \Delta G^{o}_{An-Ab}(T)$, the An-Ab exchange reaction is weakly sensitive to pressure changes during plagioclase saturation at crustal depths (cf. Lange et al., 2009). It is therefore not surprising that the uncertainty of plagioclase-based barometers is much greater than the dynamics of magma transport within volcanic conduits, corresponding to ±380 MPa (i.e., a depth uncertainty of ±17 km presuming a continental crust density of 2.7 g cm^{-3}) for barometers calibrated by global regression analysis of 727 literature data (see Figure 5 in the review study of Putirka, 2008).

5.2 Anorthite-albite melt activities and the role of H_2O^{melt}

The solution of Eq. (26) requires that activity-composition relations of An and Ab in both plagioclase and melt phases are calculated by considering the ideal and non-ideal parts of $ln\left(K_{\mathrm{An-Ab}}^{eq}\right)$:

$$ln\left(K_{\mathrm{An-Ab}}^{eq}\right) = \left[\ln\left(\frac{X_{\mathrm{An}}^{pl}}{X_{\mathrm{Ab}}^{pl}}\right)^{ideal} + \ln\left(\frac{\gamma_{\mathrm{An}}^{pl}}{\gamma_{\mathrm{Ab}}^{pl}}\right)^{non-ideal}\right] - \left[\ln\left(\frac{X_{\mathrm{An}}^{melt}}{X_{\mathrm{Ab}}^{melt}}\right)^{ideal} + \ln\left(\frac{\gamma_{\mathrm{An}}^{melt}}{\gamma_{\mathrm{Ab}}^{melt}}\right)^{non-ideal}\right] \quad (28)$$

where $K_{\mathrm{An-Ab}}^{ideal} = \left(\frac{X_{\mathrm{An}}^{pl} X_{\mathrm{Ab}}^{melt}}{X_{\mathrm{Ab}}^{pl} X_{\mathrm{An}}^{melt}}\right)^{ideal}$ and $K_{\mathrm{An-Ab}}^{non-ideal} = \left(\frac{\gamma_{\mathrm{An}}^{pl}\gamma_{\mathrm{Ab}}^{melt}}{\gamma_{\mathrm{Ab}}^{pl}\gamma_{\mathrm{An}}^{melt}}\right)^{non-ideal}$. The non-ideal part of $K_{\mathrm{An-Ab}}^{eq}$ represents the excess Gibbs free energy (ΔG_{ex}) that incorporates the deviation from ideality for the solution of An and Ab components in both phases (Putirka, 2017).

The solid solution of plagioclase is not ideal due to the occurrence of two structural states and different degrees of Si-Al ordering in tetrahedral coordination (Carpenter, 1988). However, at magmatic temperatures, activity-relation models for plagioclase approximate the condition where An-Ab solid solution can be considered to mix ideally on one site per 8-oxygen formula unit. This implies that $a_{\mathrm{An}}^{pl} \cong \left(X_{\mathrm{An}}^{pl}\right)^{ideal}$ and $a_{\mathrm{Ab}}^{pl} \cong \left(X_{\mathrm{Ab}}^{pl}\right)^{ideal}$ with quantities that never differ by more than 10%, as documented by Glazner (1984) and Namur et al. (2012).

For the melt counterpart, ideal interactions of oxide components are calculated according to Carmichael et al. (1977):

$$\left(X_{\mathrm{An}}^{melt}\right)^{ideal} = 64.000\left(X_{CaO}^{melt}\right)\left(X_{Al2O3}^{melt}\right)\left(X_{SiO2}^{melt}\right)^2 \quad (29)$$

$$\left(X_{\mathrm{Ab}}^{melt}\right)^{ideal} = 18.963\left(X_{Na2O}^{melt}\right)^{0.5}\left(X_{Al2O3}^{melt}\right)^{0.5}\left(X_{SiO2}^{melt}\right)^3 \quad (30)$$

An early attempt to develop empirical equations for $\gamma_{\mathrm{An}}^{melt}$ and $\gamma_{\mathrm{Ab}}^{melt}$ as a function of oxide components in the melt is reported in Glazner (1984) using 101 experimental plagioclase-melt pairs from basaltic to dacitic compositions equilibrated at P = 0.1-1500 MPa, $T \approx$ 1060-1400 °C, and $f\mathrm{O}_2$ ≤ QFM under anhydrous conditions. The final expressions for the activity coefficients (see Tables 3 and 4 in Glazner, 1984) are similar to a Margules power-series expansion for excess Gibbs free energy $\Delta G_{ex} = f(W)$, where W is the Margules interaction parameter. It must be noted that this type of equation does not provide a direct measure of the activity of oxide component, as the estimated quantity W is proportional but not identical to the true melt activity. Hence the final form of $\Delta G_{ex} = f(W)$ can be generally defined as activity model. Application to our experiments (Fig. 8a,b) returns modest regression statistics for the coefficient of determination ($R^2_{\mathrm{An}} = 0.65$ and $R^2_{\mathrm{Ab}} = 0.52$) and standard error of estimate ($SEE_{\mathrm{An}} = 0.22$ and $SEE_{\mathrm{Ab}} = 0.21$). The low accuracy of the polynomial function is essentially due to the absence of mafic alkaline compositions in the calibration data set of Glazner (1984), which includes only melts with tholeiitic and calc-alkaline affinities. The important aspect to keep in mind is that Margules interaction parameters are defined from experimental data on coexisting plagioclase-melt pairs. Once calibrated, these interaction parameters describe in first approximation ΔG_{ex} of a multicomponent system bounded by the *P-T-X* conditions of the calibration data (Ghiorso et al., 1983).

The most recent model of Namur et al. (2012) is based on a large data set of 530 plagioclase-melt pairs obtained for picrobasaltic to rhyolitic compositions equilibrated under anhydrous conditions at P = 0.1 MPa, $T \approx$ 1000-1350 °C, and $f\mathrm{O}_2$ ≤ QFM. The calibration data set includes alkaline mafic compositions, such as alkaline basalts, tephrites, trachybasalts, basaltic trachyandesites, and trachyandesites. Through the regression analysis of anhydrous melt components expressed as cation proportions on an 8-oxygen basis, Namur et al. (2012) obtains two empirical models for the estimate of $\ln\left(a_{\mathrm{An}}^{melt}\right)$ and X_{An}^{pl} [i.e., Eq. (28) and Eq. (31), respectively, in Namur et al., 2012]. An additional anhydrous model for calculating X_{An}^{pl} is specific to mafic–ultramafic melts

and includes a subset of 298 melt compositions [i.e., Eq. (33) in Namur et al. (2012)]. Although all these models were derived on an anhydrous basis, we found successful application to hydrous mafic alkaline melt compositions [$^{\text{Eq. (28)}}R^2$ = 0.93, $^{\text{Eq. (31)}}R^2$ = 0.94, and $^{\text{Eq. (33)}}R^2$ = 0.91, and $^{\text{Eq. (28)}}$SEE = 0.10, $^{\text{Eq. (31)}}$SEE = 0.04, and $^{\text{Eq. (33)}}$SEE = 0.04; Fig. 8c,d]. In principle, the effect of dissolved water is to decrease the activity of silica in the melt and the saturation surface of plagioclase (Ghiorso et al., 1983). However, for low to moderate amounts of dissolved water in the melt (i.e., $H_2O^{melt} \approx$ 0.0-4.4 wt.%; Supplementary Materials 1 and 2), the magnitude of this effect is overwhelmingly dominated by the variation of anhydrous melt components as a function of *T*, giving reason for the very good regression statistics of the anhydrous models proposed by Namur et al. (2012) (Fig. 8c,d).

The composition-related non-ideality of multicomponent silicate melt can be thermodynamically modeled using a symmetric regular solution type equation (Nicholls, 1980; Ghiorso and Carmichael, 1980; Ghiorso et al., 1983). Among the numerous models from the literature to calculate the activity coefficient of a component as a function of *W* in a multicomponent solution, we adopt the expression (Ghiorso and Carmichael, 1980):

$$RTln\gamma_k^{melt} = \sum_{i=1}^{n} W_{ik}X_i^2 + \sum_{i=2}^{n} X_i \sum_{j=1}^{i-1}(W_{ik} + W_{kj} - W_{ij})X_j \;;\; i,j \neq k \qquad (31)$$

Following Nicholls (1980), we choose an algebraically simple form for calculating the effect of one melt component on another by expressing oxides as mole fractions and using these quantities to represent melt composition. Glazner (1984) emphasizes that oxide mole fractions can be used to describe melt composition without further manipulations, as they represent the simplest independently variable components in the melt. Values of γ_k^{melt} are calculated for the appropriate oxide component of the melt through experimental compositions from this study, whereas the binary interaction coefficient *W* is assumed as a constant independent of the *P*-*T*-*X* conditions. The rationale behind this choice is that Eq. (26) was originally designed for olivine- and plagioclase-melt equilibria in pressure-temperature regions typical of basaltic systems (Ghiorso and Carmichael, 1980). All

mixing properties of oxide components are determined on an anhydrous basis and then employed to estimate the partial molar free energies of An and Ab. The partial molar excess Gibbs free energies predicted by Eq. (26) are also interpreted by Ghiorso and Carmichael (1980) as a potential thermometer for plagioclase in equilibrium with both anhydrous and hydrous melts.

To obtain a thermodynamic description for the activity coefficients of An and Ab components in the melt with Eq. (31), we derive values of γ_{An}^{melt} and γ_{Ab}^{melt} by considering the stoichiometric proportions of $CaAl_2Si_2O_8$ and $NaAlSi_3O_8$ as (Nicholls, 1980):

$$CaO + Al_2O_3 + 2SiO_2 = CaAl_2Si_2O_8, \text{ and} \quad (32)$$

$$0.5Na_2O + 0.5Al_2O_3 + 3SiO_2 = NaAlSi_3O_8 \quad (33)$$

Owing to the very poor correlation between H_2O^{melt} and plagioclase-melt components in mafic alkaline systems (Figs. 4 and 6), we assume for the moment that the effect of water solution does not substantially impact the melt configurational excess energy of mixing (i.e., nearly ideal solution model). Recalling that $a_{\text{An or Ab}}^{melt} = X_{\text{An or Ab}}^{melt}\gamma_{\text{An or Ab}}^{melt}$, Eq. (19) is rearranged as:

$$\ln\left(a_{\text{An or Ab}}^{melt}\right)^{measured} = \ln\left(a_{\text{An or Ab}}^{pl}\right) - \frac{\Delta G_{An\ or\ Ab}^{o}(P,T)}{RT} \quad (34)$$

Margules interaction parameters of Eq. (31) are calculated through a stepwise linear least square regression of experimental data from this study, which is the same procedure reported in Kress and Carmichael (1988). Activity coefficients from Eq. (32) ($\gamma_{An}^{melt} = \gamma_{CaO}^{melt} + \gamma_{Al2O3}^{melt} + 2\gamma_{SiO2}^{melt}$) and Eq. (33) ($\gamma_{Ab}^{melt} = 0.5\gamma_{Na2O}^{melt} + 0.5\gamma_{Al2O3}^{melt} + 3\gamma_{SiO2}^{melt}$) are then used to determine $\ln\left(a_{\text{An}}^{melt}\right)^{predicted}$ and $\ln\left(a_{\text{Ab}}^{melt}\right)^{predicted}$, respectively. The best estimates of the model parameters and the goodness of the

calculation are quantitatively evaluated by minimization of the Pearson's chi-square statistic (Harris and Kanji, 1983):

$$\chi_p^2 = \sum_{i=1}^{n} \frac{\left[\ln\left(a_{\text{Ab or An}}^{melt}\right)^{measured} - \ln\left(a_{\text{Ab or An}}^{melt}\right)^{predicted}\right]}{\ln\left(a_{\text{Ab or An}}^{melt}\right)^{measured}} \quad (35)$$

Multivariate analysis is also performed to prevent model instability caused by data overfitting and/or multicollinearity. All values of W for γ_{An}^{melt} and γ_{Ab}^{melt} are reported in Supplementary Material 6, in which binary interaction parameters identified as statistically insignificant predictors are set to zero. Fig. 9a shows alignment between measured and predicted An and Ab activities in the melt [i.e., $\ln\left(a_{\text{An or Ab}}^{melt}\right)^{measured}$ against $\ln\left(a_{\text{An or Ab}}^{melt}\right)^{predicted}$], with fairly good regression statistics of $R_{aAn}^2 = 0.93$, $R_{aAb}^2 = 0.93$, $SEE_{aAn} = 0.07$, and $SEE_{aAb} = 0.08$.

The effect of dissolved water on the activity coefficient calculation is tested in relation to the dissociation reaction of water in the melt (Stolper, 1982):

$$H_2O_{\text{molecular}} + O^o = 2OH^- \quad (36)$$

where $H_2O_{\text{molecular}}$, O^o , and OH^- refers to the molecular water, bridging oxygens, and OH^- group attached to a silicate polymer. Since liquidus temperature is a nonlinear function of water concentration, complex activity-composition relations are generally determined for hydrous silicate melts (e.g., Burnham, 1975). Margules interaction parameters are taken into account for describing the non-ideality of water dissolution in the melt by incorporating into Eq. (26) the thermodynamic expression:

$$W_{H2O}X_{H2O} + W_{H2O^2}X_{H2O}^2 + W_{H2O^{0.5}}X_{H2O}^{0.5} \quad (37)$$

where $W_{H2O}X_{H2O}$ represents the total amount of water dissolved in the melt, $W_{H2O^2}X_{H2O}^2$ refers to $H_2O_{molecular}$, and $W_{H2O^{0.5}}X_{H2O}^{0.5}$is a proxy for OH^- (see Ueki et al., 2020 for a more comprehensive description of water-related terms). Results from thermodynamic calculations are reported in Supplementary Material 6. However, Fig. 9b shows that the speciation of water does not offer any improvement in the ability prediction of An and Ab activities in the melt ($R_{aAn}^2 = 0.93$, $R_{aAb}^2 = 0.92$, $SEE_{aAn} = 0.08$, and $SEE_{aAb} = 0.08$), thereby emphasizing the subordinate role of water on plagioclase-melt equilibria at the experimental conditions investigated here (compare Figs. 3, 5, and 8c,d).

Thermodynamic calculations are also verified by multivariate descriptive statistics derived for the parameters: 1) H_2O^{melt}, 2) T, 3) plagioclase components [i.e., $\ln(X_{An}^{pl})$ and $\ln(X_{Ab}^{pl})$], 4) melt components [i.e., $\ln(X_i^{melt})$ and related cross-product terms as $\ln(X_i^{melt}X_i^{melt})$, where i is the cations of interest], 5) plagioclase-melt partition and exchange partition coefficients [i.e., $\ln(K_{An}^{pl-melt})$, $\ln(K_{Ab}^{pl-melt})$, and $\ln(Kd_{An-Ab}^{pl-melt})$], and 6) plagioclase-melt equilibrium constants [i.e., $\ln(K_{An}^{eq})$, $\ln(K_{Ab}^{eq})$, and $\ln(K_{An-Ab}^{eq})$]. The resulting correlation matrix is reported in Supplementary Material 7. Extremely high *p-values* are obtained for T (0.71), $\ln(K_{An}^{pl-melt})$ (0.71), $\ln(K_{An-Ab}^{pl-melt})$ (0.39), $\ln(K_{An}^{eq})$ (0.70), and $\ln(K_{Ab}^{eq})$ (0.70), as these parameters are not statistically significant for the description of H_2O^{melt}. Also, the absolute value of *Pearson's r* does not satisfy the statistical threshold of 0.60 for $\ln(K_{Ab}^{pl-melt})$ (0.24), $\ln(K_{An-Ab}^{eq})$ (0.43), $\ln(X_{An}^{pl})$ (0.39), and $\ln(X_{Ab}^{pl})$ (0.38). Multivariate analysis confirms the weak correlation between H_2O^{melt} and $Kd_{An-Ab}^{pl-melt}$ (Fig. 5), attesting the negligible effect of dissolved water on An and Ab melt activities (Figs. 8c,d and 9a,b). By regressing H_2O^{melt} against the best predictors (i.e., *p-values* < 0.05 and *Pearson's r* > 0.60; Supplementary Material 7) and testing for the absence of multicollinearity (*VIF* < 10), we cannot derive any predictive model performing better than plagioclase-based hygrometers published in literature that comparatively return a conservative uncertainty nearly close to ~1.1 wt.%. In particular, Eq. (H) (uncertainty ±1.1 wt.%

H_2O^{melt}) from Putirka (2005), Eq. (25b) (uncertainty ±1.1 wt.% H_2O^{melt}) from Putirka (2008), Eq. (25) (uncertainty ±0.32 wt.% H_2O^{melt}) from Lange et al., (2009), and Eq. (14) (uncertainty ±0.35 wt.% H_2O^{melt}) from Waters and Lange (2015) perform moderately well with the mafic alkaline data set, yielding $^{\text{Eq. (H)}}$SEE = 1.2 wt.%, $^{\text{Eq. (25b)}}$SEE = 1.1 wt.%, $^{\text{Eq. (25)}}$SEE = 1.1 wt.%, and $^{\text{Eq. (14)}}$SEE = 1.0 wt.%, respectively (Supplementary Material 7).

5.3 Plagioclase-based thermometry

For the purpose of modeling plagioclase crystallization conditions, activities of An and Ab in the melt are parameterized in a simpler and more tractable regression form, which includes first-order and second-order product terms for *n* oxide components in the melt (cf. Glazner, 1984; Namur et al., 2012; Putirka, 2017):

$$\ln\left(a_{\text{An or Ab}}^{melt}\right)^{measured} = f\left(\sum_{i=1}^{n} X_i + X_i \sum_{i=1}^{n} X_i\right) \tag{38}$$

Correlation matrices for these activity terms are reported in Supplementary Material 8 and weighted multiple linear regression analysis returns:

$$\begin{aligned}\ln\left(a_{\text{An}}^{melt}\right) = {} & -3.67(\pm0.75) + 0.72(\pm0.30)X_{Si} + 258.51(\pm67.71)X_{Ti} - 13.21(\pm7.38)X_{Fe} \\ & - 65.02(\pm6.13)X_{Mg} + 32.61(\pm1.75)X_{Ca} - 2864.94(\pm910.40)X_{Ti}X_{Fe} \\ & + 75.17(\pm14.52)X_{Al}X_{Fe} + 57.57(\pm18.51)X_{Al}X_{Mg} + 45.95(\pm5.43)X_{Fe}X_{Na} \\ & + 204.61(\pm47.20)X_{Mg}^2 - 88.81(\pm9.35)X_{Ca}^2, \text{ and}\end{aligned} \tag{39}$$

$$\begin{aligned}\ln\left(a_{\text{Ab}}^{melt}\right) = {} & -2.74(\pm0.16) + 10.31(\pm5.50)X_{Mg} + 8.85(\pm1.41)X_{Ca} + 5.06(\pm2.69)X_{Na} \\ & + 322.61(\pm187.37)X_{Ti}X_{Mg} + 30.47(\pm4.55)X_{Al}X_{Ca} - 37.24(\pm9.50)X_{Fe}X_{Na} \\ & - 146.32(\pm41.84)X_{Mg}^2 - 34.66(\pm8.51)X_{Ca}^2 - 38.58(\pm17.90)X_{Na}^2\end{aligned} \tag{40}$$

The very good regression statistics derived for Eq. (39) ($R^2_{aAn} = 0.99$) and Eq. (40) ($R^2_{aAb} = 0.99$) reflect the high accuracy of the models ($SEE_{aAn} = 0.004$ and $SEE_{aAb} = 0.003$). Although several filters are used to prevent data overfitting and multicollinearity, regression statistics derived for Eq. (39) and Eq. (40) are slightly better than those obtained from the solution of Eq. (31) using Margules interaction parameters. This is confirmed by thermodynamic calculations performed by Putirka (2017) on An and Ab activity composition relations. The author tests different plagioclase and melt activity models from literature by regressing 1 bar anhydrous experiments to calculate values approaching to the calorimetric measurement of ΔH_{An}^{fusion} = 135 ± 10 kJ mol^{-1}. By performing cyclic permutations, Putirka (2017) finds that application of different activity models produces very contrasting ΔH_{An}^{fusion} values bounded between 18.7 and 139.6 kJ mol^{-1}, with the majority of data within the range of 18.7-55.2 kJ mol^{-1} (see Table 4 in Putirka, 2017). By propagating errors associated with Eq. (31) and Eq. (39), regression fit of our data returns a similar range of 17.2-50.3 kJ mol^{-1}. It appears that the empirical solution of K_{An}^{eq} leads to ΔH_{An}^{fusion} values much lower than the calorimetric measurement. As explained by Putirka (2017), there is still poor understanding of crystal and melt component activities due to the fact that regression analysis of experimental data fails in determining unequivocal thermodynamic parameters. Regression coefficients are strongly sensitive to the type and number of independent variables and the calibration data used for the regression analysis. As a consequence, although activity models rely on solid thermodynamic principles, their incorporation in thermometers, barometers, and hygrometers may strongly impair the ability prediction of the models (Putirka, 2017).

To calibrate a plagioclase-based thermometer specific to mafic alkaline compositions, we take advantage of the close relation between $K_{\mathrm{An-Ab}}^{eq}$ and T, by adopting the thermodynamic expression recommended in Putirka's works and derived by rearranging Eq. (26) (see Putirka et al., 1996; Putirka, 2005; Putirka, 2008; Putirka, 2017):

$$\frac{10^4}{T\,(K)} = aK_{\mathrm{An-Ab}}^{eq} + b + cP + dln\left(\Theta_1^{melt}\right) + e\left(\Theta_1^{pl}\right) \ldots + Nln(\Theta_n^{melt}, \Theta_n^{pl}) \quad (41)$$

The pressure term cP can be eluded owing to the negligible effect of $\Delta V_{T\,An}^{o}(P)dP$ on the An-Ab exchange reaction. The parameter $Nln(\Theta_n^{melt}, \Theta_n^{pl})$ accounts for the non-ideal behavior of $K_{\mathrm{An-Ab}}^{eq}$ due to mixing and interaction between An and Ab chemical components. $Nln(\Theta_n^{melt}, \Theta_n^{pl})$ represents a pseudo-activity modifying term empirically derived by regression analysis of experimental data (Putirka et al., 1996). *N* may or may not be proportional to the activity coefficient of the component of interest (Putirka, 2008; 2017). If necessary, two components with the same activity coefficient are also combined as cross-product terms to provide the best compositional correction (Supplementary Material 9). Assuming $a_{\mathrm{An}}^{pl} \cong X_{\mathrm{An}}^{pl}$ and $a_{\mathrm{Ab}}^{pl} \cong X_{\mathrm{Ab}}^{pl}$, we calculate $K_{\mathrm{An-Ab}}^{eq}$ through Eq. (39) and Eq. (40). *VIF* analysis indicates that most of melt components are embodied in the calculation of $K_{\mathrm{An-Ab}}^{eq}$. Only X_{An}^{pl} and X_{Ab}^{pl} for plagioclase and a few melt (X_{Si}^{melt}, X_{Ti}^{melt}, X_{Fe}^{melt}, X_{Mg}^{melt}, X_{Ca}^{melt}, $X_{\mathrm{Ti}}^{melt}X_{\mathrm{Al}}^{melt}$, and $X_{\mathrm{Fe}}^{melt}X_{\mathrm{K}}^{melt}$) components are not affected by multicollinearity (*VIF* < 10). Further application of *Mallows' Cp* lowers the number of predictors to X_{An}^{pl} and X_{Ab}^{pl}, as the use of these components is enough to guarantee unbiased regression coefficients. Weighted multiple linear regression analysis yields the following thermometric equation:

$$\frac{10^4}{T\,(K)} = 6.39\,(\pm 0.19) + 0.68\,(\pm 0.05)\ln\left(\frac{X_{An}^{pl}}{a_{An}^{melt}\ from\ Eq.(39)} \times \frac{a_{Ab}^{melt}\ from\ Eq.(40)}{X_{Ab}^{pl}}\right)$$
$$- 1.06\,(\pm 0.19) lnX_{An}^{pl} + 0.81(\pm 0.09) lnX_{Ab}^{pl} \quad (42)$$

Eq. (42) reproduces *T* with R^2 = 0.80 and *SEE* = 11 °C. The incorporation of H_2O^{melt} parameter in Eq. (42) offers a mediocre improvement of ±3 °C (R^2 = 0.91 and *SEE* = 11 °C), emphasizing the subordinate influence of water on $K_{\mathrm{An-Ab}}^{eq}$ relative to the stronger effects of melt and temperature changes. In Fig. 10, the predictive power of Eq. (42) is compared with those of plagioclase-based

thermometers from Putirka (2005) [Eq. (A) and Eq. (D)], Putirka (2008) [Eq. (24a) and Eq. (26)], and Putirka (2017) [Eq. (27a), Eq. (27b), and Eq. (27c)]. It is worth stressing that these models depend on P and/or H_2O^{melt} as input parameters. For this comparison, we calculate the difference between T measured from the experimental data set minus T predicted by each different model, together with the tested standard error of estimate. As a general rule, the precision of previous models derived by regression of large data sets is systematically lower than that of Eq. (42) obtained for a subset of mafic alkaline data. Barometers, thermometers, and hygrometers obtained from restricted ranges of compositions and conditions more closely describe the variance of the calibration data set (Masotta et al., 2013; Mollo et al., 2015c, 2018). However, we note that $^{\text{Eq. (27b)}}SEE$ = 44 °C and $^{\text{Eq. (27c)}}SEE$ = 57 °C obtained for mafic alkaline data are ~10 °C lower than $^{\text{Eq. (27b)}}SEE$ = 55 °C and $^{\text{Eq. (27b)}}SEE$ = 67 °C originally derived by Putirka (2017). Analogously, $^{\text{Eq. (26)}}SEE$ = 29 °C measured in this study is better than $^{\text{Eq. (26)}}SEE$ = 37 °C tested by Putirka (2008). Although some advantages can be envisaged in the use of P-H_2O^{melt}-independent Eq. (42), the disadvantage of thermometers derived from a restricted data set is that they cannot be safely extrapolated to a broad range of compositions and crystallization conditions without returning systematic errors (see for example Masotta et al., 2013; Mollo et al., 2015c, 2018). For volcanic settings compositionally different from Stromboli and Mt. Etna, global regression models reported in Putirka (2008; 2017) are still recommended as their regression parameters and coefficients rely on large calibration data sets, including up to ~1200 plagioclase-melt pairs equilibrated at P, T, and H_2O^{melt} up to ~2.7 GPa, ~1430 °C, and ~13 wt.%, respectively. A virtue of these models is the inclusion of tholeiitic and calcalkaline compositions for which water has a strong non-linear effect on the liquidus depression of both olivine and plagioclase, thus offering a more accurate description for the marked compositional change of the melt in equilibrium with variable mineral assemblages as a function of dissolved water (Almeev et al., 2012 and references therein).

The enduring paradigm of estimating mineral saturation temperature under natural crystallization conditions is that we do not know *a priori* the melt composition in equilibrium with a

specific single crystal and/or crystal zone. As a first approximation, the composition of matrix melt can be tentatively paired with that of plagioclase phenocryst rim, if it is verified that cooling and decompression processes do not cause microlite crystallization at the time of eruption. Alternatively, the bulk rock analysis can be equilibrated with the anorthitic plagioclase core, if feldspar is recognized as the early liquidus phase. However, this is a rare event for mafic alkaline magmas where plagioclase crystallize cotectically with clinopyroxene (Armienti et al., 2013; Mollo et al., 2015a). In volcanic settings, the occurrence of residual melts is generally sporadic due to abundant syn- and post-eruptive crystallization of matrix minerals. Moreover, open-system processes such as magma mixing, mush cannibalism, and hybridization reactions cause juxtaposition of plagioclase crystals with very different growth histories, even at the small scale of a thin section (Cashman and Blundy, 2013). For this reason, recognition of the correct chemical correspondence between a variably zoned plagioclase and melt composition it is not a trivial task, essentially in relation to the polybaric-polythermal transfer of magma through compositionally distinct reservoirs and the kinetic growth of crystals (Mollo et al., 2011; Humphreys et al., 2016). To obviate this issue, plagioclase-melt equilibrium can be restored by 1) mass balances in which aliquots of representative mineral phases are subtracted/added back to the bulk rock analysis and 2) by testing different more or less differentiated bulk rock analyses representative of the overall magma evolutionary path of the eruptive period of interest (e.g., Armienti et al., 2013 and Mollo et al., 2018). As illustrated above, predictive models based on X_{An}^{pl} [i.e., Eq. (31) and Eq. (33)] of Namur et al. (2012) recover plagioclase-melt equilibrium with a satisfactory uncertainty of ±0.04 (Fig. 8). However, by performing correlation analysis on mafic alkaline data (Supplementary Material 10), we identify first-order and second-order compositional terms that are more tightly correlated with X_{An}^{pl}:

$$X_{An}^{pl} = 2.41(\pm 0.71) - \frac{1800(\pm 521)}{T} + 0.98(\pm 0.33)X_{Ti} - 0.58(\pm 0.16)X_{Ti}X_{Mg}$$
$$-0.17(\pm 0.06)X_{Fe}X_{Na} + 0.40(\pm 0.05)X_{Mg}X_{Ca} \qquad (43)$$

This refined equilibrium model is associated with $R^2_{XAn} = 0.94$ and $SEE_{XAn} = 0.02$. For plagioclase in thermodynamic equilibrium with the host melt, the difference (Δ) between X^{pl}_{An} predicted by Eq. (43) and X^{pl}_{An} measured in plagioclase should be equal to zero. But such a theoretical value does not consider the analytical uncertainty associated with major oxide analysis and error propagation in the estimate of X^{pl}_{An}. In conformity with other equilibrium models (e.g., Putirka et al., 1996; Masotta et al., 2013; Mollo et al., 2013), achievement of near-equilibrium crystallization can be expected for $\Delta X^{pl}_{\mathrm{An}}$ within the calibration error of ±0.02 obtained by weighted multiple regression analysis of the mafic alkaline data set. We report in Supplementary Material 11 an EXCEL spreadsheet and a MATLAB code to model intracrystalline heterogeneities in plagioclase as a function of temperature and melt-water concentration. For this purpose, thermometric and equilibrium equations from this study [i.e., Eq. (42) and Eq. (43), respectively] are interpolated with previous hygrometric (Putirka, 2005, 2008; Lange et al., 2009; Waters and Lange, 2015) and equilibrium (Namur et al., 2012) equations from the literature.

6. Interpreting *T* and H_2O^{melt} in zoned plagioclase crystals

Compositional zoning patterns in plagioclase crystals are routinely used by petrologists and volcanologists to estimate the intensive variables governing magma crystallization at pre- and syn-eruptive conditions (e.g., Humphreys et al., 2016; Crabtree and Lange, 2011; Cashman and Blundy, 2013). Here we focus on plagioclase phenocrysts from eight eruptive products representative of normal (24/5/2013, 26/11/2019, and 10/10/2021), major, (8/11/2009, 23/10/2017, and 19/7/2020), and paroxysmal (15/3/2007 and 3/7/2019) explosions at Stromboli in the period from March 2007 to October 2021. Plagioclase phenocrysts from different eruptions are texturally and compositionally similar, as described in Supplementary Material 12. Following the classification scheme proposed by Landi et al. (2004), crystal zoning patterns can be categorized into four textural domains:

1) subrounded corroded cores (SCC) showing prevalent patchy textures. SCC have anorthite-bytownite compositions, with average An^{pl} = 81 mol.% and σ = ±3 mol.%, where σ refers to the standard deviation of An^{pl};

2) sieve-textured concentric layers (STCL) showing abundant micrometric glass inclusions. STCL overgrow on dissolution surfaces that are characterized by angular unconformities and crenulated margins. The thickness of each layer is variable from ~10 to ~100 μm. The composition is anorthite-bytownite, with average An^{pl} = 78 mol.% and σ = ±5 mol.%;

3) oscillatory-zoned concentric layers (OZCL) developing as low amplitude-high frequency oscillatory patterns free of glass inclusions, with little An^{pl} variations ($\Delta An^{pl} \leq 4$ mol.%) and zone widths of 1-5 μm. The composition is bytownite-labradorite, with average An^{pl} = 67 mol.% and σ = ±3 mol.%. Most of the plagioclase phenocryst mantles consist of alternating bands of An-poor OZCL and An-rich STCL domains. Sometimes, OZCL are partly corroded by STCL via the formation of irregular resorption-regrowth An-rich surfaces that crosscut the inner and more An-poor oscillatory zoning patterns;

4) overgrowth rims (OR) with thickness variable from ~10 to ~60 μm and in direct contact with the matrix glass. OR are characterized by marked evolved compositions, with average An^{pl} = 65 mol.% and σ = ±2 mol.%.

According to Landi et al. (2004), STCL grow on erosional surfaces in plagioclase phenocrysts that involve successive dissolution-crystallization processes via recurrent inputs of hot, volatile-rich *Lp*-magmas rising from depth into the uppermost segment of the feeding system, in which colder and more degassed *Hp*-magmas are stored. *In situ* trace element and Sr isotope analyses of plagioclase phenocrysts by Francalanci et al. (2005, 2012) point out that STCL-OZCL alternation results from up to ~30% of *Lp*-*Hp* magma mixing causing significant Sr isotope disequilibrium. In this scenario, SCC are interpreted as relic antecrysts belonging to a crystal mush that developed from older progenitor magmas with high Sr isotope ratios. Hotter and more mafic *Lp*-magmas with low Sr

isotope ratios pass through the crystal mush column, cannibalize the antecrysts and then transport them into the *Hp*-reservoir (Francalanci et al., 2005, 2012). Periods of relatively slow growth in the *Hp*-reservoir promote the formation of OZCL via sluggish kinetic effects due to small perturbations in the concentration of the melt next to the plagioclase interface (Landi et al., 2004) and/or crystal convection along small thermal and compositional gradients by continuous *Lp*-*Hp* magma mixing (Francalanci et al., 2005). The cross-cutting relationships between STCL and OZCL domains record resorption-regrowth events due to recurrent *Lp*-*Hp* magma mixing in the *Hp*-reservoir. This produces new hybrid magmas with intermediate Sr isotope ratios feeding the growth of STCL by partial dissolution of pre-existing OZCL formed in the *Hp*-reservoir (Francalanci et al., 2005, 2012). OR are strongly depleted in An due to late textural equilibration at low-*T*, low-*P* conditions by abundant magma degassing (Landi et al., 2004), also in accord with *in situ* Sr isotope analyses suggesting isotopic equilibrium between OR and the glassy groundmass (Francalanci et al., 2012).

Integration of numerical multiphase steady-state modeling (La Spina et al., 2015) and thermodynamic calculations (Landi et al., 2004) indicates that most of plagioclase crystallization takes place at $P \leq 130$ MPa, T ≤ 1135 °C, and $H_2O^{melt} \leq 2.8$ wt.% for $P_{H2O} < P_{total}$ (Landi et al., 2004). Numerical modeling data point out also that the decrease of temperature has a great influence on magma ascent dynamics and is related to a non-isothermal condition along the conduit, as the result of competition between crystallization (heating) and gas expansion (cooling) processes (La Spina et al., 2015). Because crystallization and melt viscosity are both strongly temperature-dependent, these results emphasize that temperature, rather than melt-water content, plays an important role on controlling the volume flow rate and the crystal content of Stromboli magmas at the vent of the conduit. For instance, the mass discharge rate increases by an order of magnitude upon a *T* variation of 30 °C, whereas an increase of 1 wt.% in H_2O^{melt} has a much smaller effect causing that the mass discharge rate increases by at most a factor of ~5 (La Spina et al., 2015). Also, it is not excluded that the ascent of water-undersaturated *Lp*-magmas from greater depths may lower the saturation surface of plagioclase by promoting the stabilization of An-rich compositions and

dissolution of An-poor crystals still surviving within the mush column (Nelson and Montana, 1992; Ginibre and Worner, 2007).

Through the use of plagioclase-melt models reported in Supplementary Material 11, we estimate T from Eq. (42) and H_2O^{melt} from the hygrometers of Putirka (2008) and Waters and Lange (2015) for different textural domains in plagioclase (see Supplementary Material 12). The equilibrium condition between plagioclase and the matrix glass is also tested by employing Eq. (43) to prevent unreliable estimates (cf. Mollo et al., 2011; Humphreys et al., 2016). Results from calculations are displayed in Fig. 11 as violin plots and box plots for An^{pl}, T, and H_2O^{melt}. A kernel density estimation is used to visualize the underlying probability density function of each set of data in violin plots, whereas the statistical dispersion of data is illustrated by the box. For T and H_2O^{melt} estimates, box plots account for model errors and error propagation effect. Once the T uncertainty of ±11 °C from Eq. (42) is propagated into the hygrometric equations, an average percentage error of ~16-19% is associated to each H_2O^{melt} estimate and is in addition to the original calibration errors of the hygrometers (i.e., 1.1 and 0.35 wt.% H_2O^{melt} for the model of Putirka, 2008 and Waters and Lange, 2015, respectively). The length of the box represents the interquartile range (*IQR*) extending from the first quartile (25th percentile *Q1*) to the third quartile (75th percentile *Q3*) and whiskers go from each quartile to the minimum or maximum (see Supplementary Material 12). Violin plots show symmetric and asymmetric shapes extending beyond the actual minimum and maximum estimates of T and H_2O^{melt}, owing to the fact kernel density projections are greater than the errors associated with thermometric and hygrometric calculations (Fig. 11). The bandwidth of each violin curve corresponds with the approximate frequency of data in each region and accounts to stretched (small bandwidth) or compressed (large bandwidth) data distributions (Fig. 11). For a given textural domain, we observe that *IQR* from box plots systematically overlap, and no apparent variations can be appreciated from one eruption to another and/or from different types of eruptions (Fig. 11). This indicates that the crystallization history of plagioclase phenocrysts at Stromboli is controlled by steady-state magma dynamics resulting from highly efficient magma mixing and degassing regimes, even if the eruptive

style changes from normal to major to paroxysmal events (Petrone et al., 2016, 2018). According to Di Stefano et al. (2020), continuous injections of mafic *Lp*-magmas mix with the more differentiated mush melts migrating into the shallow reservoir, thus preserving the compositional uniformity of the *Hp*-magma. Differently from olivine and clinopyroxene, plagioclase saturates the basaltic melt at the late stage of crystallization within the uppermost part of the mush (e.g., Di Stefano et al., 2020). As a consequence, zoning patterns in plagioclase phenocrysts from the same textural domain record almost equivalent T and H_2O^{melt} conditions due to the steady-state dynamics of an open conduit system undergoing continuous recharge, crystallization, and eruption (Fig. 11).

Box plots of An^{pl} (Fig. 11a) and T (Fig. 11b) tend to overlap, showing a pair-wise behavior for SCC + STCL and OZCL + OR. The maximum probability distribution of An^{pl} is embodied within the *Q1*-*Q3* range (Supplementary Material 12) and corresponds to anorthitic compositions of 78-84 (SCC) and 74-83 (STCL), and 64-70 (OZTL), and 63-67 (OR) mol.% for the 2007-2021 eruptive period. Similarly, we found that the maximum probability distribution of T is 1097-1124 (SCC), 1097-1114 (STCL), 1072-1089 (OZTL), and 1070-1082 (OR) °C (Fig. 11b). In this regard, SCC and STCL reflect high thermal conditions due to inputs of *Lp*-magmas passing through the mush column, OZTL denotes an intermediate cooling stage for magmas residing within the *Hp*-reservoir, and OR likely records the closure temperature of the plagioclase growth at the time of eruption (Di Stefano et al., 2020 and references therein).

For H_2O^{melt} estimated by the hygrometer of Putirka (2008), SCC and STCL box plots are very similar and correspond to melt-water contents lower than those of OZCL and OR box plots (Fig. 11c), in accord with the spatial distribution of An^{pl} (Fig. 11a) and T (Fig. 11b). The maximum probability distribution of H_2O^{melt} is 2.0-2.4 (SCC), 2.1-2.5 (STCL), 2.4-2.8 (OZTL), and 2.5-2.8 (OR) wt.% (Fig. 11c). In general, phenocryst zoning patterns return H_2O^{melt} estimates higher than 2 wt.% (Fig. 11c), which are very similar to those modeled by La Spina et al. (2015) for the ascent of magma within the crystal mush, but just before rapid microlite crystallization during magma acceleration and abundant volatile exsolution in the uppermost part of the conduit where $H_2O^{melt} \leq 2$ wt.% at depth ≤

1 km. Moreover, the hygrometer of Putirka (2008) records higher amounts of H_2O^{melt} (Fig. 11c) at lower *T* (Fig. 11b), as the bulk system composition evolves towards lower calcium concentrations in the residual melt and coexisting plagioclase (Fig. 11a) with increasing the degree of crystallization in the colder parts of the mush column. Indeed, as outlined in several works (Armienti et al., 2013; Mollo et al., 2015a; Di Stefano et al., 2020; Palummo et al., 2020), the crystallization of nominally anhydrous minerals (i.e., clinopyroxene and plagioclase) at shallow depths may increase the water content in fluid-undersaturated melts, whereas CaO in the melt and An in plagioclase decrease during magma evolution. The increase of H_2O^{melt} with decreasing both *T* and An^{pl} corroborates also the thermodynamic principle expressed by Wood and Blundy (2002): for a mineral phase to remain on the liquidus with increasing H_2O^{melt}, the effect of water in lowering the activities of major components must be exactly compensated by an increase of free energy of fusion with decreasing temperature. On the other hand, for H_2O^{melt} estimated by the hygrometer of Waters and Lange (2015), violin plots and box plots from plagioclase textural domains show less marked differences, with maximum probability distributions of 1.9-2.3 (SCC), 1.9-2.4 (STCL), 2.1-2.4 (OZTL), and 2.1-2.4 (OR) wt.% (Fig. 11d). The predictive power of this model is strongly mediated by rival effects between temperature and melt-water content, as a consequence the decrease of H_2O^{melt} (Fig. 11d) with increasing *T* (Fig. 11b) is attenuated by the increase of An^{pl} (Fig. 11a), and *vice versa*.

What we learn from the comparative application of the hygrometers of Putirka (2008) and Waters and Lange (2015) is that the two models were calibrated using very different experimental compositions and regression strategies. The model of Putirka (2008) strictly depends on the change of bulk system composition, including An^{pl} and melt major oxides, such that the estimated amount of H_2O^{melt} (Fig. 11c) markedly decreases with increasing *T* (Fig. 11b). Conversely, less marked plagioclase-based hygrometric predictions from the model of Waters and Lange (2015) are more convoluted with compositional-temperature effects controlling the An-Ab exchange reaction. The overriding implication for mafic alkaline magmas is that *T* and H_2O^{melt} can be simultaneously determined for different plagioclase textural patterns if crystals are sufficiently strongly zoned, and a

maximum probability estimation is derived for different textural domains by applying kernel density analysis. However, addition of moderate amounts of water to mafic alkaline melts does not cause substantial modifications for the An-Ab exchange reaction (Fig. 5). As a consequence, the model of Waters and Lange (2015) appears less sensitive to moderate water changes, as the influence of H_2O^{melt} on An and Ab activities and activity coefficients is mitigated by change of anhydrous melt components as a function of temperature (cf. §5.2).

7. Conclusions and recommendations

By reviewing natural and experimental plagioclase growth rates from literature and comparing them with new data obtained for mafic alkaline compositions, we document that the temporal scale of plagioclase morphological evolution is intrinsically related to the change of crystal growth rate upon the effect of interface kinetics. A certain degree of undercooling, leading to melt supersaturation effects, is an essential condition to promote the growth of plagioclase; otherwise the establishment of a full thermodynamic equilibrium throughout the crystal-melt interface would correspond to a minimum energy state at which the plagioclase growth is halted. According to these kinetic principles, there is a net linear decay of plagioclase growth rate with increasing crystallization time on a logarithmic scale, in response to superimposition of diffusive relaxation phenomena over supersaturation effects at the interface melt. Results from a multifaceted statistical analysis provide that plagioclase growth kinetics can be parameterized under a broad range of isothermal-isobaric and decompression conditions representative of crystallization conditions typically encountered by mafic alkaline magmas at Stromboli and Mt. Etna in Italy. Modeling of crystal size distributions in natural erupted products indicates that degassing-induced microlite crystallization takes place in the order of minutes during fast disequilibrium ascent and acceleration of magma within the conduit. The formation of tiny, elongated plagioclase microlites from explosive eruptions is primarily dictated by fast crystallization kinetics associated with large degrees of undercooling and rapid crystal growth

regimes which result from highly dynamic, supersaturated melts. Conversely, large, tabular plagioclase phenocrysts from lava flows grow in response to sluggish kinetic effects associated with small degrees of undercooling and slow crystal growth regimes from more relaxed melts. As a matter of fact, plagioclase phenocrysts within the deeper parts of the plumbing system have more time to grow and equilibrate with the melt upon temporal scales of years.

By reassessing compositional and thermodynamic data from literature, we find that the role of water becomes dominantly important on the control of plagioclase stability and albite-anorthite compositional variability in more differentiated silicic melts, but this effect is evidently less influential for subtle water ranges in mafic alkaline magmas. According to this argument, the predominant effect of temperature on plagioclase saturation is responsible to the weak control of water on melt anorthite and albite activity coefficients as the crystallization of plagioclase proceeds during magma cooling. Different tests carried out on plagioclase-melt compositional data sets from Stromboli provide some practical guidelines that we consider important for future petrological studies. The iterative use of equilibrium, thermometric, and hygrometric equations may represent a secure approach for understanding complex magma dynamics if different textural domains are identified for strongly zoned plagioclase phenocrysts. Owing to error propagation effects resulting from the integration of different modeling equations into a single algorithm, probability-based criteria are also required to correctly disambiguate the role of temperature and melt-water content on plagioclase growth history. The interpretation of iterative modeling data depends on the perception that well categorized plagioclase textures are herald of specific physico-chemical conditions related to the crystallization of magma. Therefore, error propagation issues can be circumvented through kernel density analysis in which temperature and melt-water contents are first predicted as averages of compositional profiles from different plagioclase textural domains and then evaluated as maximum probability distributions.

As ultimate recommendation, we would caution against using plagioclase and melt compositions that are not tested for equilibrium and may potentially lead to imprecise estimates.

Plagioclase-melt equilibrium should be always verified using as many different methods as permitted by the sample data set. A side effect of such approach is the minimization of disequilibrium effects controlling the growth of plagioclase upon magma mixing and ascent dynamics, thus bounding the petrological predictions to isochemical, isobaric, and isothermal conditions. Testing for equilibrium is an essential data-filter attribute for petrological modeling.

Acknowledgments

Part of this work was supported by Natural Environment research Council UK grant NE/T009292/1 to CMP, INGV Progetti Ricerca Libera 2019 Grant #52/2020 and INGV Departmental Strategic Project UNO to PS, and PRIN MIUR Grant #2017J277S9_004 to AP.

References

Agostini, C., Fortunati, A., Arzilli, F., Landi, P., Carroll, M.R., 2013. Kinetics of crystal evolution as a probe to magmatism at Stromboli (Aeolian Archipelago, Italy). Geochim. Cosmochim. Acta 110, 135–151. https://doi.org/10.1016/j.gca.2013.02.027.

Aigner-Torres, M., Blundy, J., Ulmer, P., Pettke, T., 2007. Laser Ablation ICPMS study of trace element partitioning between plagioclase and basaltic melts: an experimental approach. Contrib. Mineral. Petrol. 153, 647–667. https://doi.org/10.1007/s00410-006-0168-2.

Allard, P., Aiuppa, A., Loyer, H., Carrot, F., Gaudry, A., Pinte, G., Michel, A., Dongarrà, G., 2000. Acid Gas and Metal Emission Rates during Long-lived Basalt Degassing at Stromboli Volcano. Geophys. Res. Lett. 27, 1207-1210.

Almeev, R.R., Holtz, F., Koepke, J., Parat, F., 2012. Experimental calibration of the effect of H2O on plagioclase crystallization in basaltic melt at 200 MPa. American Mineralogist 97, 1234–1240. https://doi.org/10.2138/am.2012.4100.

Aloisi, M., Bonaccorso, A., Gambino, S., 2006. Imaging composite dike propagation (Etna, 2002 case). J. Geophys. Res. 111, B06404. https://doi.org/10.1029/2005JB003908.

Andrews, B.J., 2021. Plagioclase population dynamics and zoning in response to changes in temperature and pressure. American Mineralogist 106, 1438–1452. https://doi.org/10.2138/am-2021-7491.

Andronico, D., Branca, S., Calvari, S., Burton, M., Caltabiano, T., Corsaro, R.A., Del Carlo, P., Garfì, G., Lodato, L., Miraglia, L., Murè, F., Neri, M., Pecora, E., Pompilio, M., Salerno, G., Spampinato, L., 2005. A multi-disciplinary study of the 2002?03 Etna eruption: insights into a complex plumbing system. Bull. Volcanol. 67, 314–330. https://doi.org/10.1007/s00445-004-0372-8.

Armienti, P., 2008. Decryption of Igneous Rock Textures: Crystal Size Distribution Tools. Rev. Mineral. Geochem. 69, 623-649.

Armienti, P., Pareschi, M.T., Innocenti, F., Pompilio, M., 1994. Effects of magma storage and ascent on the kinetics of crystal growth: The case of the 1991-93 Mt. Etna eruption. Contrib. Mineral. Petrol. 115, 402–414. https://doi.org/10.1007/BF00320974.

Armienti, P., Pareschi, M.T., Pompilio, M., 1997. Lava textures and time scales of magma storage at Mt. Etna (Italy). Acta Vulcanol. 9, 1–5

Armienti, P., Perinelli, C., Putirka, K.D., 2013. A New Model to Estimate Deep-level Magma Ascent Rates, with Applications to Mt. Etna (Sicily, Italy). J. Petrol. 54, 795–813. https://doi.org/10.1093/petrology/egs085.

Arzilli, F., La Spina, G., Burton, M.R., Polacci, M., Le Gall, N., Hartley, M.E., Di Genova, D., Cai, B., Vo, N.T., Bamber, E.C., Nonni, S., Atwood, R., Llewellin, E.W., Brooker, R.A., Mader, H.M., Lee, P.D., 2019. Magma fragmentation in highly explosive basaltic eruptions induced by rapid crystallization. Nat. Geosci. 12, 1023–1028. https://doi.org/10.1038/s41561-019-0468-6.

Bai, L., Baker, D.R., Rivers, M., 2008. Experimental study of bubble growth in Stromboli basalt melts at 1 atm. Earth Planet. Sci. Lett. 267, 533-547.

Barberi, F., Rosi, M., Sodi, A., 1993. Volcanic hazard assessment at Stromboli based on review of histroical data. Acta Vulcanol. 3, 173-187.

Blundy, J., Cashman, K., Humphreys, M., 2006. Magma heating by decompression-driven crystallization beneath andesite volcanoes. Nature 443, 76–80. https://doi.org/10.1038/nature05100.

Botcharnikov, R.E., Almeev, R.R., Koepke, J., Holtz, F., 2008. Phase Relations and Liquid Lines of Descent in Hydrous Ferrobasalt--Implications for the Skaergaard Intrusion and Columbia River Flood Basalts. J. Petrol. 49, 1687–1727. https://doi.org/10.1093/petrology/egn043.

Bottinga, Y., Weill, D.F., 1972. The viscosity of magmatic silicate liquids; a model calculation. Am J Sci 272, 438. https://doi.org/10.2475/ajs.272.5.438.

Brugger, C.R., Hammer, J.E., 2010. Crystallization Kinetics in Continuous Decompression Experiments: Implications for Interpreting Natural Magma Ascent Processes. J. Petrol. 51, 1941–1965. https://doi.org/10.1093/petrology/egq044.

Burkhard, D.J.M., 2002. Kinetics of crystallization: example of micro-crystallization in basalt lava. Contrib. Mineral. Petrol. 142, 724–737. https://doi.org/10.1007/s00410-001-0321-x.

Burkhard, D.J.M., 2005a. Relation between oxidation/crystallization and degassing upon reheating of basalt glass from Kilauea, Hawaii. Mineral. mag. 69, 103–117. https://doi.org/10.1180/0026461056920238.

Burkhard, D.J.M., 2005b. Nucleation and growth rates of pyroxene, plagioclase, and Fe-Ti oxides in basalt under atmospheric conditions. Eur. J. Mineral. 17, 675–686. https://doi.org/10.1127/0935-1221/2005/0017-0675.

Burnham, C.W., 1975. Water and magmas; a mixing model. Geochim. Cosmochim. Acta 39, 1077-1084.

Carmichael, I.S.E., Nicholls, J., Spera, F.J., Wood, B.J., Nelson S.A., 1977. High-temperature properties of silicate liquids: applications to the equilibration and ascent of basic magma. Philos. Trans. Royal. Soc. A, 286, 373–431. http://doi.org/10.1098/rsta.1977.0124.

Carpenter, M.A., 1988. Thermochemistry of Aluminium/Silicon Ordering in Feldspar Minerals, in: Salje, E.K.H. (Ed.), Physical Properties and Thermodynamic Behaviour of Minerals. Springer Netherlands, Dordrecht, pp. 265–323. https://doi.org/10.1007/978-94-009-2891-6_9.

Cashman, K., Blundy, J., 2013. Petrological cannibalism: the chemical and textural consequences of incremental magma body growth. Contrib. Mineral. Petrol. 166, 703–729. https://doi.org/10.1007/s00410-013-0895-0.

Cashman, K.V., 1993. Relationship between plagioclase crystallization and cooling rate in basaltic melts. Contrib. Mineral. Petrol. 113, 126–142. https://doi.org/10.1007/BF00320836.

Cashman, K.V., 1990. Textural constraints on the kinetics of crystallization of igneous rocks. Rev Mineral Geochem 24, 259–314.

Cashman, K.V., Marsh, B.D., 1988. Crystal size distribution (CSD) in rocks and the kinetics and dynamics of crystallization II: Makaopuhi lava lake. Contrib. Mineral. Petrol. 99, 292–305. https://doi.org/10.1007/BF00375363.

Cashman, K.V., Thornber, C., Kauahikaua, J.P., 1999. Cooling and crystallization of lava in open channels, and the transition of Pāhoehoe Lava to ’A’ā. Bull Volcanol 61, 306–323. https://doi.org/10.1007/s004450050299.

Cassidy, M., Castro, J.M., Helo, C., Troll, V.R., Deegan, F.M., Muir, D., Neave, D.A., Mueller, S.P., 2016. Volatile dilution during magma injections and implications for volcano explosivity. Geology 44, 1027–1030. https://doi.org/10.1130/G38411.1.

Cassidy, M., Manga, M., Cashman, K., Bachmann, O., 2018. Controls on explosive-effusive volcanic eruption styles. Nat. Commun. 9, 2839. https://doi.org/10.1038/s41467-018-05293-3.

Clocchiatti, R., 1981. La transition augite-diopside et les liquides silicatés intra-cristallins dans les pyroclastes de l’activité actuelle du Stromboli: témoignages de la réinjection et du mélange magmatiques. Bull. Volcanol. 44, 339-357. https://doi.org/10.1007/BF02600569.

Conte, A.M., Perinelli, C., Trigila, R., 2006. Cooling kinetics experiments on different Stromboli lavas: Effects on crystal morphologies and phases composition. J. Volcanol. Geotherm. Res. 155, 179–200. https://doi.org/10.1016/j.jvolgeores.2006.03.025.

Corrigan, G.M., 1982. Supercooling and the crystallization of plagioclase, olivine, and clinopyroxene from basaltic magmas. Mineral. mag. 46, 31–42. https://doi.org/10.1180/minmag.1982.046.338.06.

Corsaro, R.A., Civetta, L., Di Renzo, V., Miraglia, L., 2009. Petrology of lavas from the 2004–2005 flank eruption of Mt. Etna, Italy: inferences on the dynamics of magma in the shallow plumbing system. Bull Volcanol 71, 781–793. https://doi.org/10.1007/s00445-009-0264-z.

Couch, S., 2003. Experimental investigation of crystallization kinetics in a haplogranite system. American Mineralogist 88, 1471–1485. https://doi.org/10.2138/am-2003-1011.

Couch, S., Sparks, R.S.J., Carroll, M.R., 2001. Mineral disequilibrium in lavas explained by convective self-mixing in open magma chambers. Nature 411, 1037–1039. https://doi.org/10.1038/35082540.

Couch, S., Sparks, R.S.J., Carroll, M.R., 2003. The Kinetics of Degassing-Induced Crystallization at Soufrière Hills Volcano, Montserrat. J. Petrol. 44, 1477-1502.

Crabtree, S.M., Lange, R.A., 2011. Complex Phenocryst Textures and Zoning Patterns in Andesites and Dacites: Evidence of Degassing-Induced Rapid Crystallization? J. Petrol. 52, 3–38. https://doi.org/10.1093/petrology/egq067.

Di Fiore, F., Vona, A., Kolzenburg, S., Mollo, S., Romano, C., 2021. An Extended Rheological Map of Pāhoehoe—‘A‘ā Transition. JGR Solid Earth 126. https://doi.org/10.1029/2021JB022035.

Di Genova, D., Sicola, S., Romano, C., Vona, A., Fanara, S., Spina, L., 2017. Effect of iron and nanolites on Raman spectra of volcanic glasses: A reassessment of existing strategies to estimate the water content. Chem. Geol. 475, 76–86. https://doi.org/10.1016/j.chemgeo.2017.10.035.

Di Stefano, F., Mollo, S., Ubide, T., Petrone, C.M., Caulfield, J., Scarlato, P., Nazzari, M., Andronico, D., Del Bello, E., 2020. Mush cannibalism and disruption recorded by clinopyroxene phenocrysts

at Stromboli volcano: New insights from recent 2003–2017 activity. Lithos 360–361, 105440. https://doi.org/10.1016/j.lithos.2020.105440.

Dohmen, R., Blundy, J., 2014. A predictive thermodynamic model for element partitioning between plagioclase and melt as a function of pressure, temperature and composition. Am J Sci 314, 1319–1372. https://doi.org/10.2475/09.2014.04.

Dowty, E., 1980. Crystal growth and nucleation theory and the numerical simulation of igneous crystallization. In: Hargraves, R.B. (Ed.), The Physics of Magmatic Processes. Princeton University Press, Princeton, New Jersey, USA, pp. 419–485.

Fenn, P.M., 1977. The nucleation and growth of alkali feldspar from hydrous melts. The Canadian Mineralogist 15(2), 135-161.

Fornaciai, A., Landi, P., Armienti, P., 2009. Dissolution/crystallization kinetics recorded in the 2002–2003 lavas of Stromboli (Italy). Bull Volcanol 71, 631–641. https://doi.org/10.1007/s00445-008-0249-3.

Francalanci, L., Davies, G.R., Lustenhouwer, W., Tommasini, S., Mason, P.R.D., Conticelli, S., 2005. Intra-Grain Sr Isotope Evidence for Crystal Recycling and Multiple Magma Reservoirs in the Recent Activity of Stromboli Volcano, Southern Italy. J. Petrol. 46, 1997–2021. https://doi.org/10.1093/petrology/egi045.

Francalanci, L., Avanzinelli, R., Nardini, I., Tiepolo, M., Davidson, J.P., Vannucci, R., 2012. Crystal recycling in the steady-state system of the active Stromboli volcano: a 2.5-ka story inferred from in situ Sr-isotope and trace element data. Contrib. Mineral. Petrol. 163, 109–131. https://doi.org/10.1007/s00410-011-0661-0.

Francalanci, L., Lucchi, F., Keller, J., De Astis, G., Tranne, C.A., 2013. Eruptive, volcano-tectonic and magmatic history of the Stromboli volcano (north-eastern Aeolian archipelago). Geol. Soc. Lond. Mem. 37, 397–471. https://doi.org/10.1144/M37.13.

Gaetani, G.A., Grove, T.L., 1998. The influence of water on melting of mantle peridotite. Contrib. Mineral. Petrol. 131, 323–346.

Ghiorso, M.S., Carmichael, I.S.E., 1980. A regular solution model for met-aluminous silicate liquids: Applications to geothermometry, immiscibility, and the source regions of basic magmas. Contrib. Mineral. Petrol. 71, 323–342. https://doi.org/10.1007/BF00374706.

Ghiorso, M.S., Carmichael, I.S.E., Rivers, M.L., Sack, R.O., 1983. The Gibbs free energy of mixing of natural silicate liquids; an expanded regular solution approximation for the calculation of magmatic intensive variables. Contrib. Mineral. Petrol. 84, 107–145. https://doi.org/10.1007/BF00371280.

Giacomoni, P.P., Coltorti, M., Mollo, S., Ferlito, C., Braiato, M., Scarlato, P., 2018. The 2011–2012 paroxysmal eruptions at Mt. Etna volcano: Insights on the vertically zoned plumbing system. J. Volcanol. Geotherm. Res. 349, 370–391. https://doi.org/10.1016/j.jvolgeores.2017.11.023.

Giacomoni, P.P., Ferlito, C., Coltorti, M., Bonadiman, C., Lanzafame, G., 2014. Plagioclase as archive of magma ascent dynamics on "open conduit" volcanoes: The 2001–2006 eruptive period at Mt. Etna. Earth Sci Rev 138, 371–393. https://doi.org/10.1016/j.earscirev.2014.06.009.

Ginibre, C., Wörner, G., 2007. Variable parent magmas and recharge regimes of the Parinacota magma system (N. Chile) revealed by Fe, Mg and Sr zoning in plagioclase. Lithos 98, 118–140. https://doi.org/10.1016/j.lithos.2007.03.004.

Giuliani, L., Iezzi, G., Vetere, F., Behrens, H., Mollo, S., Cauti, F., Ventura, G., Scarlato, P., 2020. Evolution of textures, crystal size distributions and growth rates of plagioclase, clinopyroxene and spinel crystallized at variable cooling rates from a mid-ocean ridge basaltic melt. Earth Sci Rev 204, 103165. https://doi.org/10.1016/j.earscirev.2020.103165.

Glazner, A.F., 1984. Activities of olivine and plagioclase components in silicate melts and their application to geothermometry. Contrib. Mineral. Petrol. 88, 260–268. https://doi.org/10.1007/BF00380170.

Grove, T.L., 1978. Cooling histories of Luna 24 very low Ti (VLT) ferrobasalts: An experimental study. Proc. Lunar Planet. Sci. Conf. 9th, 565-584.

Grove, T.L., 1990. Cooling histories of lavas from Serocki Volcano. In: Detrick, R., Honnorez, J., Bryan, W.B., Juteau, T., et al., Proc. ODP, Sci. Results, 106/109: College Station, TX (Ocean Drilling Program), 3-8. https://doi.org/10.2973/odp.proc.sr.106109.113.1990.

Gualda, G.A.R., Ghiorso, M.S., Lemons, R.V., Carley, T.L., 2012. Rhyolite-MELTS: a modified calibration of MELTS optimized for silica-rich, fluid-bearing magmatic systems. J. Petrol. 53, 875–890

Hammer, J.E., 2008. Experimental Studies of the Kinetics and Energetics of Magma Crystallization. Rev Mineral Geochem 69, 9–59. https://doi.org/10.2138/rmg.2008.69.2.

Hammer, J.E., Rutherford, M.J., 2002. An experimental study of the kinetics of decompression-induced crystallization in silicic melt. J. Geophys. Res. 107, ECV 8-1-ECV 8-24. https://doi.org/10.1029/2001JB000281.

Hair, J.F., Anderson, R.E., Tatham, R.L., Black, W.C., 1995. Multivariate data analysis. Englewood Cliffs, NJ: Prentice-Hall.

Harris, R.R., Kanji, G.K., 1983. On the Use of Minimum Chi-Square Estimation. The Statistician 32, 379-394. https://doi.org/10.2307/2987540.

Higgins, M.D., 2000. Measurement of crystal size distributions. American Mineralogist 85, 1105-1116.

Housh, T.B., Luhr, J.F., 1991. Plagioclase-melt equilibria in hydrous systems. American Mineralogist 76, 477-492.

Huggins, E.G., Ruprecht, P., Ghiorso, M.S., 2021. Using Chemical Affinities to Understand Disequilibrium Textures of Plagioclase Preserved in Magmatic Systems. Geophys. Res. Lett. 48. https://doi.org/10.1029/2021GL092884.

Humphreys, M.C.S., Edmonds, M., Klöcking, M.S., 2016. The validity of plagioclase-melt geothermometry for degassing-driven magma crystallization. American Mineralogist 101, 769–779. https://doi.org/10.2138/am-2016-5314.

Iezzi, G., Mollo, S., Torresi, G., Ventura, G., Cavallo, A., Scarlato, P., 2011. Experimental solidification of an andesitic melt by cooling. Chem. Geol. 283, 261–273. https://doi.org/10.1016/j.chemgeo.2011.01.024.

Iezzi, G., Mollo, S., Shahini, E., Cavallo, A., Scarlato, P., 2014. The cooling kinetics of plagioclase feldspar as revealed by electron-microprobe mapping. American Mineralogist 99, 898–907.

Ikeda, Y., 1977. Grain size of plagioclase of the basaltic andesite dikes, Iritono, central Abukuma plateau. Can J Earth Sci 14, 1860–1866. https://doi.org/10.1139/e77-157.

Ishibashi, H., 2013. Spinel-melt oxygen barometry; a method and application to Cenozoic alkali basaltic magmas from the Higashi-Matsuura District, NW Kyushu, Japan. Geosci. Rep. Shizuoka Univ. 40, 21–32.

Jackson, K., 1969. Current concepts in crystal growth: The fundamental rate equation, J. Crystal Growth, 5, 13–18.

James, O.B., McGee, J.J., 1992. Compositional variations in mare-basalt plagioclase produced by differing crystallization regimes. Lunar Planet. Sci. XXIII, 603-604 (abstr.).

Kirkpatrick, R.J., Klein, L., Uhlmann, D.R., Hays, J.F., 1979. Rates and processes of crystal growth in the system anorthite-albite. J. Geophys. Res. 84, 3671–3676. https://doi.org/10.1029/JB084iB07p03671.

Kirkpatrick, R.J., 1975. Crystal Growth from the Melt: A Review. American Mineralogist 60, 798-814.

Kirkpatrick, R.J., 1981. Kinetics of crystallization of igneous rocks. In: Lasaga, A.C., Kirkpatrick, R.J. (Eds.). Rev Mineral Geochem 8, 321–397.

Kirkpatrick, R.J., Kuo, L.C., 1981. Crystal growth in incongruently-melting compositions: programmed cooling experiments with diopside. American Mineralogist 66, 223-241

Kirkpatrick, R.J., 1983. Theory of nucleation in silicate melts. American Mineralogist 68, 66-77.

Kneedler, A.E., 1989. Quantitative petrographic study of two diabase dikes intruded into the Sao Francisco craton, Brasil. BA Thesis, Princeton University.

Kohut, E., Nielsen, R.L., 2004. Melt inclusion formation mechanisms and compositional effects in high-An feldspar and high-Fo olivine in anhydrous mafic silicate liquids. Contrib. Mineral. Petrol. 147, 684–704. https://doi.org/10.1007/s00410-004-0576-0.

Kouchi, A., Tsuchiyama, A., Sunagawa, I., 1986. Effect of stirring on crystallization kinetics of basalt: texture and element partitioning. Contrib. Mineral. Petrol. 93, 429-438.

Kress, V.C., Carmichael, I.S.E., 1988. Stoichiometry of the iron oxidation reaction in silicate melts. Am Mineral 73, 1267-1274.

Kress, V.C., Carmichael, I.S.E., 1991. The compressibility of silicate liquids containing Fe2O3 and the effect of composition, temperature, oxygen fugacity and pressure on their redox states. Contrib. Mineral. Petrol. 108, 82-92.

La Spina, G., Burton, M., de' Michieli Vitturi, M., 2015. Temperature evolution during magma ascent in basaltic effusive eruptions: a numerical application to Stromboli volcano. Earth Planet. Sci. Lett. 426, 89–100. https://doi.org/10.1016/j.epsl.2015.06.015.

La Spina, G., Burton, M., de' Michieli Vitturi, M., Arzilli, F., 2016. Role of syn-eruptive plagioclase disequilibrium crystallization in basaltic magma ascent dynamics. Nat. Commun. 7, 13402. https://doi.org/10.1038/ncomms13402.

La Spina, G., Arzilli, F., Llewellin, E.W., Burton, M.R., Clarke, A.B., de' Michieli Vitturi, M., Polacci, M., Hartley, M.E., Di Genova, D., Mader, H.M., 2021. Explosivity of basaltic lava fountains is controlled by magma rheology, ascent rate and outgassing. Earth Planet. Sci. Lett. 553, 116658. https://doi.org/10.1016/j.epsl.2020.116658.

Landi, P., Métrich, N., Bertagnini, A., Rosi, M., 2004. Dynamics of magma mixing and degassing recorded in plagioclase at Stromboli (Aeolian Archipelago, Italy). Contrib. Mineral. Petrol. 147, 213–227. https://doi.org/10.1007/s00410-004-0555-5.

Landi, P., Francalanci, L., Pompilio, M., Rosi, M., Corsaro, R.A., Petrone, C.M., Nardini, I., Miraglia, L., 2006. The December 2002–July 2003 effusive event at Stromboli volcano, Italy: Insights into

the shallow plumbing system by petrochemical studies. J. Volcanol. Geotherm. Res. 155, 263–284. https://doi.org/10.1016/j.jvolgeores.2006.03.032.

Larsen, J.F., 2005. Experimental study of plagioclase rim growth around anorthite seed crystals in rhyodacitic melt. American Mineralogist 90, 417–427. https://doi.org/10.2138/am.2005.1456.

Lasaga, A.C., 1998. Kinetic Theory in the Earth Sciences. Princeton Univ. Press, Princeton, NJ. 781 pp.

Lang, S., Mollo, S., France, L., Misiti, V., Nazzari, M., 2021. Kinetic partitioning of major-minor cations between olivine and Hawaiian tholeiitic basalt under variable undercooling and cooling rate conditions. Chem. Geol. 584, 120485. https://doi.org/10.1016/j.chemgeo.2021.120485.

Lange, R.A., Frey, H.M., Hector, J., 2009. A thermodynamic model for the plagioclase-liquid hygrometer/thermometer. American Mineralogist 94, 494–506. https://doi.org/10.2138/am.2009.3011.

Le Gall, N., Arzilli, F., La Spina, G., Polacci, M., Cai, B., Hartley, M.E., Vo, N.T., Atwood, R.C., Di Genova, D., Nonni, S., Llewellin, E.W., Burton, M.R., Lee, P.D., 2021. In situ quantification of crystallisation kinetics of plagioclase and clinopyroxene in basaltic magma: Implications for lava flow. Earth Planet. Sci. Lett. 568, 117016. https://doi.org/10.1016/j.epsl.2021.117016.

Lindsley, D.H., Smith D., 1971. Chemical variations in the feldspars. Carnegie Institute of Washington Yearb 69, 274-278.

Lofgren, G., 1974. An experimental study of plagioclase crystal morphology; isothermal crystallization. Am. J. Sci. 274, 243-273. https://doi.org/10.2475/ajs.274.3.243.

Lofgren, G., 1980. Experimental studies on the dynamic crystallization of silicate melts. In: Hargraves RB (ed) The physics of magmatic processes. Princeton University Press, Princeton, pp 487–551

Long, D.A., 1977. Raman Spectroscopy. McGraw-Hill, pp. 276.

Longhi, J., Walker, D., Hays, J.F., 1976. Fe and Mg in plagioclase. Proc. Lunar Sci. Conf. 7th, 1281-1300.

Marsh, B.D., 1988. Crystal size distribution (CSD) in rocks and the kinetics and dynamics of crystallization. Contrib. Mineral. Petrol. 99, 277–291.

Masotta, M., Mollo, S., Freda, C., Gaeta, M., Moore, G., 2013. Clinopyroxene–liquid thermometers and barometers specific to alkaline differentiated magmas. Contrib. Mineral. Petrol. 166, 1545–1561. https://doi.org/10.1007/s00410-013-0927-9.

Métrich, N., Rutherford, M.J., 1998. Low Pressure Crystallization Paths of H2O-Saturated Basaltic-Hawaiitic Melts from Mt Etna: Implications for Open-System Degassing of Basaltic Volcanoes. Geochim. Cosmochim. Acta 62, 1195–1205. https://doi.org/10.1016/S0016-7037(98)00048-9.

Métrich, N., Allard, P., Spilliaert, N., Andronico, D., Burton, M., 2004. 2001 flank eruption of the alkali- and volatile-rich primitive basalt responsible for Mount Etna's evolution in the last three decades. Earth Planet. Sci. Lett. 228, 1–17. https://doi.org/10.1016/j.epsl.2004.09.036.

Métrich, N., Bertagnini, A., Di Muro, A., 2010. Conditions of Magma Storage, Degassing and Ascent at Stromboli: New Insights into the Volcano Plumbing System with Inferences on the Eruptive Dynamics. J. Petrol. 51, 603-626. https://doi.org/10.1093/petrology/egp083.

Mollard, E., Martel, C., Bourdier, J.-L., 2012. Decompression-induced Crystallization in Hydrated Silica-rich Melts: Empirical Models of Experimental Plagioclase Nucleation and Growth Kinetics. J. Petrol. 53, 1743–1766. https://doi.org/10.1093/petrology/egs031.

Mollo, S., Putirka, K., Iezzi, G., Del Gaudio, P., Scarlato, P., 2011. Plagioclase–melt (dis)equilibrium due to cooling dynamics: Implications for thermometry, barometry and hygrometry. Lithos 125, 221–235. https://doi.org/10.1016/j.lithos.2011.02.008.

Mollo, S., Misiti, V., Scarlato, P., Soligo, M., 2012. The role of cooling rate in the origin of high temperature phases at the chilled margin of magmatic intrusions. Chem. Geol. 322–323, 28–46. https://doi.org/10.1016/j.chemgeo.2012.05.029.

Mollo, S., Putirka, K., Misiti, V., Soligo, M., Scarlato, P., 2013. A new test for equilibrium based on clinopyroxene–melt pairs: Clues on the solidification temperatures of Etnean alkaline melts at

post-eruptive conditions. Chem. Geol. 352, 92–100. https://doi.org/10.1016/j.chemgeo.2013.05.026.

Mollo, S., Giacomoni, P.P., Coltorti, M., Ferlito, C., Iezzi, G., Scarlato, P., 2015a. Reconstruction of magmatic variables governing recent Etnean eruptions: Constraints from mineral chemistry and P–T–fO2–H2O modeling. Lithos 212–215, 311–320. https://doi.org/10.1016/j.lithos.2014.11.020.

Mollo, S., Giacomoni, P.P., Andronico, D., Scarlato, P., 2015b. Clinopyroxene and titanomagnetite cation redistributions at Mt. Etna volcano (Sicily, Italy): Footprints of the final solidification history of lava fountains and lava flows. Chem. Geol. 406, 45–54. https://doi.org/10.1016/j.chemgeo.2015.04.017.

Mollo, S., Masotta, M., Forni, F., Bachmann, O., De Astis, G., Moore, G., Scarlato, P., 2015c. A K-feldspar-liquid hygrometer specific to alkaline differentiated magmas. Chem. Geol. 392, 1-8. https://doi.org/10.1016/j.chemgeo.2014.11.010.

Mollo, S., Vetere, F., Beherens, H., Tecchiato, V., Langone, A., Scarlato, P., Perugini, D., 2017. The effect of degassing and volatile exsolution on the composition of a trachybasaltic melt decompressed at slow and fast rates. Period. di Mineral. 86. https://doi.org/10.2451/2017PM691.

Mollo, S., Hammer, J.E., 2017. Dynamic crystallization in magmas, in: Heinrich, W., Abart, R. (Eds.), Mineral Reaction Kinetics: Microstructures, Textures, Chemical and Isotopic Signatures. Mineralogical Society of Great Britain & Ireland, pp. 378–418. https://doi.org/10.1180/EMU-notes.16.12.

Mollo, S., Blundy, J., Scarlato, P., De Cristofaro, S.P., Tecchiato, V., Di Stefano, F., Vetere, F., Holtz, F., Bachmann, O., 2018. An integrated P-T-H2O-lattice strain model to quantify the role of clinopyroxene fractionation on REE+Y and HFSE patterns of mafic alkaline magmas: Application to eruptions at Mt. Etna. Earth Sci Rev 185, 32–56. https://doi.org/10.1016/j.earscirev.2018.05.014.

Moore, J.G., Evans, B.W., 1967. The role of olivine in the crystallization of the prehistoric Makaopuhi tholeiitic lava lake, Hawaii. Contrib. Mineral. Petrol. 15, 202–223. https://doi.org/10.1007/BF01185342.

Morgan, D.J., Jerram, D.A., 2006. On estimating crystal shape for crystal size distribution analysis. J. Volcanol. Geotherm. Res. 154, 1–7. https://doi.org/10.1016/j.jvolgeores.2005.09.016.

Moschini, P., Mollo, S., Gaeta, M., Fanara, S., Nazzari, M., Petrone, C.M., Scarlato, P., 2021. Parameterization of clinopyroxene growth kinetics via crystal size distribution (CSD) analysis: Insights into the temporal scales of magma dynamics at Mt. Etna volcano. Lithos 396–397, 106225. https://doi.org/10.1016/j.lithos.2021.106225.

Muncill, G.E., Lasaga, A. C., 1987. Crystal-growth kinetics of plagioclase in igneous systems: One-atmosphere experiments and application of a simplified growth model. American Mineralogist 72, 299-311.

Muncill, G.E., Lasaga, A. C., 1988. Crystal-growth kinetics of plagioclase in igneous systems: Isothermal H2O-saturated experiments and extension of a growth model to complex silicate melts. American Mineralogist 73, 982-992.

Mysen, B.O., Carmichael, I.S.E., Virgo, D., 1985. A comparison of iron redox ratios in silicate glasses determined by wet-chemical and 57 Fe Mössbauer resonant absorption methods. Contrib. Mineral. Petrol. 90, 101–106.

Nabelek, P.I., Taylor, L.A., Lofgren, G.E., 1978. Nucleation and growth of plagioclase and the development of textures in a high-alumina basaltic melt. Proc. Lunar Planet. Sci. Conf. 9th, 725-741.

Namur, O., Charlier, B., Toplis, M.J., Vander Auwera, J.V., 2012. Prediction of plagioclase-melt equilibria in anhydrous silicate melts at 1-atm. Contrib. Mineral. Petrol. 163, 133–150. https://doi.org/10.1007/s00410-011-0662-z.

Naney, M.T., Swanson, S.E., 1980. The effect of Fe and Mg on crystallization in granitic systems. American Mineralogist 65, 639-653.

Nelson, S.T., Montana, A., 1992. Sieve-textured plagioclase in volcanic rocks produced by rapid decompression. American Mineralogist 77, 1242-1249.

Nicholls, J., 1980. A Simple Thermodynamic Model for Estimating the Solubility of H2O in Magmas. Contrib. Mineral. Petrol. 74, 211-220.

Nielsen, R.L., Drake, M.J., 1979. Pyroxene-melt equilibria. Geochim. Cosmochim. Acta 43, 1259–1272. https://doi.org/10.1016/0016-7037(79)90117-0.

Orlando, A., D'Orazio, M., Armienti, P., Borrini, D., 2008. Experimental determination of plagioclase and clinopyroxene crystal growth rates in an anhydrous trachybasalt from Mt Etna (Italy). Eur. J. Mineral. 20, 653–664. https://doi.org/10.1127/0935-1221/2008/0020-1841.

Palummo, F., Mollo, S., De Astis, G., Di Stefano, F., Nazzari, M., Scarlato, P., 2020. Petrological and geochemical modeling of magmas erupted at Vulcano Island in the period 54-8 ka: Quantitative constraints on the sub-volcanic architecture of the plumbing system. Lithos 374-375, 105715.

Perinelli, C., Mollo, S., Gaeta, M., De Cristofaro, S.P., Palladino, D.M., Armienti, P., Scarlato, P., Putirka, K.D., 2016. An improved clinopyroxene-based hygrometer for Etnean magmas and implications for eruption triggering mechanisms. American Mineralogist 101, 2774–2777. https://doi.org/10.2138/am-2016-5916.

Peters, M.T., Shaffer, E.E., Burnett, D.S., Kim, S.S., 1995. Magnesium and titanium partitioning between anorthite and Type B CAI liquid: Dependence on oxygen fugacity and liquid composition. Geochim. Cosmochim. Acta 59, 2785–2796. https://doi.org/10.1016/0016-7037(95)00173-W.

Petrone, C.M., Bugatti, G., Braschi, E., Tommasini, S., 2016. Pre-eruptive magmatic processes re-timed using a non-isothermal approach to magma chamber dynamics. Nat. Commun. 7, 12946.

Petrone, C.M., Braschi, E., Francalanci, L., Casalini, M., Tommasini, S., 2018. Rapid mixing and short storage timescale in the magma dynamics of a steady-state volcano. Earth Planet. Sci. Lett. 492, 206–221.

Phinney, W.C., 1992. Partition coefficients for iron between plagioclase and basalt as a function of oxygen fugacity: Implications for Archean and lunar anorthosites. Geochim. Cosmochim. Acta 56, 1885–1895. https://doi.org/10.1016/0016-7037(92)90318-D.

Polacci, M., Andronico, D., de' Michieli Vitturi, M., Taddeucci, J., Cristaldi, A., 2019. Mechanisms of Ash Generation at Basaltic Volcanoes: The Case of Mount Etna, Italy. Front. Earth Sci. 7, 193. https://doi.org/10.3389/feart.2019.00193.

Pontesilli, A., Masotta, M., Nazzari, M., Mollo, S., Armienti, P., Scarlato, P., Brenna, M., 2019. Crystallization kinetics of clinopyroxene and titanomagnetite growing from a trachybasaltic melt: New insights from isothermal time-series experiments. Chem. Geol. 510, 113–129. https://doi.org/10.1016/j.chemgeo.2019.02.015.

Pontesilli, A., Brenna, M., Ubide, T., Mollo, S., Masotta, M., Caulfield, J., Le Roux, P., Nazzari, M., Scott, J. M., Scarlato, P., 2021. Intraplate Basalt Alkalinity Modulated by a Lithospheric Mantle Filter at the Dunedin Volcano (New Zealand). J. Petrol. 62 (10). https://doi.org/10.1093/petrology/egab062.

Pupier, E., Duchene, S., Toplis, M.J., 2008. Experimental quantification of plagioclase crystal size distribution during cooling of a basaltic liquid. Contrib. Mineral. Petrol. 155, 555–570. https://doi.org/10.1007/s00410-007-0258-9.

Putirka, K.D., 2005. Igneous thermometers and barometers based on plagioclase + liquid equilibria: Tests of some existing models and new calibrations. American Mineralogist 90, 336–346. https://doi.org/10.2138/am.2005.1449.

Putirka, K.D., 2008. Thermometers and Barometers for Volcanic Systems. Rev Mineral Geochem 69 (1), 61–120. https://doi.org/10.2138/rmg.2008.69.3.

Putirka, K.D., 2017. Geothermometry and Geobarometry. In: White W. (eds) Encyclopedia of Geochemistry. Encycl. Earth Sci. Ser. Springer, Cham. https://doi.org/10.1007/978-3-319-39193-9_322-1.

Putirka, K.D., Johnson, M., Kinzler, R., Longhi, J., Walker, D., 1996. Thermobarometry of mafic igneous rocks based on clinopyroxene-liquid equilibria, 0-30 kbar. Contrib. Mineral. Petrol. 123, 92–108. http://dx.doi.org/10.1007/s004100050145.

Sato, H., 1989. Mg-Fe partitioning between plagioclase and liquid in basalts of hole 504B, ODP LEG 111: A study of melting at 1 atm. Proceedings of the Ocean Drilling Program, 111 Scientific Results 111.

Schiavi, F., Walte, N., Keppler, H., 2009. First in situ observation of crystallization processes in a basaltic-andesitic melt with the moissanite cell. Geology 37, 963–966. https://doi.org/10.1130/G30087A.1.

Schiavi, F., Kobayashi, K., Moriguti, T., Nakamura, E., Pompilio, M., Tiepolo, M., Vannucci, R., 2010. Degassing, crystallization and eruption dynamics at Stromboli: trace element and lithium isotopic evidence from 2003 ashes. Contrib. Mineral. Petrol. 159, 541–561. https://doi.org/10.1007/s00410-009-0441-2.

Schanofsky, M., Fanara, S., Schmidt, B.C., 2019. CO2-H2O solubility in K-rich phonolitic and leucititic melts. Contrib Mineral Petrol 174, 52. https://doi.org/10.1007/s00410-019-1581-7.

Shea, T., Hammer, J.E., 2013. Kinetics of cooling- and decompression-induced crystallization in hydrous mafic-intermediate magmas. J. Volcanol. Geotherm. Res. 260, 127–145. https://doi.org/10.1016/j.jvolgeores.2013.04.018.

Shirley, D.N., 1987. Differentiation and Compaction in the Palisades Sill, New Jersey. J. Petrol. 28, 835–865. https://doi.org/10.1093/petrology/28.5.835.

Simakin, A.G., Salova, T.P., 2004. Plagioclase Crystallization from a Hawaiitic Melt in Experiments and in a Volcanic Conduit. Petrology 12, 82-92.

Singer, B.S., Pearce, T.H., Kolisnik, A.M., Myers, J.D., 1993. Plagioclase zoning in mid-Pleistocene lavas from the Seguam volcanic center, central Aleutian arc, Alaska. American Mineralogist 87, 143–157.

Sisson, T.W., Grove, T.L., 1993. Experimental investigations of the role of H2O in calc-alkaline differentiation and subduction zone magmatism. Contrib. Mineral. Petrol. 113, 143-166.

Smith, J.Y., Brown, W.L., 1988. Feldspar minerals vol. I: Crystal structures, physical, chemical, and microtextural properties, 2nd edition. Springer, Berlin, Heidelberg New, p. 828.

Smith, J.V., 1974. Feldspar Minerals. Vol. 2: Chemical and Textural Properties. Springer-Verlag. New York.

Smith, R.K., Lofgren, G.E., 1983. An analytical and experimental study of zoning in plagioclase. Lithos 16, 153-168.

Stolper, E., 1982. The speciation of water in silicate melts. Geochim. Cosmochim. Acta 46, 2609–2620. https://doi.org/10.1016/0016-7037(82)90381-7.

Sugawara, T., 2001. Ferric iron partitioning between plagioclase and silicate liquid: thermodynamics and petrological applications. Contrib. Mineral. Petrol. 141, 659–686. https://doi.org/10.1007/s004100100267.

Swanson, S.E., 1977. Relation of nucleation and crystal-growth rate to the development of granitic textures. American Mineralogist 62, 966–978.

Sun, C., Graff, M., Liang, Y., 2017. Trace element partitioning between plagioclase and silicate melt: The importance of temperature and plagioclase composition, with implications for terrestrial and lunar magmatism. Geochim. Cosmochim. Acta 206, 273–295. https://doi.org/10.1016/j.gca.2017.03.003.

Tsuchiyama, A., 1983. Crystallization kinetics in the system CaMgSi206-CaAI2Si2O8: the delay in nucleation of diopside and anorthite. American Mineralogist 68, 687-698.

Tsuchiyama, A., 1985. Crystallization kinetics in the system CaMgSi206-CaAI2Si2O8: development of zoning and kinetics effects on element partitioning. American Mineralogist 70, 474-486.

Ueki, K., Kuwatani, T., Okamoto, A., Akaho, S., & Iwamori, H. (2020). Thermodynamic modeling of hydrous-melt–olivine equilibrium using exhaustive variable selection. Physics of the Earth and Planetary Interiors, 300, 106430. https://doi.org/10.1016/j.pepi.2020.106430.

Vetere, F., Iezzi, G., Behrens, H., Holtz, F., Ventura, G., Misiti, V., Cavallo, A., Mollo, S., Dietrich, M., 2015. Glass forming ability and crystallisation behaviour of sub-alkaline silicate melts. Earth Sci Rev 150, 25–44. https://doi.org/10.1016/j.earscirev.2015.07.001.

Vona, A., Romano, C., 2013. The effects of undercooling and deformation rates on the crystallization kinetics of Stromboli and Etna basalts. Contrib to Mineral Petrol 166, 491–509. https://doi.org/10.1007/s00410-013-0887-0.

Waters, L.E., Lange, R.A., 2015. An updated calibration of the plagioclase-liquid hygrometer-thermometer applicable to basalts through rhyolites. American Mineralogist 100, 2172–2184. https://doi.org/10.2138/am-2015-5232.

Watson, E.B., Müller, T., 2009. Non-equilibrium isotopic and elemental fractionation during diffusion-controlled crystal growth under static and dynamic conditions. Chem. Geol. 267, 111–124. https://doi.org/10.1016/j.chemgeo.2008.10.036.

Wilke, M., Behrens, H., 1999. The dependence of the partitioning of iron and europium between plagioclase and hydrous tonalitic melt on oxygen fugacity. Contrib. Mineral. Petrol. 137, 102–114. https://doi.org/10.1007/s004100050585.

Wood, B.J., Blundy, J.D., 2002. The effect of H2O on crystal-melt partitioning of trace elements. Geochim. Cosmochim. Acta 66, 3647–3656. https://doi.org/10.1016/S0016-7037(02)00935-3.

Wright, T.L., Okamura, R.T., 1977. Cooling and crystallization of tholeiitic basalt, 1965 Makaopuhi lava lake, Hawaii. US Geol Surv Prof Pap 1004

Xue, S., Morse, S.A., 1994. Chemical characteristics of plagioclase and pyroxene megacrysts and their significance to the petrogenesis of the Nain anorthosites. Geochim. Cosmochim. Acta 58, 4317–4331. https://doi.org/10.1016/0016-7037(94)90336-0.

Zhang, Y., 2010. Diffusion in minerals and melts: theoretical background. In: Zhang, Y., Cherniak, D. (Eds.), Diffusion in Minerals and Melts. Rev. Mineral. Geochem. 72. pp. 5–60.

Figure captions

Figure 1. Variation of plagioclase growth rate on a logarithmic scale as a function of isothermal-isobaric and fast-slow decompression conditions for Stromboli (a) and Etna (b) compositions.

Figure 2. Plot of growth rate from our experiments against time on a logarithmic scale (a). Comparison between growth rate from our experiments and those from literature reported in Supplementary Material 4 (b).

Figure 3. Compositional variation of plagioclase crystals from isothermal-isobaric and fast-slow decompression conditions as a function of temperature and melt-water content.

Figure 4. Plot of mol.% of MgO and FeO (i.e., total iron as FeO from microprobe analysis) in plagioclase against those of melt oxides from isothermal-isobaric and fast-slow decompression conditions (a). Plot of plagioclase-melt partition coefficients for iron and magnesium against melt components calculated with the two-lattice melt model of Nielsen and Drake (1979) (b).

Figure 5. Variation of Fe-Mg and An-Ab exchange partition coefficients between plagioclase and melt as a function of temperature and melt-water concentration. Data from isothermal-isobaric and fast-slow decompression experiments.

Figure 6. Plot of An^{melt}/Ab^{melt} against An^{pl}/Ab^{pl} for isothermal-isobaric and fast-slow decompression experiments carried out on mafic alkaline compositions from this study, compared with literature data from Sisson and Grove (1993), Lange et al. (2009), and Waters and Lange (2015). Data are grouped as calcalkaline basalts-andesites ($T \approx$ 1100-1235 °C and $H_2O^{melt} \approx$ 0-2 wt.%), calcalkaline dacites-rhyolites ($T \approx$ 800-1060 °C and $H_2O^{melt} \approx$ 2-8 wt.%), and mafic alkaline melts ($T \approx$ 1050-1150 °C and $H_2O^{melt} \approx$ 0.0-4.4 wt.%).

Figure 7. Compositional variation of melt major oxides from isothermal-isobaric and fast-slow decompression experiments is compared with natural bulk rock compositions of magmas erupted at Stromboli and Mt. Etna.

Figure 8. Plot of measured against predicted values of $\ln\left(a_{\mathrm{An}}^{melt}\right)$ (a) and $\ln\left(a_{\mathrm{Ab}}^{melt}\right)$ (b) using the model of Glazner (1984). Plot of measured against predicted values of $\ln\left(a_{\mathrm{An}}^{melt}\right)$ using Eq. 28 from Namur et al. (2012) (c). Plot of measured against predicted values of X_{An}^{pl} using Eq. (31) and Eq. (33) from Namur et al. (2012) (d).

Figure 9. Plot of measured against predicted values of $\ln\left(a_{\mathrm{An\ or\ Ab}}^{melt}\right)$ by excluding (a) and including (b) the water-related Margules interaction parameters from Ueki et al. (2020).

Figure 10. Plot of measured against predicted values of temperature from different plagioclase-based thermometric models. Eq. (42) from this study is compared with Eq. (A) and Eq. (D) from Putirka (2005), Eq. (24a) and Eq. (26) from Putirka (2008), Eq. (27a), Eq. (27b) and Eq. (27c) from Putirka (2017). SEE refers to the standard error of estimate resulting from the model calibration.

Figure 11. Violin plots and box plots for anorthite in plagioclase phenocrysts from 2007-2021 eruptions at Stromboli (a), temperature predicted by Eq. (42) from this study (b), and melt-water content predicted by the hygrometers of Putirka (2008) (c) and Waters and Lange (2015) (d). A kernel density estimation is used to visualize the underlying probability density function of each set of data in violin plots, whereas the statistical dispersion of data is illustrated by the box plot. The width of the box represents the interquartile range (*IQR*) extending from the first quartile (25^{th} percentile *Q1*) to the third quartile (75^{th} percentile *Q3*) and whiskers go from each quartile to the minimum or

maximum. SCC, subrounded corroded cores. STCL, sieve-textured concentric layers. OZCL, oscillatory-zoned concentric layers. OR, overgrowth rims.

Figures

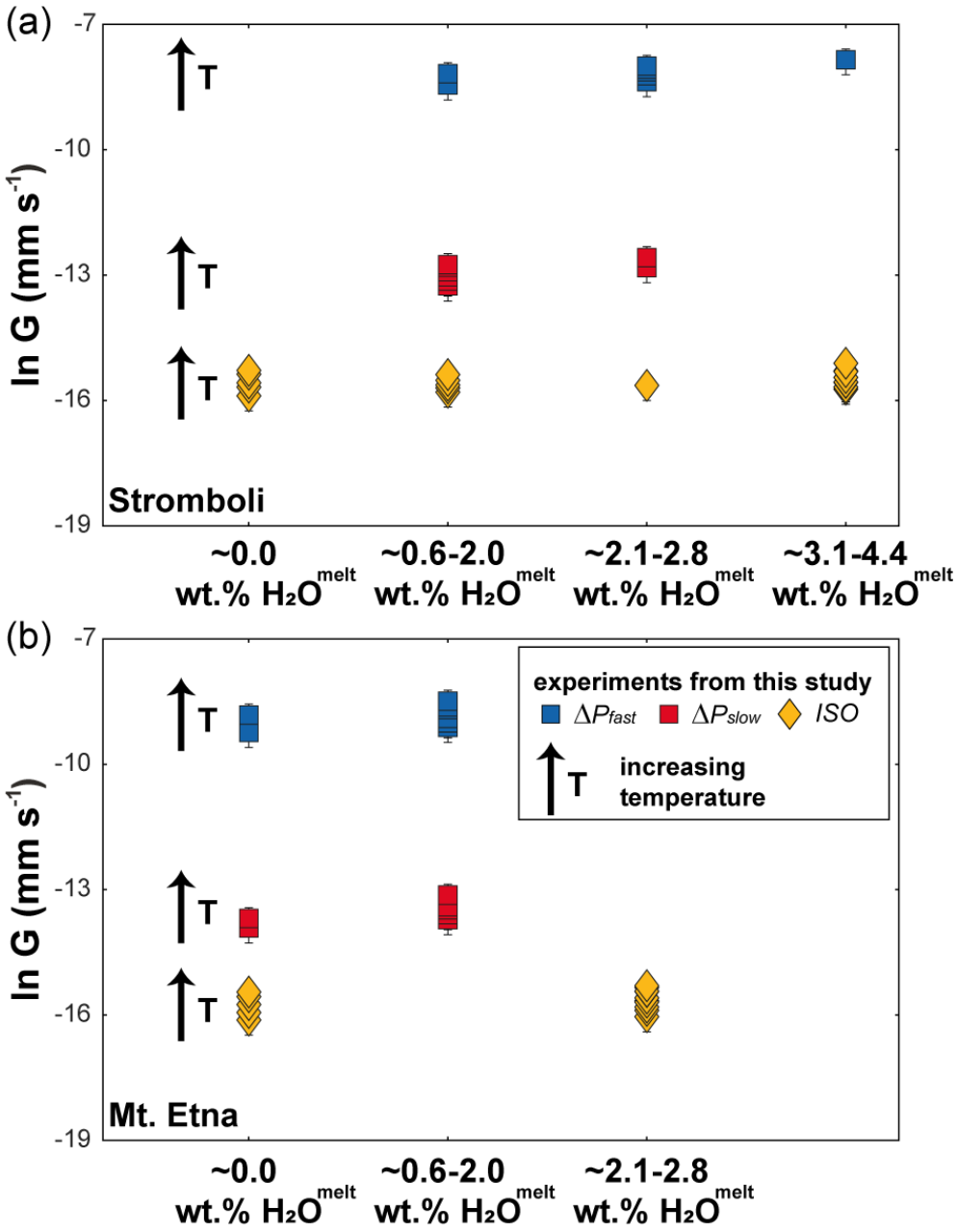

Figure 1

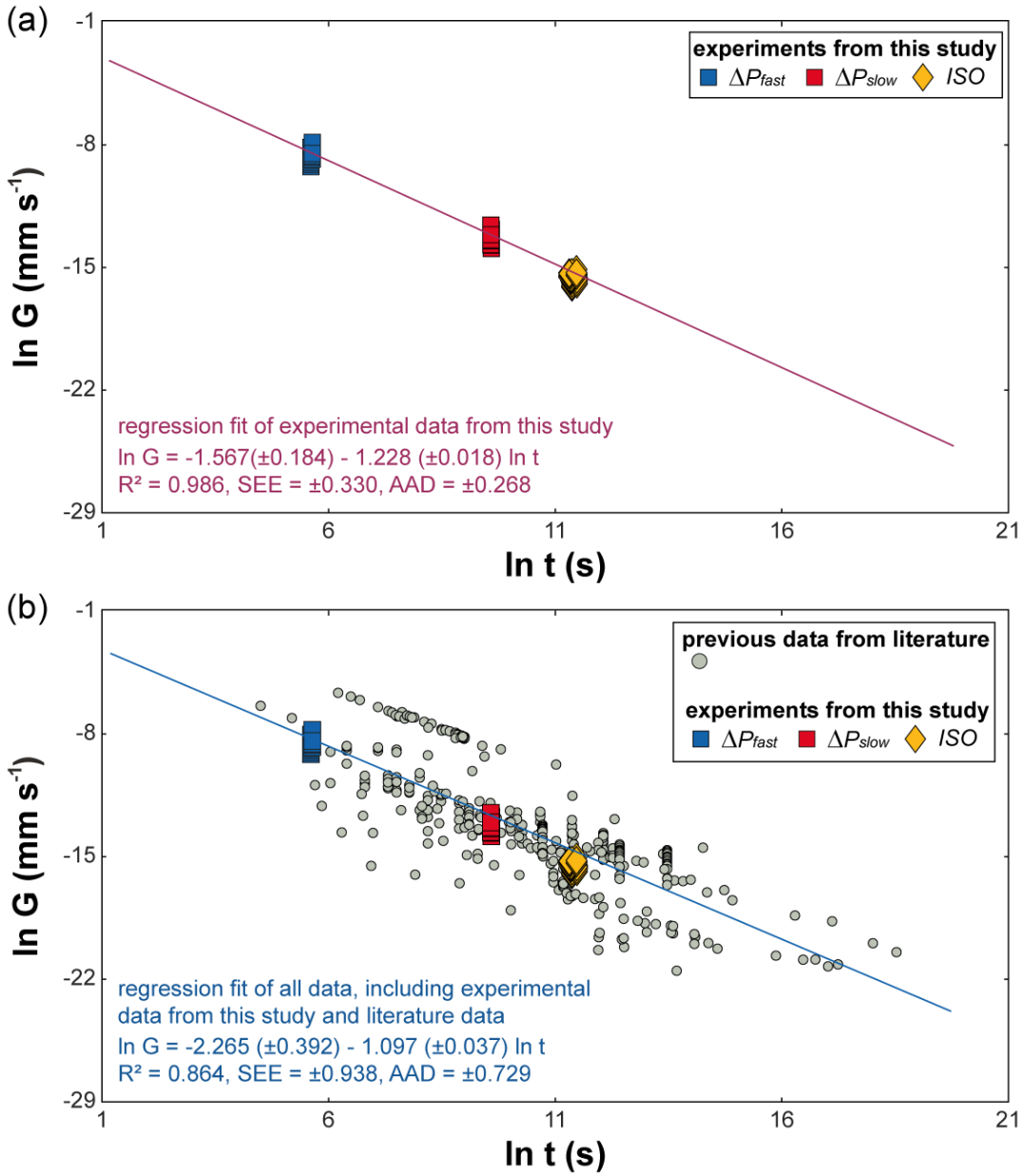
(a)
experiments from this study
ΔPfast ΔPslow ISO
regression fit of experimental data from this study
ln G = -1.567(±0.184) - 1.228 (±0.018) ln t
R² = 0.986, SEE = ±0.330, AAD = ±0.268
ln G (mm s-1)
ln t (s)
(b)
previous data from literature
experiments from this study
ΔPfast ΔPslow ISO
regression fit of all data, including experimental
data from this study and literature data
ln G = -2.265 (±0.392) - 1.097 (±0.037) ln t
R² = 0.864, SEE = ±0.938, AAD = ±0.729
ln G (mm s-1)
ln t (s)

Figure 2

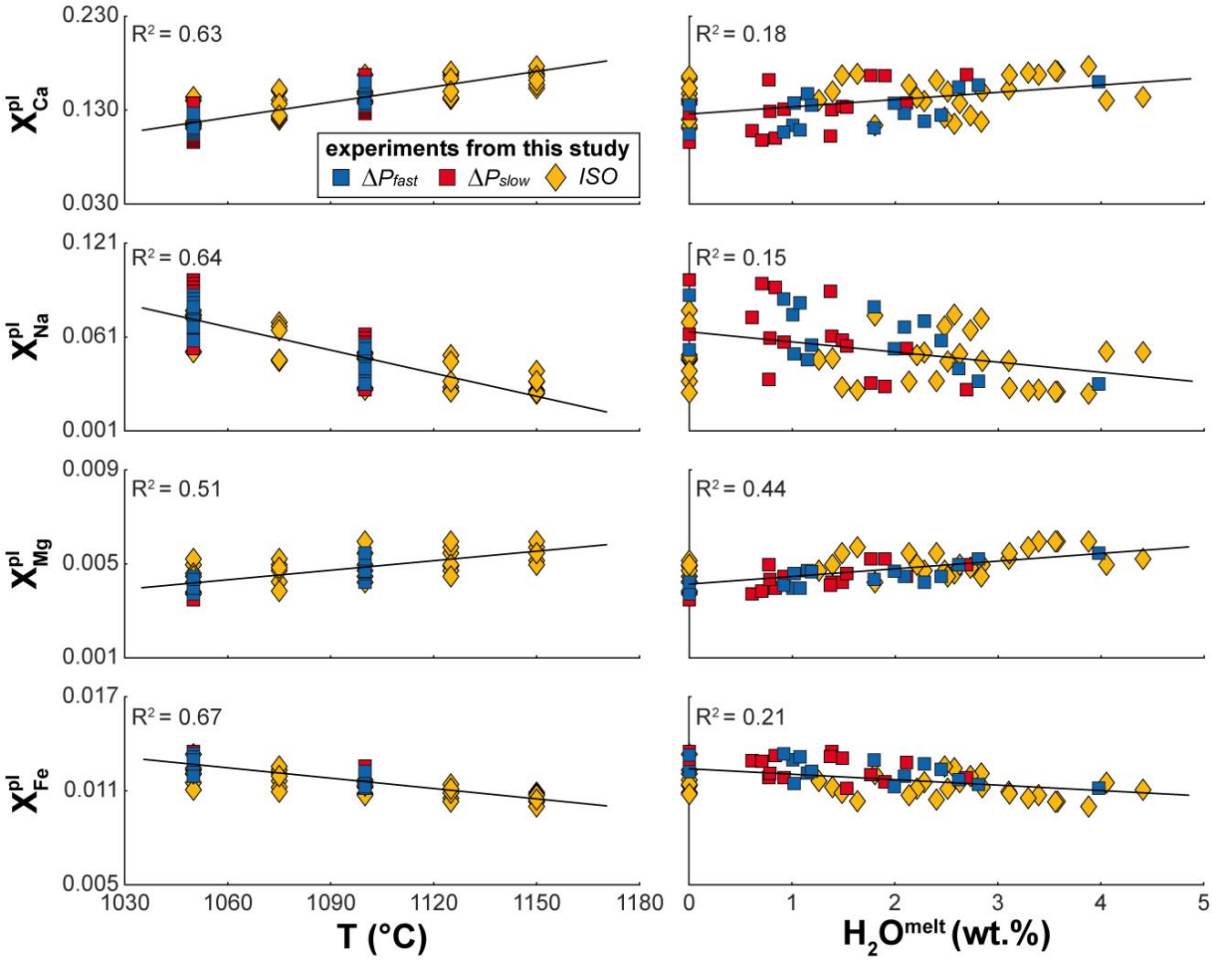
R² = 0.63
R² = 0.18
R² = 0.64
R² = 0.15
R² = 0.51
R² = 0.44
R² = 0.67
R² = 0.21
experiments from this study
ΔPfast
ΔPslow
ISO
0.230
0.130
0.030
0.121
0.061
0.001
0.009
0.005
0.001
0.017
0.011
0.005
1030
1060
1090
1120
1150
1180
0
1
2
3
4
5
T (°C)
H2Omelt (wt.%)

Figure 3

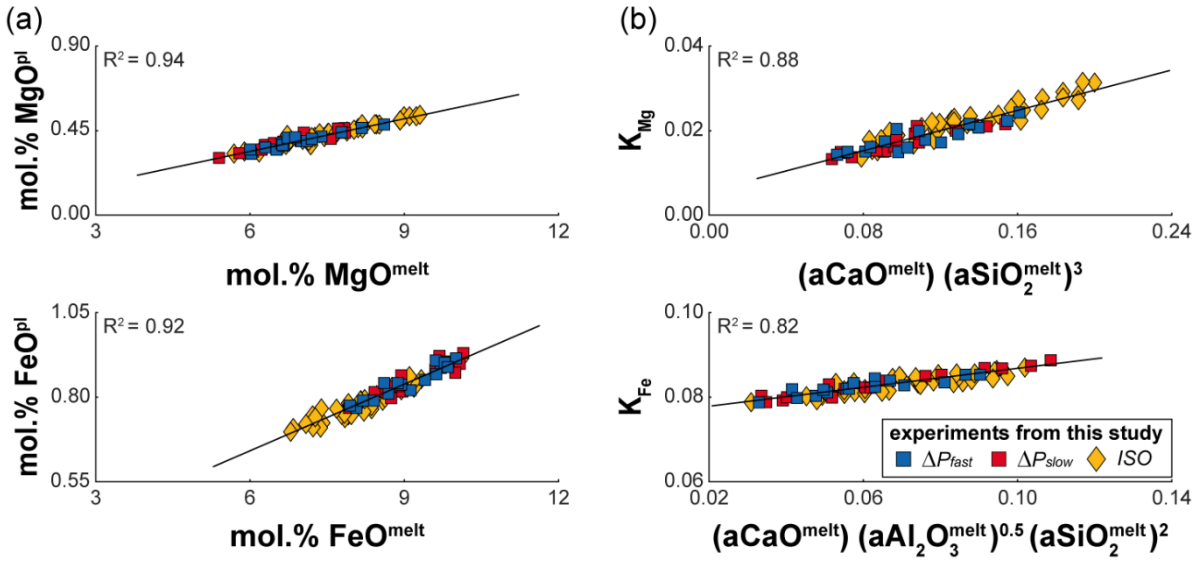

Figure 4

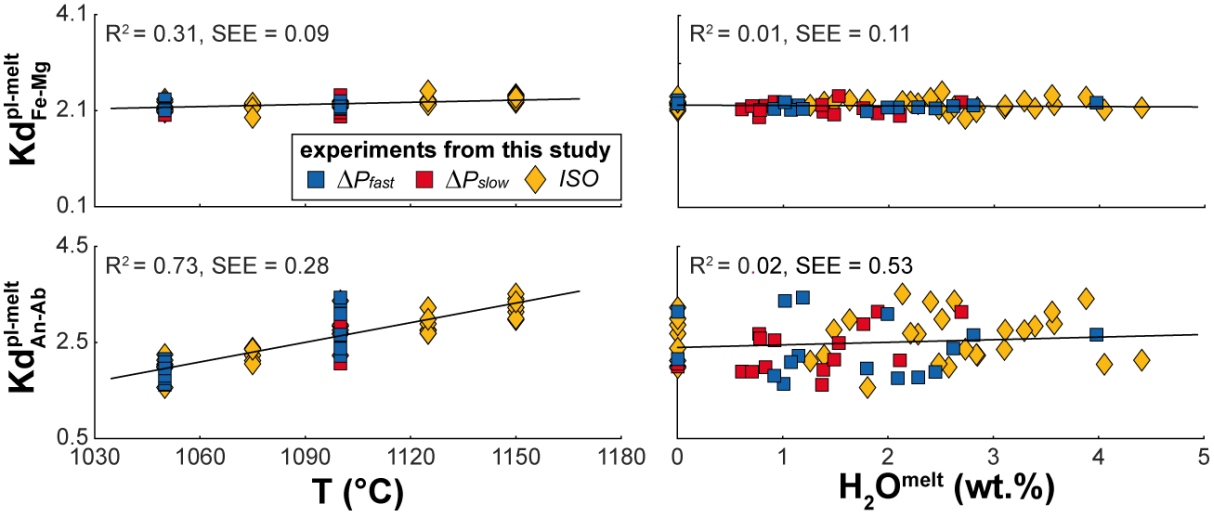

Figure 5

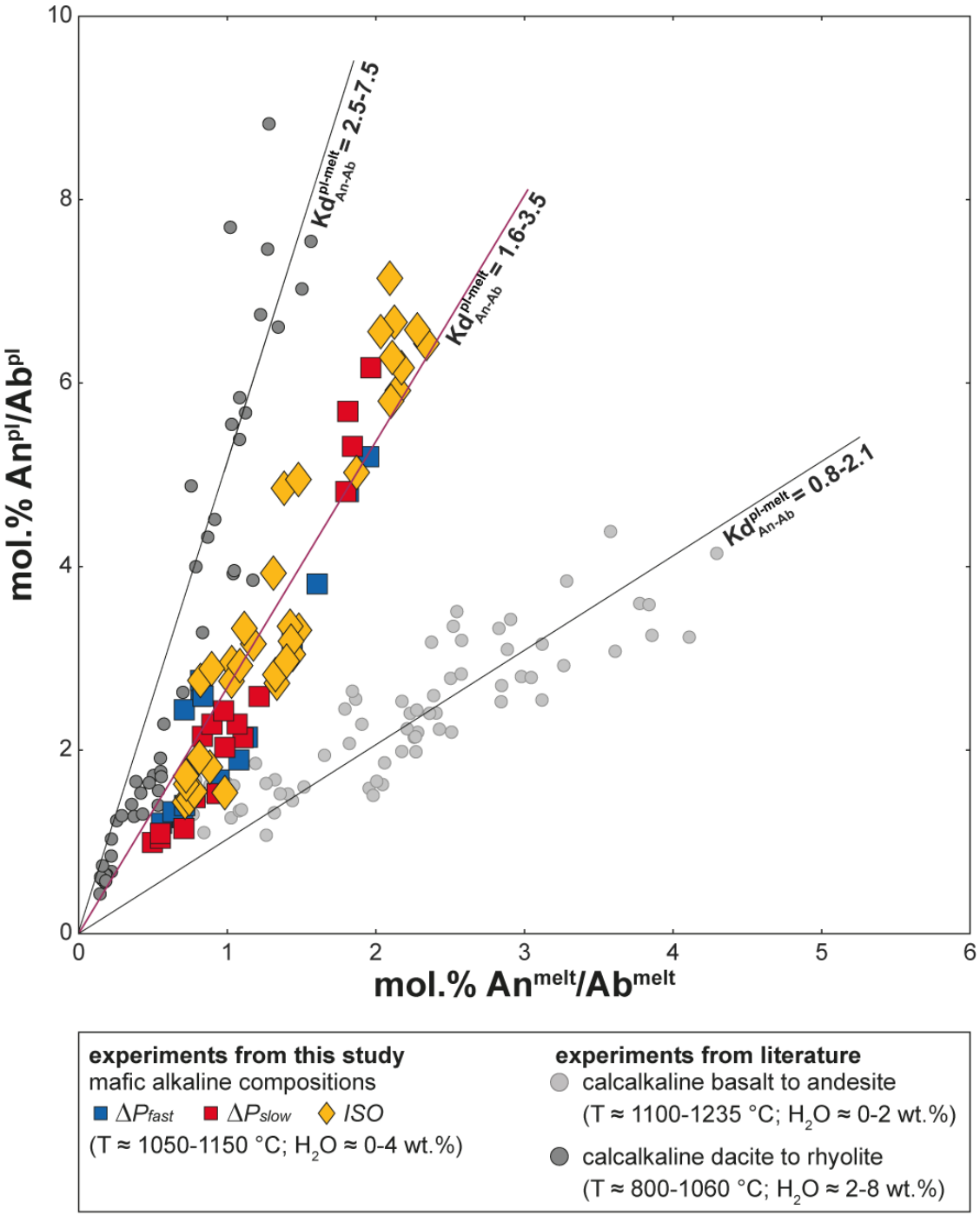
mol.% An^pl/Ab^pl
mol.% An^melt/Ab^melt
Kd^pl-melt An-Ab = 2.5-7.5
Kd^pl-melt An-Ab = 1.6-3.5
Kd^pl-melt An-Ab = 0.8-2.1
0
1
2
3
4
5
6
0
2
4
6
8
10
experiments from this study
mafic alkaline compositions
ΔPfast ΔPslow ISO
(T ≈ 1050-1150 °C; H2O ≈ 0-4 wt.%)
experiments from literature
calcalkaline basalt to andesite
(T ≈ 1100-1235 °C; H2O ≈ 0-2 wt.%)
calcalkaline dacite to rhyolite
(T ≈ 800-1060 °C; H2O ≈ 2-8 wt.%)

Figure 6

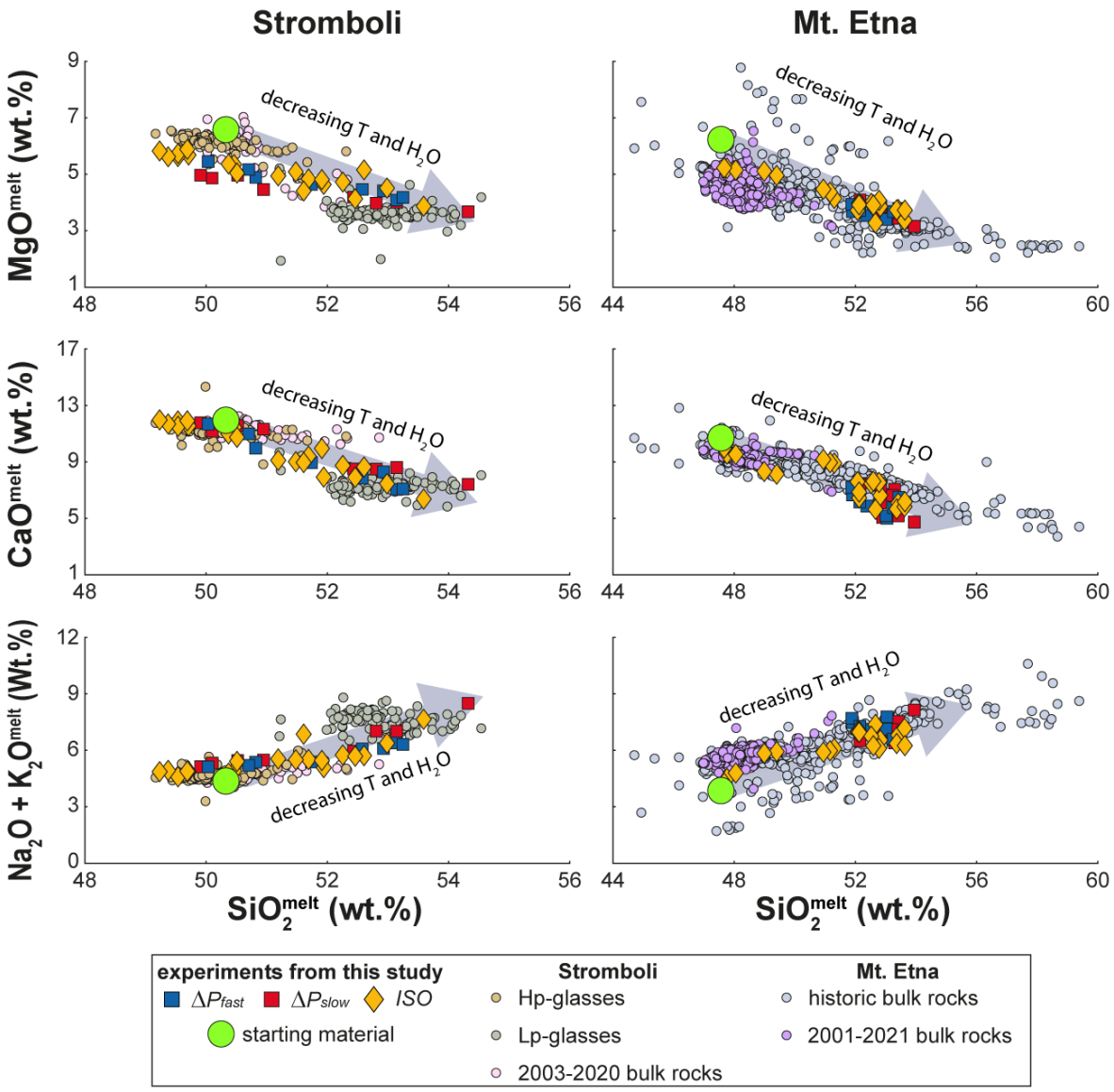
Stromboli
Mt. Etna
MgO melt (wt.%)
CaO melt (wt.%)
Na2O + K2O melt (Wt.%)
SiO2 melt (wt.%)
decreasing T and H2O
experiments from this study
ΔPfast
ΔPslow
ISO
starting material
Stromboli
Hp-glasses
Lp-glasses
2003-2020 bulk rocks
Mt. Etna
historic bulk rocks
2001-2021 bulk rocks

Figure 7

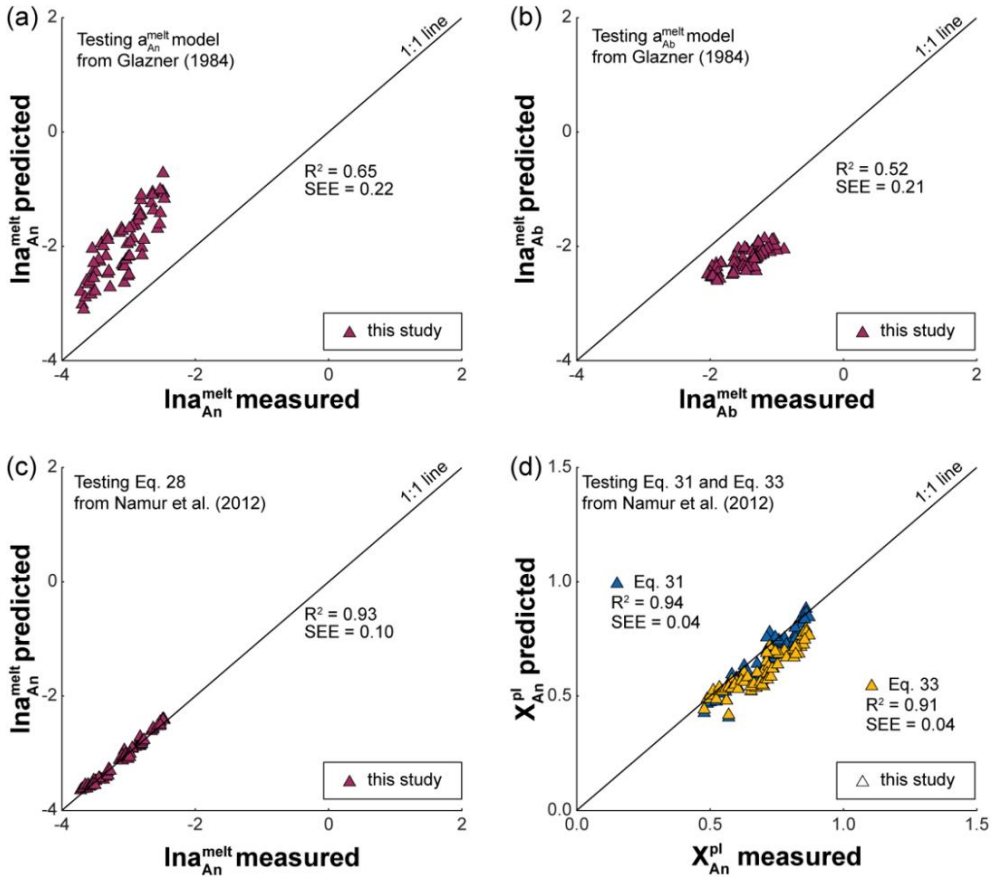

Figure 8

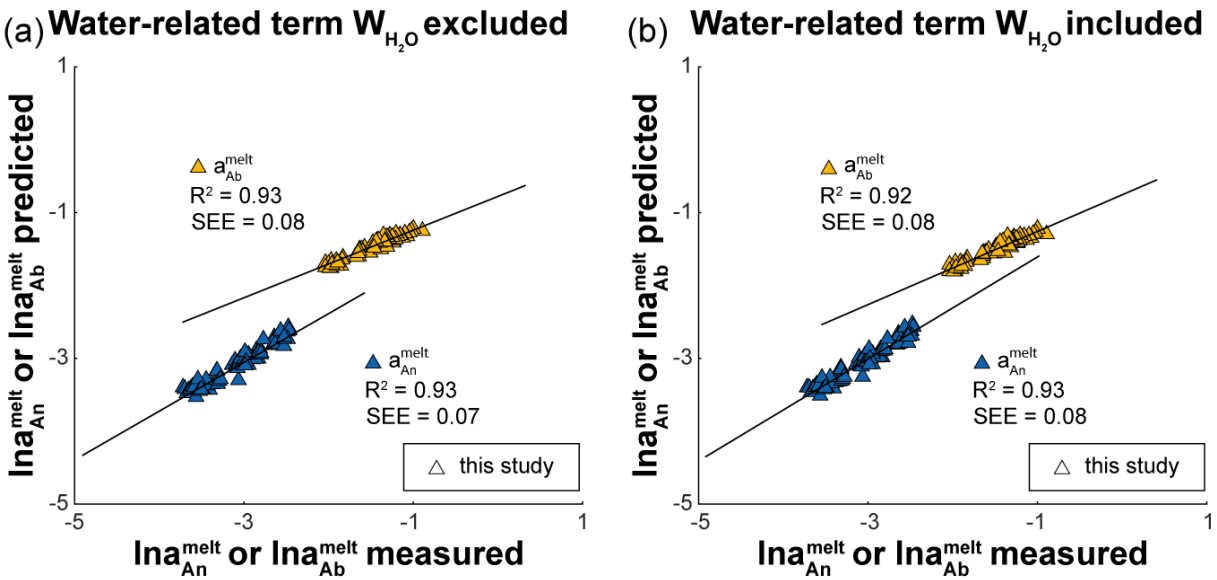

Figure 9

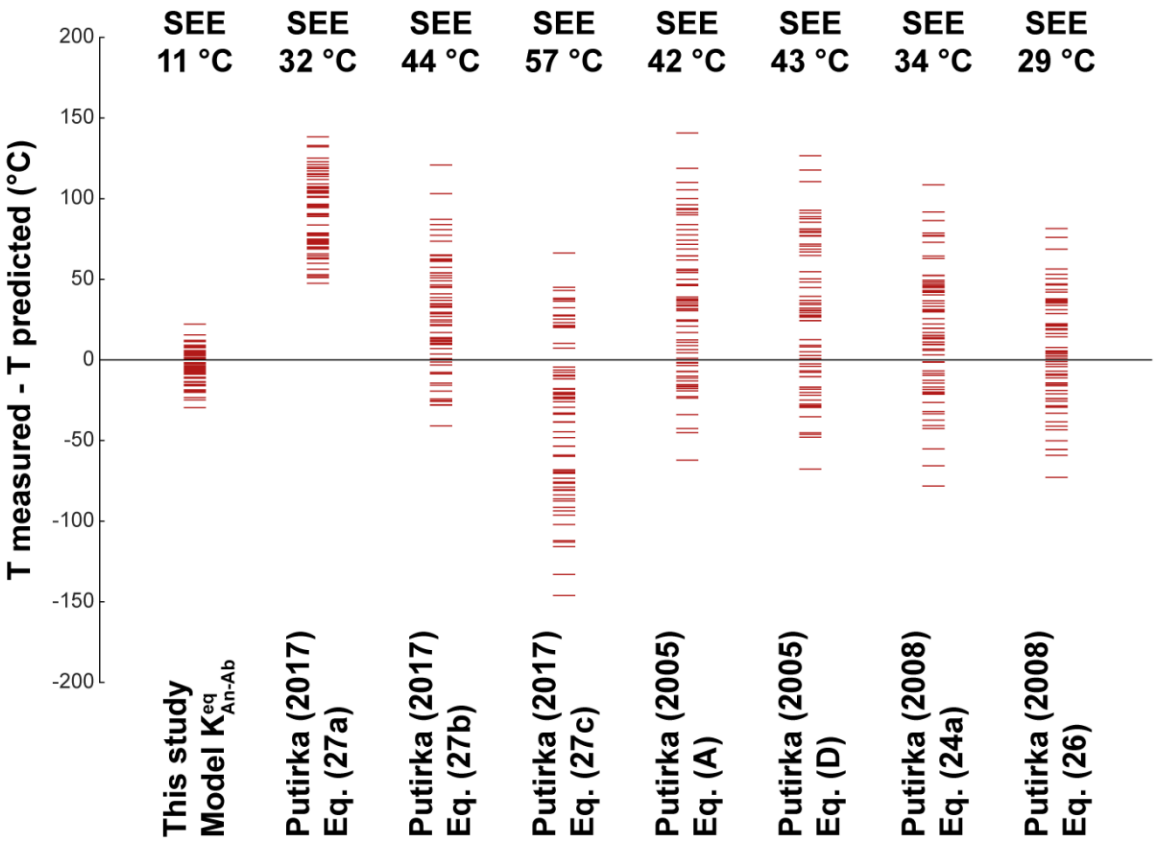
SEE 11 °C
SEE 32 °C
SEE 44 °C
SEE 57 °C
SEE 42 °C
SEE 43 °C
SEE 34 °C
SEE 29 °C
T measured - T predicted (°C)
200
150
100
50
0
-50
-100
-150
-200
This study Model K^{eq}_{An-Ab}
Putirka (2017) Eq. (27a)
Putirka (2017) Eq. (27b)
Putirka (2017) Eq. (27c)
Putirka (2005) Eq. (A)
Putirka (2005) Eq. (D)
Putirka (2008) Eq. (24a)
Putirka (2008) Eq. (26)

Figure 10

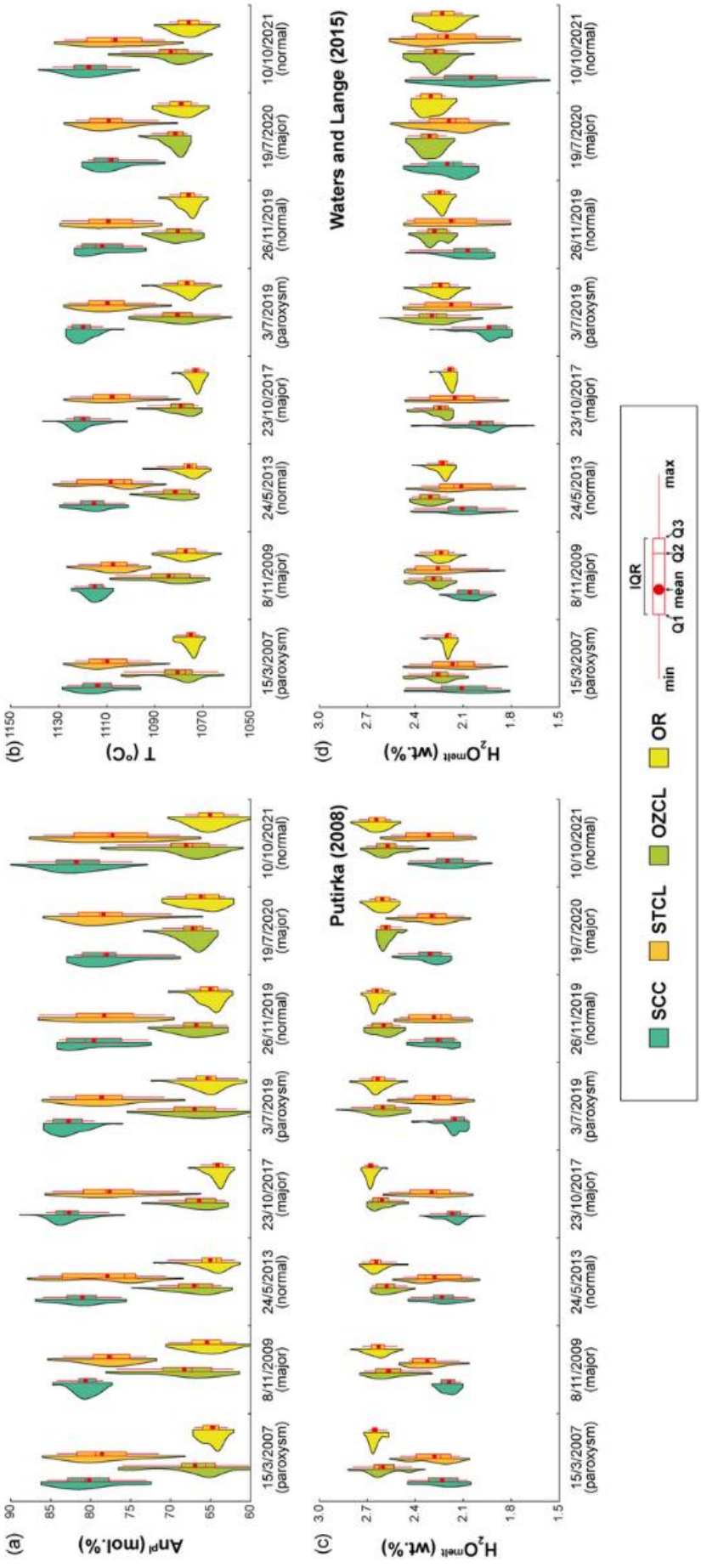
(a)
(b)
(c)
(d)
Putirka (2008)
Waters and Lange (2015)
SCC
STCL
OZCL
OR
IQR
min
Q1
mean
Q2
Q3
max
15/3/2007 (paroxysm)
8/11/2009 (major)
24/5/2013 (normal)
23/10/2017 (major)
3/7/2019 (paroxysm)
26/11/2019 (normal)
19/7/2020 (major)
10/10/2021 (normal)

Figure 11

Supplementary data to this article can be found online at https://drive.google.com/drive/folders/13-Dhwh21nZprosAXF3vQfyuL_pZj0ztL?usp=share_link.

Concluding remarks

Mt. Etna and Stromboli are some of the most studied and monitored volcanoes in the world. These two open-conduit basaltic volcanoes are characterized by persistent high-frequency, low-magnitude explosive activity alternating with high-magnitude, short-lasting eruptions. In this context, understanding and quantifying the timescales and dynamics of magma transport is critical to mitigate volcanic hazards and represent a persisting compelling challenge in the petrological-volcanological field.

In this PhD thesis, clinopyroxene and plagioclase growth kinetics have been experimentally investigated and parameterized under a broad range of isothermal-isobaric, decompression, and cooling rate conditions that mimic the crystallization paths of magmas erupted at Mt. Etna and Stromboli. My results document how the textural evolution of clinopyroxene and plagioclase is greatly controlled by melt supersaturation corresponding to a certain degree of undercooling. Imbalance between crystal growth rate and diffusion of cations in the melt arises at large degrees of undercooling leading to disequilibrium uptake of incompatible cations at the crystal-melt interface. Concentration gradients promote high nucleation rates and fast development of small and anhedral crystals. However, relaxation phenomena become more effective as the crystallization time proceeds, thereby lowering the crystal growth rate prior to the establishment of a full thermodynamic equilibrium throughout the crystal-melt interface. This leads to a steady state textural maturation driving the transition from diffusion-controlled to interface-controlled growth regimes. I found that the decay of crystal growth rate over time can be integrated with the crystal size distribution analysis to estimate the timescale of clinopyroxene and plagioclase formation. For the case of Mt. Etna lava fountains, results from calculations return timescales in the order of ~10^0-10^1 min and ~10^1-10^2 h for clinopyroxene microlite and microphenocryst populations, respectively. Similarly, timescales of plagioclase microlites vary from ~10^0-10^1 min at Stromboli volcano. Short timescales estimated for microlites conform to fast kinetic effects due to large degrees of undercooling during magma acceleration in the uppermost part of the volcanic conduit as the result of strong decompression,

degassing, and cooling phenomena. Conversely, longer timescales estimated for microphenocrysts are prevalently associated with near-equilibrium crystallization due to slow magma ascent rates and small degrees of undercooling at depth.

Plagioclase compositional parameters have been examined under the rationale of thermodynamic principles. This approach is pivotal to disambiguate the role of temperature and melt-water content on plagioclase zoning patterns at Stromboli and Mt. Etna. My results document how the strength of correlation between plagioclase cation fractions and melt-water content is weak and is overwhelmingly mitigated by the change of temperature. Moreover, no statistically significant correlation has been found between the An-Ab exchange partition coefficient and melt-H_2O content. The effect of dissolved water in decreasing the activity of silica in the melt and the saturation surface of plagioclase is dominated by the variation of anhydrous melt components as a function of temperature when low to moderate amounts of dissolved water occur in the melt (i.e., maximum melt-water content of 4.4 wt.%). Therefore, it is not surprising that literature anhydrous models for calculating the activity-composition relations of An in both plagioclase and melt phases return very good regression statistic. By adopting a Margules power-series expansion approach, I have obtained a thermodynamic description for the activity coefficient of An and Ab components in the melt. Results from thermodynamic calculations show that the speciation of water does not offer any improvement in the ability prediction of An and Ab activities in the melt, thereby emphasizing the subordinate role of water on plagioclase-melt equilibria at the experimental conditions investigated in my PhD thesis. A pressure and melt-H_2O independent thermometer specific to mafic alkaline compositions has been developed taking advantage of the close relation between An-Ab equilibrium constant and temperature. Finally, by reappraising plagioclase-based equilibrium, thermometric, and hygrometric equations, I have developed an integrated model to decode complex zoning patterns in natural plagioclase phenocrysts solidifying from mafic alkaline magmas. The model has been tested on plagioclase phenocrysts from 2007-2021 eruptions at Stromboli with the aim to provide guidelines and a secure methodology for future petrological studies. A key outcome from this approach is that

statistical analysis can help to disambiguate the role of temperature and melt-water content on plagioclase compositional variability, with the strong limitation that textural complexities are susceptive to multiple interpretations in chemically and physically dynamic systems.

Acknowledgements

Firstly, I would like to thank Prof. Mario Gaeta and Prof. Silvio Mollo for supervising my PhD study. Their inspiring advice, patience and assistance brought me to the achievement of the PhD project objectives and encouraged me to do my best all along the academic path.

Many thanks also to Dr. Piergiorgio Scarlato who gave me access to experimental and analytical facilities at the High Pressure High Temperature (HP-HT) Laboratory of Geophysics and Volcanology of the Istituto Nazionale di Geofisica e Vulcanologia (INGV). I wish to thank Dr. Manuela Nazzari for her assistance with the electron microprobe and with the scanning electron microscope. I thank Alessio Pontesilli for teaching me how to use experimental facilities at INGV laboratories. Special thanks to Sara Fanara and all the people of the Department of Experimental and Applied Mineralogy at Georg August University of Göttingen who helped me with the experimental sessions run during my first international mobility. Moreover, my gratitude goes to Prof. Olivier Bachmann, Dr. Ben S. Ellis, Dr. Marcel Guillong (Institute of Geochemistry and Petrology – ETH Zurich) for their assistance with laser ablation inductively coupled plasma mass spectrometry analyses. I would like to express my gratitude to Prof. Alessandro Vona and Prof. Claudia Romano who gave me access to the micro-Raman spectrometer at EVPLab of Roma Tre University. I am also grateful to Dr. Maria Chiara Petrone (Natural History Museum - London), Dr. Giovanni Chiodini, Dr. Giulio Bini, Dr. Gianfranco Galli (INGV). Final thanks to all people of HP-HT Laboratory of the INGV.